The chemical consequences of the gradual decrease of the ionic radius along the Ln-series

Joop A. Peters [a,*], Kristina Djanashvili [a], Carlos F.G.C. Geraldes [b,c], Carlos Platas-Iglesias [d]

[a] Department of Biotechnology, Delft University of Technology, Van der Maasweg 9, 2629 HZ Delft, The Netherlands
[b] Department of Life Sciences and Coimbra Chemistry Centre, Faculty of Science and Technology, University of Coimbra, Calçada Martim de Freitas, 3000-456 Coimbra, Portugal
[c] CIBIT/ICNAS, University of Coimbra, Azinhaga de Santa Comba, 3000-548 Coimbra, Portugal
[d] Centro de Investigacións Científicas Avanzadas (CICA) and Departamento de Química, Universidade da Coruña, Campus da Zapateira-Rúa da Fraga 10, 15008 A Coruña, Spain

ABSTRACT

In the periodical system, the lanthanides (the 15 elements in the periodic table between barium and hafnium) are unique in the sense that their trivalent cations have their valence electrons hidden behind the 5s and 5p electrons. They show a gradual decrease in ionic radius with increasing atomic number (also known as the lanthanide contraction). The resulting steric effects determine to a large extent the geometries of complexes of these ions. Here, we discuss these effects, particularly upon the properties of the complexes in aqueous solution, for selected families of Ln^{3+}-complexes of oxycarboxylate and aminocarboxylate ligands. The physical properties of the cations are very different, which is very useful for the elucidation of the configuration, conformation and the dynamics of the complexes by X-ray techniques, NMR spectroscopy, and optical techniques. Often the structural analysis is assisted by computational methods.
© 2019 The Authors. Published by Elsevier B.V. This is an open access article under the CC BY license (http://creativecommons.org/licenses/by/4.0/).

Contents

Abbreviations: BCP, Bond critical point; BTP, bicapped trigonal prism; CN, coordination number; DFT, density functional theory; DPA, 2,6-dipicolinate; DOTA, 1,4,7,10-tetraazacyclododecane-1,4,7,10-tetraacetate; DOTMA, 1R,4R,7R,10R-α,α′, α″, α‴- tetramethyl-1,4,7,10-tetraazacyclododecane-1,4,7,10-tetraacetate; DTPA, diethylenetriamine-N,N,N′,N″,N″-pentaacetate; DTPA-BMA, 1,7-bis[(N-methylcarbamoyl)methyl]-1,4,7-triazaheptane-1,4,7-triacetate; LIS, lanthanide induced shift; MD, molecular dynamics; EDTA, ethylenediamine-N,N,N′,N′-tetraacetate; EGTA, ethylene glycol-bis(2-aminoethylether)-N,N,N′,N′-tetraacetate; EXAFS, extended X-ray absorption fine structure; NMR, nuclear magnetic resonance; ODA, oxydiacetate; PCS, pseudo contact shift; SA, square antiprism; SBM, Solomon-Bloembergen-Morgan; SO-CASSCF, spin-orbit complete active space self-consistent field; TTP, tricapped trigonal prism; TSA, twisted square antiprism; XANES, X-ray absorption near edge structure.
* Corresponding author.
E-mail address: J.A.Peters@tudelft.nl (J.A. Peters).

1. Introduction

When Mendeleev designed the first version of the Periodic Table 150 years ago, only four lanthanides (La, Ce, Er, and Tb) were known [1–3]. The chemical similarity of the lanthanides made their separation rather cumbersome and allocation into the Periodic Table of any later discovered lanthanide posed problems due to the similarities in their chemical behavior. During the 20th century, the lanthanides and actinides were usually represented as a footnote to the Table. This way of presentation is still the most common one, although, from a systematic point of view, the so-called long table (Fig. 1) is the most logical one considering the current understanding of atomic structures.

All lanthanides have stable isotopes, except Pm, which is radioactive. The characteristic stable oxidation state of the lanthanide elements is +3 with $[Xe]4f^n$ ($n = 0-14$) as electronic configuration. The valence electrons in the $4f$ orbitals are shielded by the $5s$ and $5p$ electrons, which makes the formation of covalent bonds with donor atoms of ligands virtually impossible. In this respect, they contrast with the cations of the d-block transition elements, which have the valence electrons in the outer shell. Consequently, the interactions between Ln^{3+}-cations and ligands are largely electrostatic and the coordination numbers (CNs) and complex geometries are largely determined by steric factors and almost not by electronic ones. CNs in the range 3–12 have been observed for Ln-complexes with 8 and 9 as the most common ones. Since the $4f$ valence electrons are hidden below the $5s$ and $5p$ electrons, the 15 lanthanide cations are chemically very similar and these cations resemble Ca^{2+}, which has about the same size, but a lower charge. The Ln^{3+}-ions behave as hard Lewis acids and therefore, have a preference for ligands with highly electronegative donor sites.

Due to poor shielding by the $4f$ electrons, the effective nuclear charge is increasing steadily across the lanthanide series, which results in a gradual decrease of the ionic radius going from La^{3+} to Lu^{3+} (Fig. 2) [4]. Consequently, the charge density of the Ln^{3+}-cations increases across the series as, for example, reflected in the pK_{a1} values of the Ln^{3+}-aquo complexes, which decrease from 8.5 to 7.6 upon going from La^{3+} to Lu^{3+} [5]. Often, the geometries of complexes of a particular ligand with the various Ln^{3+}-ions are nearly isostructural [6]. Any deviations from isostructurality

can generally be attributed to the lanthanide contraction and/or the accompanying increase in charge density.

In addition to a large chemical similarity, the lanthanides, fortunately, show an extraordinary diversity in physical properties that provides a wealth of information about the structures and dynamic behavior of Ln-compounds. The elements flanking the series (La^{3+} and Lu^{3+}) are diamagnetic because they lack unpaired electrons, whereas the elements in between have exclusively unpaired electrons in the $4f$ orbitals and are thus paramagnetic. Each of the paramagnetic Ln^{3+}-ions provokes characteristic effects on the NMR parameters of the surrounding nuclei. Spin-orbit coupling effects are very important for these ions. As a result, Dy^{3+} and Tb^{3+} are the most paramagnetic stable metal ions in the Periodic Table, having higher effective magnetic moments than Gd^{3+} with seven unpaired electrons. Furthermore, the Ln^{3+} ions have intriguing optical properties that also can be utilized for structural analysis. The insights of the coordination chemistry of lanthanide complexes are being exploited in many applications, including catalysis, biomedical diagnosis and therapy, and environmental chemistry.

Much progress has recently been made in the development of computational methods for Ln^{3+}-complexes. Nowadays, reliable methods exist for the evaluation of physical parameters and of geometries of Ln^{3+}-complexes. Computational methods are being exploited to support the interpretation of experimental data.

In this review, after an overview of the tools that can be used to elucidate the structure and dynamics of Ln^{3+}-complexes, we describe some examples of the consequences of the lanthanide contraction. The focus will be on the structure and dynamics of aqueous systems with coordination numbers 8 and 9.

2. Analytical techniques for the elucidation of the structure and dynamics of Ln^{3+}-complexes

2.1. X-ray and neutron scattering

X-ray crystallography can give accurate pictures of the static molecular structures of Ln^{3+}-complexes, which may be applied as an initial guess for the evaluation of solution data obtained by other techniques, such as DFT (density functional theory) calculations. Often, in crystals, Ln^{3+}-complexes occur as self-associates. The comparable structure in aqueous solution can then be
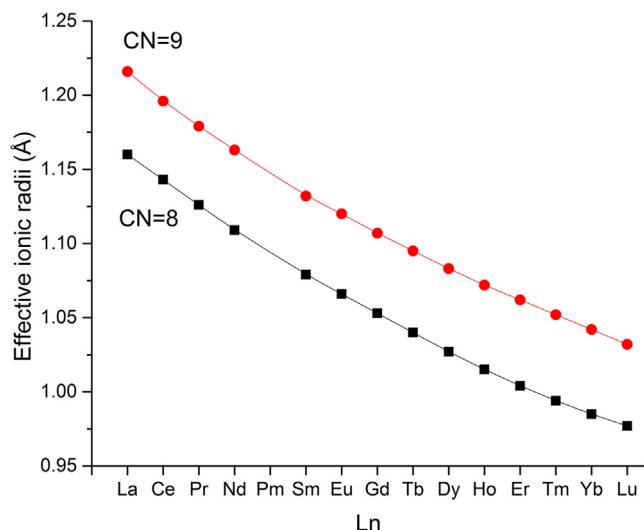

Fig. 1. The long Periodic Table of elements.

Fig. 2. Effective ionic radii of 8- and 9-coordinated Ln^{3+}-ions [4].

estimated by replacing bridging donor atoms by water ligands or by vacant donor atoms of a remaining ligand. Structural trends along the Ln-series observed in X-ray crystal structures have been recently reviewed by Cotton and Raithby [7].

Recently, much progress has been made in the application of X-ray absorption experiments, such as EXAFS (extended X-ray absorption fine structure) and XANES (X-ray absorption near edge structure), to investigate the structures of Ln^{3+}-complexes in solution. Usually, these techniques are combined with computational techniques including ab initio, molecular mechanics, MD (molecular dynamics) and DFT calculations for the fitting of the data [8,9].

Neutron diffraction difference spectroscopy has been used to establish that the CN for the Ln-aquo complexes decreases from 9 to 8 across the series [10,11].

2.2. NMR spectroscopy

The paramagnetic Ln^{3+}-ions in Ln^{3+}-complexes induce substantial shift and relaxation effects in coordinated ligand nuclei. The magnitudes of these effects are dependent on the spatial orientation of the nuclei with respect to the central Ln^{3+}-ion and they are different for the various lanthanides. Therefore, collection of data of complexes of a particular ligand with various lanthanides can provide a wealth of structural information.

2.2.1. Lanthanide induced NMR shifts

The bound value of the lanthanide induced shift (LIS) of a ligand nucleus upon coordination to an Ln^{3+}-ion (Δ) can be dissected into four contributions: the bulk magnetic susceptibility shift (Δ_χ), the diamagnetic (Δ_{dia}), the pseudocontact (Δ_{pc}), and the contact shift (Δ_{con}) (Eq. (1)).

$$\Delta = \Delta_\chi + \Delta_{dia} + \Delta_{pc} + \Delta_{con} \tag{1}$$

The magnitude of Δ_χ expressed in ppm for a lanthanide compound in a standard NMR sample tube placed parallel to the applied magnetic field can be approximated by Eq. (2), where c is the Ln^{3+}-ion concentration in mol L^{-1}, T represents the absolute temperature, and μ_{eff} is the effective magnetic moment of the Ln^{3+}-ion under study. The magnitude of Δ_χ is the same for all nuclei in a sample and thus independent of the structure of the Ln^{3+}-complex. In a standard NMR tube (single compartment), Δ_χ can be canceled by frequency-locking of the spectrometer or by determining the chemical shifts with respect to an internal stan-

dard. Moreover, Δ_χ can be measured easily by applying an external reference put in a co-axial inner tube. The value of Δ_χ can then be utilized to evaluate c by Eq. (2) [12].

$$\Delta_\chi = \frac{4000\pi c}{3T}\left(\frac{\mu_{eff}}{2.84}\right)^2 \tag{2}$$

Diamagnetic contributions are usually relatively small, except for the donor nuclei [13]. They are due to, for example, conformational changes upon coordination of the ligand, inductive effects, and direct field effects. The values of Δ_d can be estimated from the shifts of the corresponding diamagnetic La^{3+}- or Lu^{3+}-complexes (electron configurations $4f^0$ and $4f^{14}$, respectively), by interpolating these shifts, or from the induced shift of the comparable Y^{3+}-complex, which is also diamagnetic.

The contact shift results from unpaired spin density created by the Ln^{3+} f-orbital that is transmitted to the ligand nucleus under study by direct spin delocalization and/or by spin polarization. Its magnitude (in ppm) is given by Eq. (3), where $< S_z >$ is the reduced value of the average spin polarization, μ_B the electron Bohr magneton, k the Boltzmann constant, γ_I the magnetogyric ratio of the nucleus in question, and $A/\hbar$ the hyperfine coupling constant (in rad s^{-1}). Golding and Halton have calculated $< S_z >$ values for the various paramagnetic Ln^{3+}-ions at 300 K, taking into account bonding effects, mixing of excited states into the ground state, and spin–orbit couplings (ξ) as obtained by Hartree-Fock calculations [14]. Pinkerton et al. have computed somewhat refined $< S_z >$ values by employing ξ-values obtained by relativistic Hartree-Fock calculations [15]. The values for Eu^{3+} and Sm^{3+} appeared to be very sensitive to the choice of the spin–orbit coupling and therefore, for these ions, the authors have proposed experimental values. In both approaches, it is implicitly assumed that crystal-field effects are negligible at normal temperatures [16]. More recently, $<S_z>$ values for Ln^{3+}-complexes of 4-ethyl-2,6-dipicolinate ($Ln(4\text{-Et-DPA})_3$, see below) were evaluated by SO-CASSCF calculations (SO-CASSCF = spin-orbit complete active space self-consistent field) [17]. A comparison of the various sets of $<S_z>$ values (see in Table 1) shows that the relative variations among them are largest for the light lanthanides, particularly for Eu^{3+} and Sm^{3+}, which can be ascribed to the high sensitivity of $<S_z>$ for variations in ξ.

$$\Delta_{con} = \langle S_z \rangle \frac{\mu_B}{3kT\gamma_I} \frac{A}{\hbar} 10^6 \tag{3}$$

The magnitude of Δ_{con} is always very large for donor atoms of a ligand but declines steeply with an increasing number of bonds separating the Ln^{3+}-ion and the observed nucleus [13].

Table 1
Values of $< S_z >$ and C_j for paramagnetic Ln^{3+}-ions at 300 K.

Ln	$<S_z>$[a]	$<S_z>$[b]	$<S_z>$[c]	C_j[d]
Ce	−0.979	−0.974	−0.78	−6.3
Pr	−2.972	−2.956	−2.83	−11.0
Nd	−4.487	−4.452	−4.12	−4.2
Sm	0.063	0.224	0.39	−0.7
Eu	10.682	7.569	11.12	4.0
Gd	31.500	31.500	31.50	0
Tb	31.818	31.853	30.38	−86
Dy	28.545	28.565	27.93	−100
Ho	22.629	22.642	22.36	−39
Er	15.374	15.382	15.56	33
Tm	8.208	8.210	8.49	53
Yb	2.587	2.589	2.66	22

[a] For free Ln^{3+}, Ref. [14].
[b] For free Ln^{3+}, Ref. [15].
[c] For $Ln(4\text{-Et-DPA})_3$, Ref. [17].
[d] Reference [18]. Scaled to −100 for Dy.

The pseudocontact or dipolar shift of ligand nuclei in a paramagnetic Ln^{3+}-complex is caused by magnetic susceptibility anisotropy due to disturbance of the spherical symmetry around the Ln^{3+}-ion by crystal-field effects. For Gd^{3+}, Δ_{pc} is always negligible because its spherical $^8S_{7/2}$ ground state does not experience crystal-field splitting under first-order conditions. However, for all other paramagnetic Ln^{3+}-ions, Δ_{pc} of ligand nuclei is usually considerable up to an Ln-nucleus distance of about 40 Å [19]. Δ_{pc} (in ppm) can be expressed by the magnetic susceptibility tensors given in Eqs. (4)–(6) [20,21], where, r, θ, and φ are the spherical coordinates of the nucleus under study referred to the principal axes of the tensor centered on the Ln^{3+}-ion, and $\Delta\chi_{ax}$ and $\Delta\chi_{rh}$ are the axial and the rhombic anisotropy parameters. In the special case of axial symmetry, $\Delta\chi_{rh}$ = 0. Eqs. (4)–(6) can be expressed in several other ways [22], for example with an Ln^{3+}-complex fixed coordinate system using the five components of the magnetic susceptibility tensor [23].

$$\Delta_{pc} = \frac{10^6}{12\pi r^3}\left[\Delta\chi_{ax}(3\cos^2\theta - 1) + \frac{3}{2}\Delta\chi_{rh}\left(\sin^2\theta\cos 2\varphi\right)\right] \quad (4)$$

$$\Delta\chi_{ax} = \chi_{zz} - \frac{\chi_{xx} + \chi_{yy}}{2} \quad (5)$$

$$\chi_{rh} = \chi_{xx} - \chi_{yy} \quad (6)$$

Bleaney has approximated Δ_{pc} by applying the assumptions that the crystal-field splittings of the ground state of the J-multiplet are small compared to kT, the unpaired electrons are point charges at the origin, and the orientation of the main susceptibility axes is the same for all paramagnetic Ln^{3+}-ions in a series of complexes with a given ligand [20]. If the principal magnetic axis system is used, Δ_{pc} can be expressed as Eq. (7). Here, C_j is a constant, which is characteristic of the Ln^{3+}-ion and B_0^2 and B_2^2 are second-order crystal-field coefficients. The crystal-field coefficients of a Eu^{3+}-complex can independently be calculated by analysis of its emission spectrum [24,25]. For systems containing an n-fold symmetry axis with $n \geq 3$, the second term in Eq. (7) averages out when the chemical exchange between the nuclei concerned is fast on the NMR time scale. For Sm^{3+}, the pseudocontact shift (PCS) values, besides the ground state, also reflect the first excited $J = 7/2$ state. For Eu^{3+}, the excited energy levels with $J = 2$ and $J = 1$ are only 1200 and 400 cm^{-1} above the ground state ($J = 0$) and, therefore, also contribute to the PCS. As a result, the PCS has a complicated temperature dependence. Relative values of C_j have been tabulated by Bleaney et al. (see Table 1) [18].

$$\Delta_{pc} = \frac{C_j\mu_0\mu_B^2}{60k^2T^2}\left[\frac{(3\cos^2\theta - 1)B_0^2}{r^3} + \frac{\left(\sin^2\theta\cos 2\varphi\right)B_2^2}{r^3}\right] \quad (7)$$

The general validity of Bleaney's presumptions has often been questioned [26,27]. For example, the crystal-field splitting may be larger than kT, values of >1000 cm^{-1} have been reported [28]. The point dipole approximation may also be unjustified because the electron density distribution is not always spherical. Actually, Eu^{3+}, Yb^{3+}, Tm^{3+} and Er^{3+} have a prolate f electron density distribution, whereas Ce^{3+}, Pr^{3+}, Nd^{3+}, Tb^{3+}, and Dy^{3+} have an oblate distribution [29]. The principal directions of the susceptibility tensor can be differently oriented for the various Ln^{3+}-ions, leading to different angles θ, and φ in Eq. (7) within a set of complexes with the same ligand [30]. For example, measurements at low temperature (2 K) have shown that the main axis in the $[Ln(DOTA)(H_2O)]^-$ series changes in orientation with up to 90° between Tb and Yb [31]. It moves from almost perpendicular to the $Ln-O_{water}$ direction for Dy and Tb, to approximately parallel to it for Yb and Er. This effect is probably related to a different adaptation of the ligand geometry to the electron density distribution (prolate or oblate) of the Ln^{3+}-ions. If the assumption that the ligand field splitting is small compared to the spin–orbit coupling is not valid, the $\Delta\chi_{ax}$ values will depend not only on the specific Ln^{3+}-ion but also on the geometry of its coordination polyhedron. This has been observed for several metal complexes with relatively large ligand field splittings [27].

Despite these limitations, Eq. (7) has often been applied for the evaluation of solution structures of Ln^{3+}-complexes. However, a more rigid approach is the evaluation of the susceptibility tensor, for example, by fitting experimental data to Eqs. (4)–(6). Nowadays, this approach has become quite popular thanks to the great progress in computational methods to model possible structures, assign NMR spectra [30], and evaluate magnetic parameters [32].

2.2.2. Separation of contact and pseudocontact shifts and checks on isostructurality and invariability of parameters

Correction of LIS values for diamagnetic and susceptibility contributions affords the paramagnetic shifts, also known as the hyperfine shifts (Δ'). Evaluation of chemical structures of Ln^{3+}-complexes by analysis of LIS data may need Δ' to be separated into Δ_{pc} and Δ_{con} [16,33–37]. The Δ' for Gd^{3+}-complexes are exclusively of contact origin, but the resonances are generally severely broadened, which makes their accurate determination impossible. Since the ratio $|C_j/\langle S_z\rangle|$ for Ln = Yb is maximal (see Table 1), the ratio $|\Delta_{pc}/\Delta_{con}|$ is usually maximal as well, which allows assuming that Δ_{con} is negligible for ligand nuclei separated by at least four single bonds from the binding site. For other Ln^{3+}-ions a larger separation is required for such an assumption. Otherwise, a separation of the shift contributions is required. To that aim, it may be useful to consider the complex in the principal magnetic axes system. Then Eqs. (3) and (7) can be rewritten as Eqs. (8) and (9). Here, $\langle S_z\rangle$ and C_j are characteristic of the Ln^{3+}-ion but independent on the ligand nucleus, while F and D are dependent of the hyperfine coupling constant, the ligand geometry, the crystal-field coefficients, and the temperature. For a series of isostructural Ln^{3+}-complexes Eq. (8) can be linearized to Eqs. (10) and (11) [38]. Plots according to these equations are straight lines with F and D as slopes, respectively. Obviously, due to the lanthanide contraction, a series of Ln^{3+}-complexes is almost never perfectly isostructural. Gradual tiny changes in geometries across the series are usually reflected in a tiny break in the straight lines, approximately halfway through the series, because of the amplification of the effect due to the relatively large C_j-values of the heavier lanthanides. Drastic changes in geometries, hyperfine coupling constants, or crystal-field coefficients across the Ln^{3+}-series result in large deviations from linearity [39].

$$\Delta' = \Delta_{pc} + \Delta_{con} = \langle S_z\rangle F + C_j D \quad (8)$$

$$D = B_0{}^2 G_{ax} + B_2{}^2 G_{rh} \quad (9)$$

$$\frac{\Delta'}{C_j} = \frac{\langle S_z\rangle}{C_j}F + D \quad (10)$$

$$\frac{\Delta'}{\langle S_z\rangle} = F + \frac{C_j}{\langle S_z\rangle}D \quad (11)$$

For (effective) axially symmetric complexes (G_{rh} = 0), it is possible to factor out B_0^2, if Δ'-data for at least two ligand nuclei are available [16,34,40]. It is important to note that the elimination of B_0^2 is only possible if the F-values of the ligand nuclei considered are invariant for the set of lanthanides under study [34]. For example, Eq. (12) can be derived, where the subscripts i and k denote two different ligand nuclei, a relates to the Ln^{3+}-ion concerned, and $R_{i,k}$ = G_i/G_k. Accordingly, plots of $\Delta'_{i,a}/\langle S_z\rangle_a$ versus

$\Delta'_{k,a}/<S_z>_a$ should give straight lines for isostructural complexes with relative G-values $(R_{i,k})$ as the slope and $(F_i - R_{i,k}F_k)$ as the intercept. Variations in structure or in F along the Ln^{3+}-series show up as deviations from linearity, whereas variations in B_0^2 have no effect. If Δ'-data for at least three ligand nuclei are available, it is possible to extend this approach to afford Eqs. (13)–(16) in which both B_0^2 and $<S_z>$ are eliminated [41]. These equations can all be used as tests for isostructurality, which has been demonstrated for many complexes of series of Ln^{3+}-ions with rigid ligands [16].

$$\frac{\Delta'_{i,a}}{\langle S_z \rangle_a} = (F_i - R_{i,k}F_k) + \frac{R_{i,k}\Delta'_{k,a}}{\langle S_{za} \rangle_a} \tag{12}$$

$$\frac{\Delta'_i}{\Delta'_j} = \alpha \frac{\Delta'_k}{\Delta'_j} + \beta \tag{13}$$

$$\alpha = \frac{(S_{i,j} - R_{i,j})}{(S_{k,j} - R_{k,j})} \tag{14}$$

$$\beta = \frac{(S_{k,j}R_{i,j} - S_{i,j}R_{k,j})}{(S_{k,j} - R_{k,j})} \tag{15}$$

$$S_{i,j} = \frac{F_i}{F_j} \tag{16}$$

In graphical representations, the mathematical manipulations applied with the linear equations described above can smoothen as well as amplify effects of variations in the parameters or of inaccuracies in experimental data, because there is a large difference in magnitude of both $<S_z>$ and C_j between the first and second half of the series (see Table 1). Often, breaks are observed around Gd^{3+}, which therefore should be interpreted with great care. Furthermore, it may be advisable to exclude experimental shifts for Sm^{3+} because they are usually very small. Moreover, one should be aware that the conditions under which the Bleaney equations can be applied are not always fulfilled [42].

Alternatively, computational methods can be applied to calculate the structures and the related spin densities of Ln^{3+}-complexes. The spin densities can then be applied to calculate hyperfine coupling constants and contact shifts [43].

2.2.3. Lanthanide-induced relaxation rate enhancements

Paramagnetic Ln^{3+}-ions accelerate both the longitudinal and transverse relaxation rates ($R_1 = 1/T_1$ and $R_2 = 1/T_2$, respectively). The relaxation enhancements comprise an inner-sphere and a usually negligibly small outer-sphere contribution. The line-broadening of ligand nuclei in Gd^{3+}-complexes is often impractically large, particularly at distances from the Gd^{3+}-ion smaller than 10–15 Å. Therefore, structural investigations are usually carried out with the other paramagnetic Ln^{3+} ions. The R_1-values need to be corrected for the diamagnetic contributions, for example, by subtracting (interpolated) values of R_1-values for the corresponding La^{3+}, Lu^{3+}, or Y^{3+}- complexes. The resulting paramagnetic contribution for these Ln^{3+}-ions ($Ln \neq Gd$) is dominated by the dipolar ($R_{i,dip}$) and the Curie susceptibility mechanisms ($R_{i,Curie}$) [44].

The dipolar contribution is caused by the random fluctuations of the electronic field and may be modeled by Solomon-Bloembergen-Morgan (SBM) equations (Eqs. (17) and (18)) [45–47] when it is assumed that the reorientation of the complex is magnetically and geometrically isotropic. Here, τ_C is the correlation time given by $\tau_C^{-1} = \tau_R^{-1} + \tau_M^{-1} + T_{ie}^{-1}$ (i = 1,2), τ_R is the rotational correlation time, τ_M, the residence time of the ligand in the first coordination sphere of the Ln-cation (the reciprocal of

the ligand exchange rate, k_{ex}), and T_{ie}, the longitudinal or transverse electronic relaxation time. Typically, $\tau_R > 10^{-11}$ s, $\tau_M > 10^{-9}$ s and $T_{ie} \approx 10^{-13}$ s. Then, Eqs. (17) and (18) simplify to Eq. (19).

$$R_{1,dip} = \frac{2}{15}\left(\frac{\mu_0}{4\pi}\right)^2 \frac{\gamma_I^2 \mu_{eff}^2}{r^6}\left(\frac{3\tau_c}{1 + \omega_I^2 \tau_c^2} + \frac{7\tau_c}{1 + \omega_S^2 \tau_c^2}\right) \tag{17}$$

$$R_{2,dip} = \frac{1}{15}\left(\frac{\mu_0}{4\pi}\right)^2 \frac{\gamma_I^2 \mu_{eff}^2}{r^6}\left(4\tau_c + \frac{3\tau_c}{1 + \omega_I^2 \tau_c^2} + \frac{13\tau_c}{1 + \omega_S^2 \tau_c^2}\right) \tag{18}$$

$$R_{1,dip} = R_{2,dip} = \frac{4}{3}\left(\frac{\mu_0}{4\pi}\right)^2 \frac{\gamma_I^2 \mu_{eff}^2}{r^6}T_{ie} \tag{19}$$

The Curie relaxation is another dipolar mechanism due to an interaction between the nuclear spin and the thermal average of the electronic spin [48]. Eqs. (20) and (21) have been derived for it.

$$R_{1,Curie} = \frac{6}{5}\left(\frac{\mu_0}{4\pi}\right)^2 \frac{\omega_I^2 \mu_{eff}^4}{(3kT)^2 r^6}\left(\frac{\tau_R}{1 + \omega_I^2 \tau_R^2}\right) \tag{20}$$

$$R_{2,Curie} = \frac{1}{5}\left(\frac{\mu_0}{4\pi}\right)^2 \frac{\omega_I^2 \mu_{eff}^4}{(3kT)^2 r^6}\left(4\tau_R + \frac{3\tau_R}{1 + \omega_I^2 \tau_R^2}\right) \tag{21}$$

The Curie mechanism is often the predominant dipolar contribution for $Ln^{3+} \neq Gd^{3+}$, especially at strong magnetic fields. It should be noted that the above equations strictly only hold under certain conditions, including isotropic magnetic susceptibility and zero-field splitting that is smaller than the electronic Zeeman interaction (Zeeman limit). Outside these limits, a proper description of the relaxation phenomena requires more complicated approaches [49,50]. The effect of the anisotropy of the magnetic susceptibility tensor of these Ln^{3+} ions on the Curie relaxation was originally considered by Vega and Fiat [51]. Recently, Suturina et al. presented some relatively simple equations that take anisotropic nuclear relaxation into account, in both dipolar and Curie mechanisms (Eqs. (22)–(28)) [52]. Here, $\hat{r}$ is the unit vector oriented in the same direction as vector r, $\boldsymbol{G}(\omega)$ is the spectral power density tensor describing the statistics of both the dynamics of the molecular rotation and the electron magnetic dipole (Eqs. (22) and (23)). In Eqs. (25) and (26), Δ_σ^2 and Λ_σ^2 are the first and the second rank invariant of the total chemical shielding tensor, respectively, which are given by Eqs. (27) and (28).

$$R_{1,dip} = \frac{2}{3}\left(\frac{\mu_0}{4\pi}\right)^2 \frac{\gamma_I^2}{r^6} Tr\left[\left(3\hat{r}\cdot\hat{r}^T - 1\right)^2\right]\boldsymbol{G}(\omega_I) \tag{22}$$

$$R_{2,dip} = \frac{1}{3}\left(\frac{\mu_0}{4\pi}\right)^2 \frac{\gamma_I^2}{r^6} Tr\left[\left(3\hat{r}\cdot\hat{r}^T - 1\right)^2\right](\boldsymbol{G}(0) + \boldsymbol{G}(\omega_I)) \tag{23}$$

$$\boldsymbol{G}(\omega)\int_0^\infty \boldsymbol{G}(\tau)e^{-\tau/\tau_R}d\tau \tag{24}$$

$$R_{1,Curie} = \frac{1}{2}\Lambda_\sigma^2 \omega_I^2 \frac{\tau_R}{1 + 9\omega_I^2 \tau_R^2} + \frac{2}{15}\Delta_\sigma^2 \omega_I^2 \frac{\tau_R}{1 + \omega_I^2 \tau_R^2} \tag{25}$$

$$R_{2,Curie} = \frac{1}{4}\Lambda_\sigma^2 \omega_I^2 \frac{\tau_R}{1 + 9\omega_I^2 \tau_R^2} + \frac{1}{45}\Delta_\sigma^2 \omega_I^2 \left(4\tau_R + \frac{3\tau_R}{1 + \omega_I^2 \tau_R^2}\right) \tag{26}$$

$$\Lambda_\sigma^2 = (\sigma_{xy} - \sigma_{yx})^2 + (\sigma_{xz} - \sigma_{zx})^2 + (\sigma_{yz} - \sigma_{zy})^2 \tag{27}$$

$$\Delta_\sigma^2 = \sigma_{xx}^2 + \sigma_{yy}^2 + \sigma_{zz}^2 - \sigma_{xx}\sigma_{yy} - \sigma_{xx}\sigma_{zz} - \sigma_{yy}\sigma_{zz}$$
$$+ \frac{3}{4}\left[(\sigma_{xy} + \sigma_{yx})^2 + (\sigma_{xz} + \sigma_{zx})^2 + (\sigma_{yz} + \sigma_{zy})^2\right] \tag{28}$$

2.3. Computational methods

Computational methods have emerged in the last two decades as very powerful tools to investigate the structure and properties of metal complexes, including complexes of the Ln^{3+}-ions. The advances in methodological and technical aspects (algorithms, software...), together with the increasing computational resources, allow modeling rather large systems to unprecedented accuracy. In principle, Ln^{3+}-complexes can be investigated using the complete set of computational chemistry methods, including 1) calculations based on molecular mechanics and (classical) molecular dynamics methods, and 2) methods based on electronic structure theory. The latter group includes semiempirical and ab initio methods, as well as calculations based on density functional theory (DFT) [53].

Molecular mechanics and classical molecular dynamics calculations are based on the laws of classical physics. The energy of the system is described by a force field, an expression that relates the potential energy of the system, and a series of terms to account for the contributions of atoms linked by covalent bonds, as well as terms that consider interactions between non-bonded atoms like electrostatic and van der Waals interactions [54]. Besides the functional form of the potential energy, a force field includes a set of parameters for each type of atom considered to develop the force field. Parametrization of the force field is usually performed on the basis of empirical data or quantum mechanical calculations [55]. The application of molecular mechanics methods to investigate Ln^{3+}-complexes is hampered by the lack of parametrization of the Ln^{3+}-ions in the most common force-fields. As a result, the structures of small Ln^{3+}-complexes are more often investigated using semiempirical or DFT methods. Nevertheless, force field methods have been successfully applied to investigate different chemical problems, in particular, the dynamics of Gd^{3+}-complexes relevant as MRI contrast agents [56,57]. Classical molecular dynamics calculations have the advantage of their low computational cost, so long as simulation times are accessible.

The simplest approach to electronic structure theory is by quantum–chemical semiempirical methods, which use parametrization and integral approximations to make calculations more efficient [58]. Semiempirical parameters within the Sparkle model were developed to be used with the Parametric Method number 7 (PM7), which allows the prediction of the geometries of metal complexes containing lanthanide ions with average unsigned errors for the prediction of Ln–O and Ln–N distances <0.09 Å [59]. A more robust semiempirical method, denoted as Recife Model 1 (RM1), capable of predicting also Ln–C, Ln–S, Ln–Cl and Ln–Br distances, was proposed and applied to investigate different lanthanide complexes [60]. A semiempirical method based on the tight binding electronic structure approach (GFN-xTB) was parametrized for all elements up to $Z = 86$, and thus includes the whole lanthanide series [61]. Semiempirical calculations have the advantage that they can be used to investigate rather large lanthanide complexes, containing several hundreds of atoms. Furthermore, these semiempirical calculations are also useful to investigate the conformational space of smaller lanthanide complexes, which may be afterward studied at a higher computational level.

The advent of modern functionals has made DFT the most common method selected to investigate the structures and energies of lanthanide complexes. DFT methods rely on the Hohenberg-Kohn theorem, which states that the electron density of the system provides access to the energy and all electronic properties of the molecule [62]. However, the Hohenberg-Kohn theorem does not give the form of the functional (a function of a function) that should afford the exact energy from the exact electron density. As a result, many different functionals were developed during the last two

decades. These modern functionals allow a very accurate description of the structures and many properties of lanthanide complexes. DFT incorporates electron correlation with the exchange correlation potential, which is usually separated into two parts, denoted as the exchange and correlation parts, accounting for the interactions between electrons with the same spin and different spin, respectively. The different functionals developed so far can be classified in six different groups [63]: 1) LDA functionals: they rely on the local density approximation (LDA), which expresses the energy of the system as a function of the electron density at each point in space $\rho(r)$; 2) GGA functionals: based on the generalized gradient approximation (GGA), and depend both on the electron density and derivatives of the electron density $\nabla\rho(r)$; 3) meta-GGA functionals: they depend on the electron density, its gradient, and higher derivatives of the electron density; 4) hybrid functionals: they include the hybrid GGA and hybrid meta-GGA functionals, and contain a fraction of the non-local Hartree-Fock exchange; 5) double-hybrid functionals, which include non-local correlation effects through second-order perturbation treatment (i.e. MP2); 6) long-range corrected functionals, which use a short term to include the DFT exchange interaction and a second term to account for long-range interactions. Benchmark studies showed that meta-GGA (mPWB95, BB95, and TPSS) and hybrid meta-GGA functionals (TPSSh, M06) perform substantially better than the hybrid GGA and GGA functionals in predicting the geometries of Ln^{3+}-complexes [64]. Some hybrid GGA functionals (i.e. B3PW91 and BH&HLYP) also perform well, providing better results than the popular B3LYP functional. GGA functionals and functionals based on the LDA approximation should not be used to obtain accurate geometries of Ln^{3+}-complexes. The DFT-based molecular dynamics Car-Parrinello method [65] was also proved to be very useful to investigate the dynamics of Ln^{3+}-complexes, for instance, water exchange processes or the dynamics of the zero-field splitting or hyperfine interactions [66–68].

The computational treatment of Ln^{3+}-complexes using DFT methods requires considering the main relativistic effects, which play an important role in compounds of these heavy elements. The most popular approach to introduce relativistic effects is the use of effective core potentials (ECPs). ECPs provide an efficient strategy to implicitly include relativistic effects using a formally non-relativistic framework. In the ECP approach, the explicit quantum-chemical description is limited to the valence electrons, which reduces the computational cost of the calculations, while relativistic effects are implicitly incorporated by an adequate adjustment of the several parameters in the valence model Hamiltonian [69]. The most common ECPs used in computational studies of Ln^{3+}-complexes are those of the Stuttgart-Cologne family, for which two definitions are available: large-core, which considers the 4f-electrons as core electrons, and small-core, which treats the 4f-electrons explicitly [70,71]. The inclusion of the 4f-electrons in the core allows performing calculations using a pseudo-singlet state, which greatly reduces the computational effort [72]. This approach was found to be very effective to explore the structures and energetics of Ln^{3+}-complexes. Obviously, the small core approximation is required to study properties related to the 4f shell, as for instance the calculation of hyperfine coupling constants. Alternatively, all-electron calculations based on the Douglas-Kroll-Hess (DKH) method or the zero-order regular approximation (ZORA) can be applied for Ln^{3+}-complexes [73,74], being better suited to address some specific problems [75]. All-electron basis sets are available for both DKH and ZORA calculations [76–78].

The last years have witnessed important advances that made it possible to apply wave function calculations based on the Complete Active Space Self-Consistent Field (CASSCF) method to

relatively large systems [79]. All members of the lanthanide series except La^{3+} and Lu^{3+} have unpaired f-electrons, which results in the presence of different states with similar energy and thus in wave functions with multiconfigurational character. The CASSCF method provides a very convenient approach to model systems with multiconfigurational character by dividing the orbitals into three subspaces: i) an inactive space in which all orbitals are doubly occupied; ii) a second subspace known as the active space for which a full configuration interaction expansion is considered (The occupation number of these orbitals should be a non-integer number between 0 and 2); iii) a virtual space with the orbitals that are kept unoccupied. In the particular case of the Ln^{3+} ions [80,81], calculations based on CASSCF(n,7) wave functions (an active space defined by the n electrons distributed in the seven $4f$ orbitals) incorporating spin–orbit coupling effects (SO-CASSCF), were found to be particularly useful to investigate magnetic properties, including the magnetic anisotropy responsible for the pseudocontact shifts described above [32], and the zero-field splitting energy [82].

2.4. Evaluation of hydration numbers of Ln^{3+}-complexes in aqueous solution

Understanding of the coordination chemistry of lanthanides in aqueous solutions as the result of the very subtle changes in electronic configuration from La^{3+} to Lu^{3+} is not comprehensive without insights into hydration mechanisms. Association/dissociation reactions of non-charged water molecules exclude potentiometric methods to study hydration equilibria in solution, implying that alternative methodologies are needed for the quantitative description of the hydration changes across the series of lanthanides.

An accurate assessment of the hydration state is essential for the evaluation of the relaxation behavior of paramagnetic Ln^{3+}-ions. Both, the longitudinal and the transverse inner-sphere proton relaxation rates are directly proportional to q, as described by Eqs. (29) and (30), where c is the concentration (mM) of a paramagnetic Ln^{3+}-complex, P_M is the mole fraction of bound water, $\Delta\omega_M$ is the chemical shift difference between the bound and free water molecules, and $(1/T_{1M})^{IS}$ and $(1/T_{2M})^{IS}$ are longitudinal and transverse relaxation rates of protons of the bound water molecules, respectively.

$$\left(\frac{1}{T_1}\right)^{IS} = \frac{cq}{55.5}\frac{1}{T_{1M}+\tau_M} = P_m\frac{1}{T_{1M}+\tau_M} \quad (29)$$

$$\left(\frac{1}{T_2}\right)^{IS} = \frac{P_M}{\tau_M}\frac{T_{2M}^{-2}+\tau_M^{-1}+T_{2M}^{-1}+\Delta\omega_M^2}{\left(\tau_M^{-1}+T_{2M}^{-2}\right)^2+\Delta\omega_M^2} \quad (30)$$

Fitting of the relaxation data measured at different magnetic fields with the SBM model (see above) can provide q, but besides being laborious, the method suffers from many uncertainties due to the involvement of multiple physical parameters. Solid-state structures of the Ln-complexes can offer direct information on the hydration numbers, but the results are often somewhat different from those found in disordered solution-states [83]. In the late 1970s, Horrocks and Sudnick have introduced a method to assess the number of water molecules in the first coordination sphere of Eu^{3+} and Tb^{3+} by measuring the luminescence lifetimes (τ) of the corresponding complexes dissolved in both H_2O and D_2O [84]. Direct laser-induced excitation of the f-electron levels results in $^5D_0 \rightarrow {}^7F_J$ and $^5D_4 \rightarrow {}^7F_J$ transitions ($J = 0$–6) for Eu^{3+} and Tb^{3+}, respectively, with the subsequent exponential decay of luminescence. The exponential decay rate constant ($k_{obs} = 1/\tau$) measured in the presence and absence of OH oscillators in the first coordination sphere can then be used to calculate q through a linear

dependence (Eq. (31)), with A_{Ln} being the lanthanide specific proportionality constant. Somewhat extended equations have been designed that take into account the effects of X-H oscillators and water molecules beyond the first coordination sphere [85,86]. In later studies, the same method was also applied successfully for the determination of q in Sm^{3+} and Dy^{3+} complexes [87].

$$q = A_{Ln}\left(\tau_{H_2O}^{-1}-\tau_{D_2O}^{-1}\right) \quad (31)$$

The coordination of water molecules directly to a paramagnetic Ln^{3+} ion has consequences on the ^{17}O NMR data of water. If the exchange between bound and unbound water molecules is fast on the NMR time scale, the ^{17}O NMR chemical shift of the coordinated water molecules (δ_M) relates to the observed shift (δ_{obs}) corrected for pure water via Eq. (32) [88]. As described in section 2.2, the ^{17}O shift of bound water can be dissected in three terms (Eqs. (1) and (8)) and the LIS of water (Δ) can be expressed as in Eqs. (33) and (34).

$$\delta_{obs} = \delta_\chi + q \cdot P_M \cdot \delta_M \quad (32)$$

$$\Delta = \frac{\delta_{obs}-\delta_\chi}{P_M} = q \cdot \delta_{dia} + q \cdot \delta_{con} + q \cdot \delta_{pc} \quad (33)$$

$$\Delta = q \cdot \delta_{dia} + q \cdot \langle S_Z \rangle \cdot F + q \cdot C_j \cdot G \quad (34)$$

The diamagnetic contribution is usually the smallest and can easily be eliminated by subtraction of the corresponding shifts of diamagnetic La^{3+} or Lu^{3+}-complexes. The contact shift, on the other hand, is the dominating one and can be used for the calculation of q [89]. The hyperfine coupling constant ($A/\hbar$) between the unpaired electrons of the Ln^{3+}-ion and the ^{17}O nucleus of water is in direct relation with F (Eq. (35)). It has been demonstrated that for the Ln^{3+}- bound ^{17}O nuclei, F and thus also $A/\hbar$, is practically independent of the character of the ligands and even of the nature of the Ln-bound O atom [90]; the value of $A/\hbar$ typically ranges within $(3.9 \pm 0.3) \times 10^6$ rad s^{-1}.

$$F = \frac{\mu_\beta}{3kT\gamma_O}\cdot\frac{A}{\hbar}\cdot 10^6 = \frac{6.172\cdot 10^{-3}}{T}\cdot\frac{A}{\hbar} \quad (35)$$

For Gd^{3+}, the PCS can also be neglected ($C_j = 0$) so that q can be calculated directly from the observed chemical shift, measured typically at 80 °C to ensure the fast exchange between the coordinated and free water molecules. When severe line broadening in the ^{17}O spectra hampers the accurate determination of q, Dy^{3+}-analogs can be used [88,90,91]. The contact contribution, in this case, is >85% [13], which enables the determination of q with the accuracy of ±0.2.

Whether or not q for Ln^{3+}-complexes of a specific ligand is constant across the Ln-series can be checked by plotting the ^{17}O LIS data for water in a linearized form of Eq. (34) (see Eq. (10)). A possible change in q can then be visualized by a break in the obtained linear plot, going from light ($q = 9$) to heavy ($q = 8$) lanthanides (see, for example, Fig. 6a, where $F = -84$ calculated for both lines, corresponding to $A/\hbar = -4.05 \times 10^6$ rad s^{-1} [92]).

3. Stability trends of Ln complexes

The thermodynamic stability of Ln^{3+}-complexes is a very relevant issue for different technological and medical applications. The smooth contraction of the ionic radii of the Ln^{3+}-ions across the series generally results in complexes with similar chemical properties, including their thermodynamic stabilities. As a result, the selective complexation of a particular Ln^{3+}-ion or group of Ln^{3+}-ions is not an easy task [93]. The trends in stability constants observed across the lanthanide series may fall in three different categories (Fig. 3): 1) in most cases stability constants increase
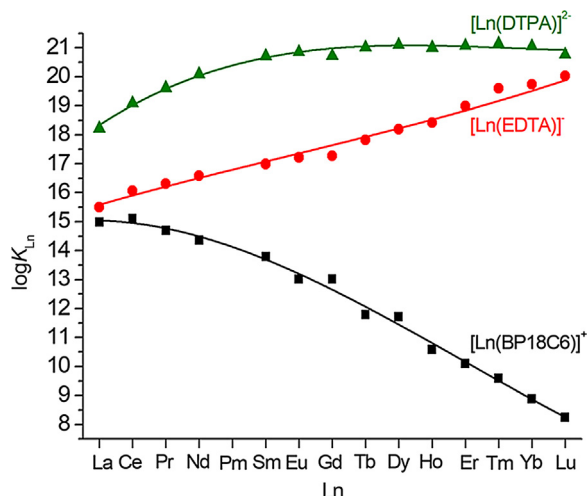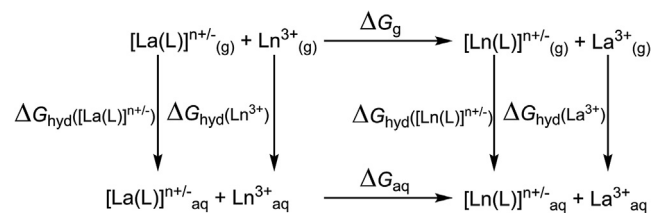
Fig. 3. Stability constants of Ln^{3+} complexes illustrating the different trends observed across the series. Data from [94–97].

Scheme 1. Thermodynamic cycle for the formation of a $[Ln(L)]^{n\pm}$ complex in aqueous solution ($[Ln(L)]^{n\pm}_{aq}$) from the La^{3+}-analog.

steadily across the lanthanide series, as it is the case of $[Ln(EDTA)]^-$ complexes [94]; 2) some ligands form complexes whose stability increases along the first part of the series, reaches a maximum and then remains constant or even decreases for the late lanthanides. A typical example of this trend is given by the [Ln(DTPA)]$^{2-}$ complexes [95]; 3) a few ligands form Ln^{3+}-complexes with decreasing stability on proceeding to the right across the series. The macrocyclic ligand derived from 1,10-diaza-18-crown-6 containing picolinate pendants BP18C6^{2-}, also known as MACROPA (Fig. 4), belongs to the last group, and provides the largest selectivity for the large Ln^{3+}-ions reported so far ($\Delta\log K_{Ln}$ = $\log K_{La}$- $\log K_{Lu}$ = 6.7) [96]. As a result, BP18C6^{2-} was proved to be very selective in providing size-discrimination for both the lanthanide and actinide ions [97] and was found to be well suited for the coordination of large ions such as Ac^{3+} and Ba^{2+} [98,99]. Rigidification of the macrocyclic unit by incorporating a cyclohexyl unit results in a similar stability trend [100]. Other ligands based on the 1,10-diaza-18-crown-6 functionalized with acetate or malonate pendant arms also show reversed stabilities with respect to the normal trend, though less marked [101,102]. Decreasing the

size of the crown ether to 1,10-diaza-15-crown-5 yields complexes with stabilities that remain nearly unchanged for the first half of the lanthanide series, then decrease for the smallest Ln^{3+}-ions [103,104].

The steady increase in stability along the series commonly observed for Ln^{3+}-complexes may be more pronounced in the case of rigidified acyclic ligands such as BCAED^{4-}, which presents a large selectivity for the small Ln^{3+}-ions with $\Delta\log K_{Ln}$ = $\log K_{La}$- $\log K_{Lu}$ = −8.2, a value that differs six orders of magnitude from that observed for the structurally related EGTA^{4-} ($\Delta\log K_{Ln}$ = −2.3) [105,106].

The stability trends across the lanthanide series may be rationalized using the thermodynamic cycle depicted in Scheme 1 [107]. This allows to express the Gibbs free energy associated to the formation of a general complex $[Ln(L)]^{n\pm}$ in aqueous solution ($[Ln(L)]^{n\pm}_{aq}$) from the La^{3+}-analog in terms of the Gibbs free energy in the gas phase (ΔG_g) and the hydration energies of the different species (see Eq. (36)).

$$\Delta G_{aq} = \Delta G_g + \Delta G_{hyd}([Ln(L)]^{n\pm}) + \Delta G_{hyd}([La^{3+}]) - \Delta G_{hyd}([Ln^{3+}]) - \Delta G_{hyd}([La(L)]^{n\pm}) \quad (36)$$

The hydration free energies of the Ln^{3+}-ions become more negative across the series owing to the increased charge density of the metal ion associated with the contraction in ionic radii, taking values of −788.1 kcal mol^{-1} for La^{3+} and −888.1 kcal mol^{-1} for Lu^{3+} [108,109]. On the other hand, hydration free energies remain almost constant for different lanthanide complexes with a given ligand, as demonstrated by DFT calculations for several series of Ln^{3+}-complexes [107,110]. Thus, the term $\Delta G_{hyd}([Ln(L)]^{n\pm})$ − $\Delta G_{hyd}([La(L)]^{n\pm})$ can be considered to provide a negligible
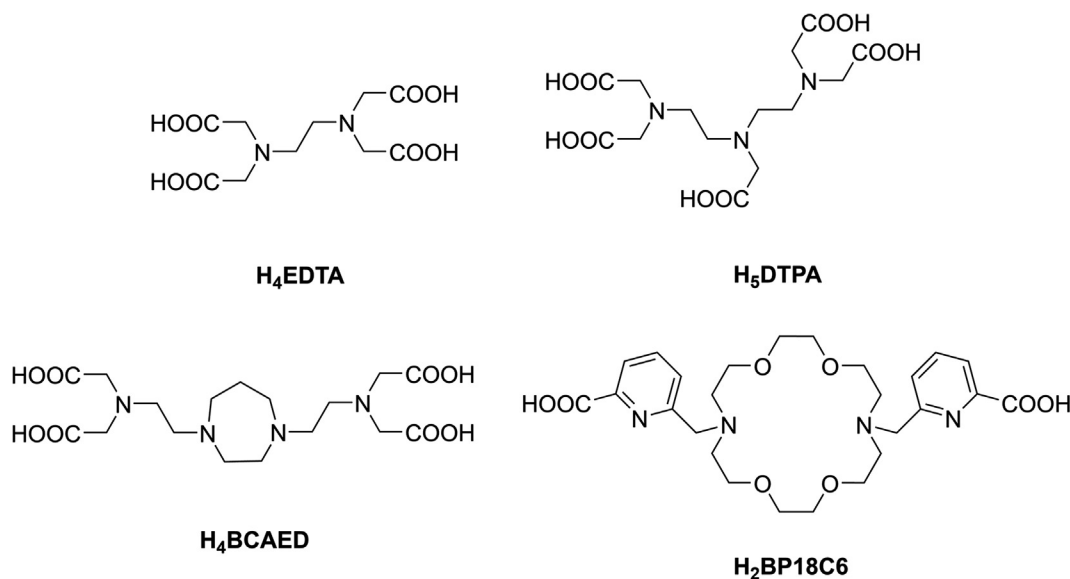

Fig. 4. Molecular structures of ligands discussed in Section 3.

contribution to the observed trend. As a consequence, the stability trend observed across the lanthanide series is the result of the balance between ΔG_g and the $\Delta G_{hyd}([La^{3+}]) - \Delta G_{hyd}([Ln^{3+}])$ term, which amounts to + 100 kcal mol^{-1} from La^{3+} to Lu^{3+}. DFT calculations demonstrated that the binding energy of polyaminocarboxylate ligands becomes more negative on going to the right across the series, as a result of an increased electrostatic interaction due to the lanthanide contraction, resulting in negative ΔG_g values [107,110]. In the absence of steric constraints for the coordination of smaller Ln^{3+} ions, the ΔG_g values compensate for the unfavorable contribution of the $\Delta G_{hyd}([La^{3+}]) - \Delta G_{hyd}([Ln^{3+}])$ term, as generally polyaminocarboxylates are better ligands than water for the Ln^{3+} ions. This explains the increasing stability along the $4f$ series of complexes with ligands such as EDTA^{4-} and most polyaminocarboxylates. Deviations from this general behavior occur with rigid macrocyclic ligands such as BP18C6^{2-}, which are better suited for the coordination of large metal ions. This was supported by DFT studies based on the large-core ECP approximation, which evidenced that some of the Ln–donor distances become longer along the $4f$ period in spite of the decreasing ionic radius of the Ln^{3+}-ion [36,96].

4. Examples

4.1. Lanthanide-aquo systems

The complex hydration behavior across the series of lanthanides in solution is based on the dipole-charge electrostatic interactions with solvent water molecules present in the first coordination sphere of the metal ions. The exact information about the Ln-complexes formed with the simplest ligand, water, such as stoichiometry (q), bond distances, bond angles, and thus the conformation and geometry of the complexes, can be assessed through solid-state and liquid state diffraction data coupled with theoretical models.

Already in the pioneering work on Ln-aquo complexes by Spedding et al., it was noticed that physicochemical properties of Ln-aquo systems showed the so-called 'gadolinium break': apparent molar volumes [111], heat capacities [112], and relative viscosities [113] displayed, in contrast to the ionic radii, a non-smooth variation across the Ln-series. The irregularities were the greatest around Gd^{3+}. It was hypothesized that these phenomena can be ascribed to the existence of equilibria between two Ln-aquo complexes with different q, where this equilibrium may be sharply displaced toward a lower CN below a critical ionic radius. Later, X-ray studies on concentrated LnCl$_3$ solutions in water (3 M) demonstrated that q = 9 for Ln = La, Pr, and Nd and q = 8 for Ln = Tb → Lu, whereas for Ln = Nd → Tb, the q-values are broken numbers between 8 and 9, probably due to an averaging between q = 9 and 8 [114,115].

The first EXAFS experimental data obtained on concentrated solutions of Ln^{3+}-perchlorates based on the analysis of the low-energy (5–10 keV) L$_3$-edge X-ray absorption spectra, also suggested a change of the hydration numbers from 9 (light Ln^{3+}) to 8 (heavy Ln^{3+}) with a break in the middle of the series (Sm^{3+}– Eu^{3+}) [116]. However, subsequent studies using the same method resulted in rather contradictory structural parameters, such as Ln–O bond lengths for complexes with the same q. Apparently, analysis of the low-energy spectra applied in the early investigations was less efficient compared to the additional high-energy (38–62 keV) K-edge analysis implemented in more recent studies [117]. Currently, the estimated mean distances between the Ln^{3+}-ions and the O-atoms of coordinated water molecules in the first coordination sphere are consistent among various studies (2.4 – 2.5 Å), with some deviations due to the accompanied coordination

geometry of the hydrated complexes (vide infra), and the number of water molecules directly coordinated to Ln^{3+}-ions (q) is no longer a subject of debate. The experimental data obtained from X-ray absorption spectroscopy, X-ray scattering, neutron diffraction, and optical spectroscopy, in combination with reliable theoretical models, evidence a smooth transition between nine- and eight-coordinated complexes, with the majority of the lanthanides having a non-integer hydration number [118]. Hence, a more realistic view is the assumption of the presence of hydration equilibria.

Today, a large number of crystal structures of Ln-aqua ions are reported in the literature. Most of the reported structures have CN = 8 or 9 [92]. The data show that the choice of the counter ion has an influence on the CN of the compound that crystallizes from solution. Anions with stronger coordination ability (e.g. Cl$^-$ and Br$^-$) [119] usually enter the first coordination sphere, while weak coordinators like ethyl sulfates (EtOSO$_3^-$), triflates (CF$_3$SO$_3^-$), and bromates generally rather show a preference for the second coordination sphere, both in the crystal structure and in aqueous solution [92,120]. For the latter complexes, 9-coordinated crystal structures have been reported. Crystal packing effects may lead to stabilization of deviating Ln-aquo structures, as is illustrated by the crystal structures Ln(ClO$_4$)$_3$·6H$_2$O (Ln = La, Tb, Er), where octahedral [Ln(H$_2$O)$_6$]$^{3+}$ entities are packed in a cubic close-packed arrangement with the ClO$_4^-$ anions occupying all holes in this lattice [121]. Overall in crystal structures, there is an apparent tendency for a decreasing number of coordinated water molecules upon the decrease of the ionic radius going from light to heavy lanthanides. An accompanying phenomenon is the decreasing average of Ln-water bond lengths observed in the structures exhibiting a $P6_3/m$ crystallographic space-group. Chemically complex counterions force the formation of crystals with low symmetry space groups, resulting in a larger variety of Ln-water bond lengths, which complicates structural investigations on such complexes [122].

Various solid-state studies demonstrate the coordination of nine water molecules for the light lanthanides arranged in a tricapped trigonal prism (TTP), with six bonds originating from O-atoms at the apexes of the trigonal prism (Ln—O(9P)), and three capping bonds (Ln—O(9C)). The heavy lanthanides coordinate eight water molecules (Ln—O(8)) in a square antiprism (SA) geometry (Fig. 5) [123]. Similar geometries are evident from the analysis of ^{17}O NMR data acquired on the series of Ln-triflates in combination with computations of Ln(H$_2$O)$_9^{3+}$ and Ln(H$_2$O)$_8^{3+}$ [92]. DFT calculations on the nona- and octa-coordinated Ln-aqua ions yielded slightly distorted D_3 and S_8 symmetries for TTP and SA structures,
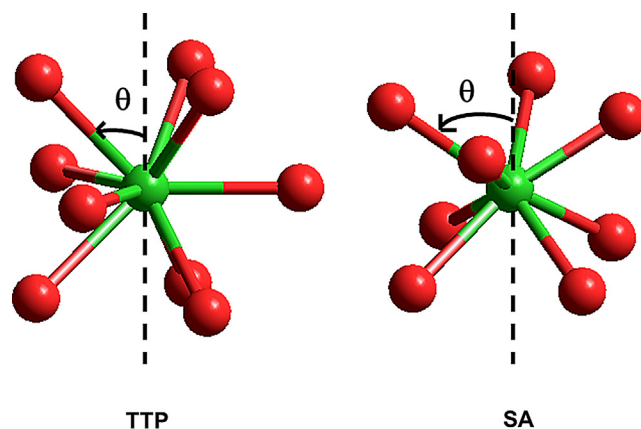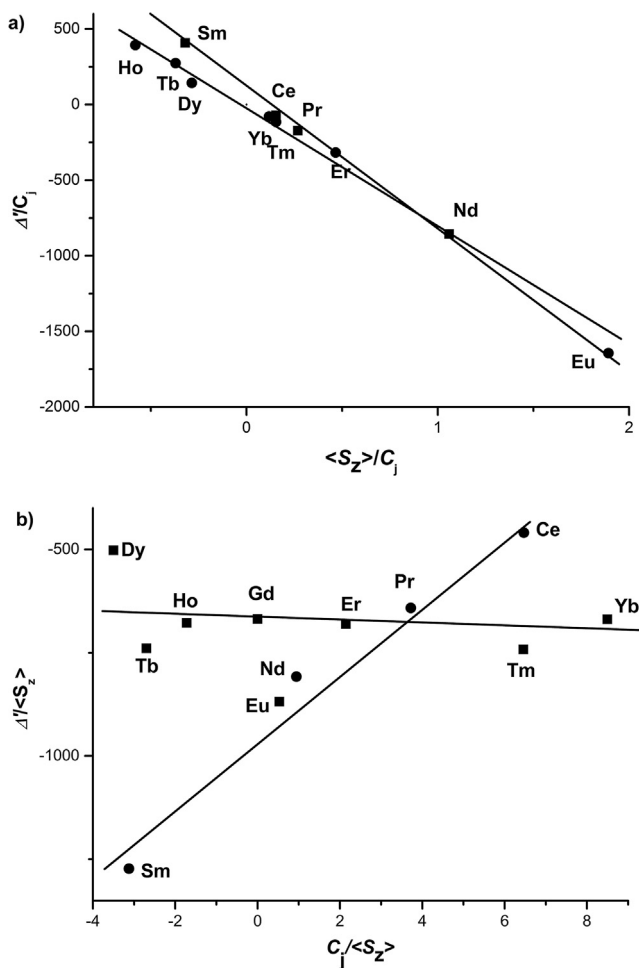

Fig. 5. The coordination polyhedra of lanthanide aqua-ions Ln(H$_2$O)$_n^{3+}$ (n = 8 and 9) with the dotted line indicating the main symmetry axis. Reproduced from Ref. [92] with permission from The Royal Society of Chemistry.

Fig. 6. Plots of paramagnetic ^{17}O NMR shifts of water in the series of Ln^{3+}-aquo ions with trifluoromethanesulfonates coordinated in the second sphere, according to Eq. (10) (a) and Eq. (11) (b). Reproduced from Ref. [92] with permission from The Royal Society of Chemistry.

Table 2
Activation parameters and water exchange rate constants on $[Ln(H_2O)_8]^{3+}$ [125].

	Gd^{3+}	Tb^{3+}	Dy^{3+}	Ho^{3+}	Er^{3+}	Tm^{3+}	Yb^{3+}
$k_{ex}^{298}(10^7\ s^{-1})$	83.0	55.8	43.4	21.4	13.3	9.1	4.7
$\Delta V^{\ddagger}$ (cm^3 mol^{-1})	−3.3	−5.7	−3.3	−6.0	−6.6	−6.9	−6.0
$\Delta S^{\ddagger}$ (J K^{-1} mol^{-1})	−24.1	−36.9	−24.0	−30.5	−27.8	−16.4	−21.0
$\Delta H^{\ddagger}$ (kJ^{-1}mol^{-1})	14.9	12.1	16.6	16.4	18.4	22.7	12.3

for $[Ln(H_2O)_9]^{3+}$ and $[Ln(H_2O)_8]^{3+}$, respectively [126]. Increased enthalpies ($\Delta H^{\ddagger}$), as well as negative values for both entropy ($\Delta S^{\ddagger}$) and activation volumes ($\Delta V^{\ddagger}$) for the heavier lanthanides, confirm the associative mechanism of the octa-coordinated species (Table 2). This conclusion is in agreement with Monte Carlo simulations of water exchange mechanisms for nine- and eight-coordinated lanthanide aquo-ions [127].

The gradual decrease of water exchange rates (k_{ex}) of heavy lanthanides with q = 8 going from Gd^{3+} to La^{3+}, as determined by ^{17}O transverse NMR relaxation rates measurements, can be explained by the interplay between electrostatic and steric effects in the associative mechanism. While an increase of the charge density leads to stronger attraction of water molecules by the lanthanide ions implying faster water exchange, contraction of lanthanide-ions causes steric hindrance for the water molecules entering the first coordination sphere resulting in an overall decrease of the water exchange rates [128].

Direct assessment of water exchange rates for the lanthanides in the beginning of the series is not possible due to the small kinetic effects, except for the two light lanthanides Pr^{3+} and Nd^{3+} due to their favorable ^{17}O NMR chemical shifts that allowed for determination of lower limits of k_{ex} for these Ln^{3+}-ions, being $\geq 40 \cdot 10^7$ and $\geq 50 \cdot 10^7$, respectively [129]. However, since these values match exactly the rate constants determined for the exchange of coordinated SO_4^{2-} by ultrasonic absorption in aqueous solutions of the whole series of lanthanides [130], the water exchange rates for the light lanthanides can be interpolated (Fig. 7).

A somewhat deeper understanding of the relation between the water kinetics and the CN of the lanthanide aquo-ions along with the corresponding stereochemistry has recently been proposed after application of the atom-in-molecule theory [131,132]. Analysis of Ln—O bonds, and particularly bond critical points (BCP), revealed larger electron density values (ρ_{BCP}) for the shorter and

respectively, and allowed for the evaluation of the Ln—O distances (r) and the angles θ between the Ln—O vector and the main symmetry axis of the complex, as well as the geometric factor G_{ax} (see Eqs. (7) and (9)). The calculated G_{ax}-values were related to the slopes obtained from plotting of the ^{17}O shifts according to Eqs. (10) and (11), demonstrating a substantial difference in B_0^2 between the light and heavy lanthanides (Fig. 6). The change in crystal field parameters going from TTP to SA arrangement seems logical considering the considerable differences in the charge distribution around the Ln-ions in these polyhedra [124]. Furthermore, fitting of the ^{17}O NMR data with two datasets: Ce – Sm (q = 9) and Eu – Yb (q = 8), indicated that the crystal field parameter B_0^2 is an order of magnitude larger for the light lanthanides compared to the heavy ones. The values for F were found to be the same for the whole series of lanthanides, which corresponds to a hyperfine coupling constant of $A/\hbar$ = -4.2×10^6 rad s^{-1}, being within the range of the typical value for Ln-coordinated ^{17}O nucleus (-3.9×10^6 rad s^{-1}) [90].

The change of CN halfway of the Ln-series has a significant effect on the water-exchange kinetics of Ln-aquo systems. The exchange rate of coordinated water molecules with the bulk water molecules increases upon a gradual decrease of ionic radius, peaking at Gd^{3+} and decreases thereafter going to Yb^{3+} [125].

From the mechanistic point of view, the water exchange is expected to follow either a dissociative or an associative pathway

Fig. 7. Constants for interchange rate of substitution of SO_4^{2-} on $[Ln(H_2O)_n]^{3+}$ (black squares) and water exchange constants for $[Ln(H_2O)_8]^{3+}$ (red circles). Redrawn from Ref. [125].

hence stronger Ln–O(8) and Ln–O(9P) bonds, and at the same time, small values for Ln–O(9C) bonds that fluctuate for the light lanthanides from La^{3+} to Sm^{3+} (±0.0366 a.u.) and decrease going to Lu^{3+} as the capping bonds get shorter. These findings explain the preference for CN = 9 and 8 for the light and heavy lanthanides, respectively, considering the peculiarity of the capping bonds, which was already observed earlier in the 2D solid-state NMR study of $[Ln(H_2O)_9](CF_3SO_3)_3$ combined with crystallography that demonstrated decreasing occupancies of water molecules in the labile capping positions for Ho, Tm, Yb, and Lu as 2.9, 2.8, 2.7, and 2.4, respectively [133]. Consequently, the exchange mechanism of both SA (q = 8) and TTP (q = 9) structures can be expected to proceed through the formation of bicapped trigonal prism (BTP) intermediates, which facilitates water exchange on capping positions (Fig. 8).

4.2. Lanthanide tris(2,6-dipicolinate) complexes

X-ray crystal structures have shown that all lanthanide tris(2,6-dipicolinate) complexes ($[Ln(DPA)_3]^{3-}$) have similar molecular structures in the solid-state [134–136]. The tridentate DPA ligands are forming a distorted tricapped trigonal prism (TTP) coordination polyhedron around the Ln^{3+}-ion, with six carboxylate O-atoms at the corners of the two trigonal faces of the prism and the three N-atoms at the capping positions (Fig. 9). The binding sites of the ligands are lying on a sphere, which is slightly flattened because

the Ln-N bonds are somewhat longer than the Ln-O bonds. More recently, accurate X-ray studies on a series of $[Ln(DPA)_3]^{3-}$ complexes have been performed [17,137]. The most striking changes passing from Ln = La to Lu that were observed are: (*i*) the average Ln-N distances decrease from 2.64 to 2.43 Å, whereas the Ln-O distances only decrease from 2.53 to 2.36 Å; (*ii*) the top and base O_3-triangles of the prism are twisted with respect to each other over a twist angle that decreases from Ln = La to Lu, where the opposite O-triangles almost eclipse (Fig. 10); (*iii*) the average dihedral angles between the planes of the pyridine rings and LnN_3 are almost invariable across the Ln-series (average 49.9°). A perfect TTP geometry has D_{3h}-symmetry and is achiral, but because of the twist between the top and the base of the prism, the symmetry is lowered to D_3 and consequently, the DPA ligand can wrap around the Ln^{3+}-ion in two enantiomeric ways (Δ and Λ, see Fig. 11). Most published crystal structures are on racemic compounds, but in the presence of interacting chiral compounds, an excess of one of the enantiomers may crystallize [138,139].

The solution structure of $Ln(DPA)_3$ and several derivatives show ^{13}C and ^1H NMR spectra that correspond with D_3-symmetry, which suggests that the solid-state molecular structures are maintained in solution [17,18,140–145]. Luminescence studies also revealed maintenance of the tris-tridentate structure with D_3-symmetry [146]. Furthermore, this is confirmed by EXAFS studies on DMSO solutions of $Ln(DPA)_3$ [17]. The occurrence of a fast intramolecular Δ/Λ-interconversion has been established by variable temperature
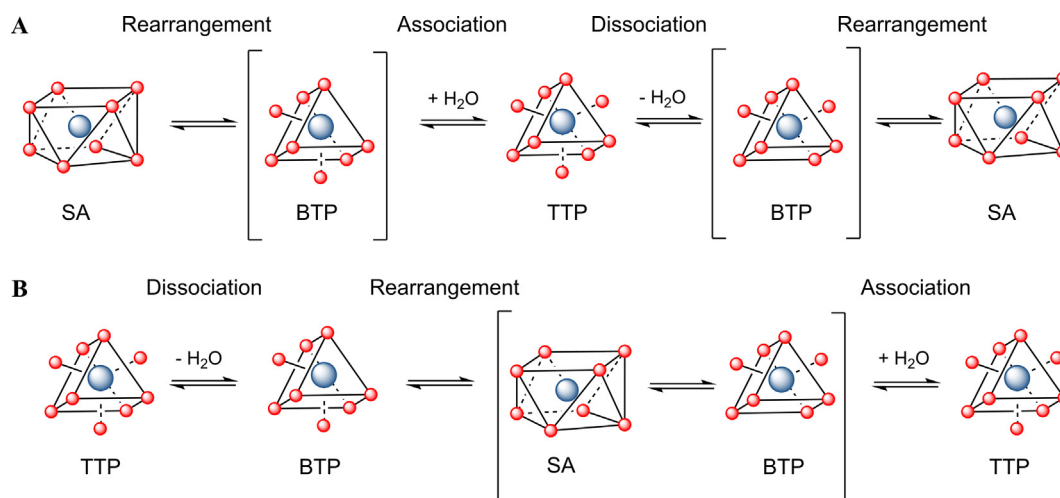

Fig. 8. Extended scheme for associative (A) and dissociative (B) water exchange mechanisms of $[Ln(H_2O)_8]^{3+}$ and $[Ln(H_2O)_9]^{3+}$, respectively.

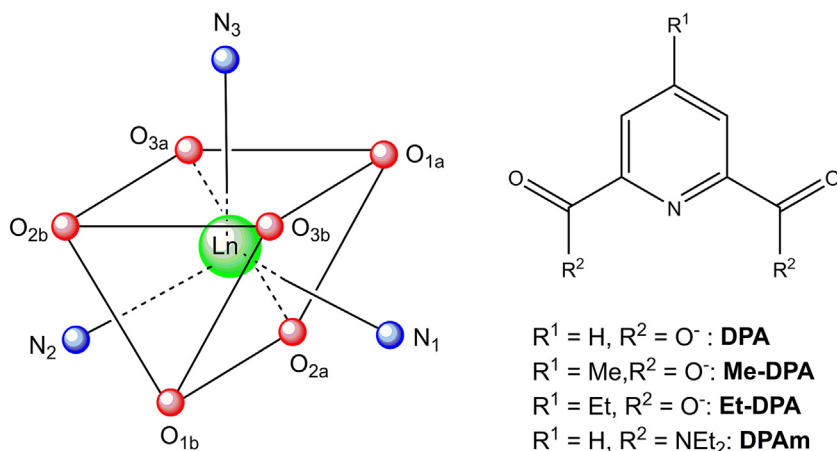**Fig. 9.** Schematic representation of the TTP coordination polyhedron and of the DPA ligand.

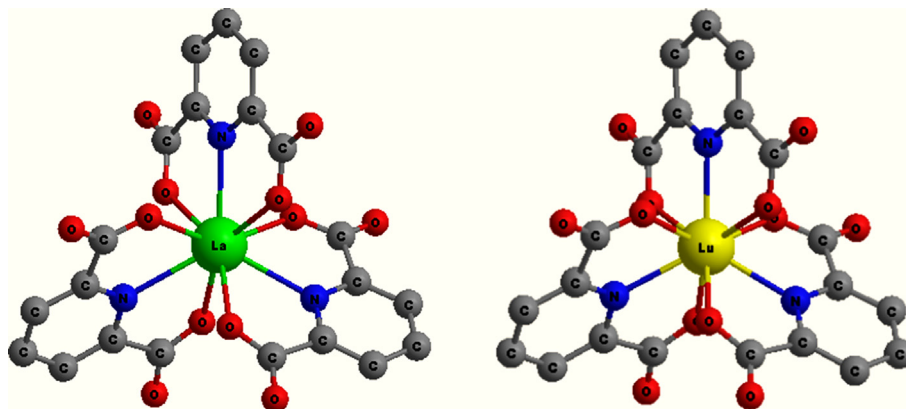**Fig. 10.** Comparison of $[La(DPA)_3]^{3-}$ (left) and $[Lu(DPA)_3]^{3-}$ (right) viewed down their pseudo C_3-axes. H-atoms are omitted [137].

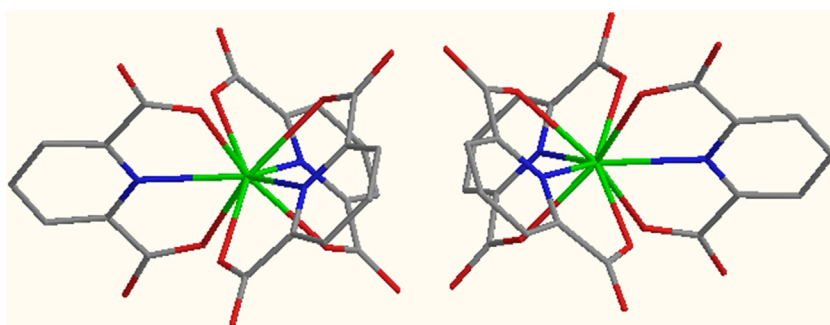**Fig. 11.** Molecular structures of the Δ- and Λ-isomers of $[Ln(DPA)_3]^{3-}$. H-atoms are omitted.

^{1}H NMR measurements on $Ln(Et-DPA)_3$ in D_2O, which showed coalescence of the ABX_3 system for the diastereotopic methylene protons into an A_2X_3 system. The activation energy for this process was almost independent on the size of the Ln^{3+}-ion ($\Delta G^{\neq}(Eu)$ = 63 kJ mol^{-1}, T_c = 290 K; $\Delta G^{\neq}(Tm)$ = 64 kJ mol^{-1}, T_c = 290 K; $\Delta G^{\neq}(Yb)$ = 60 kJ mol^{-1}, T_c = 303 K) [143]. Comparable racemization rates were observed by enantioselective quenching of luminescence in $Eu(DPA)_3$ and $Tb(DPA)_3$ [147]. The absence of water in the first coordination sphere of the Ln-cations has been demonstrated by water ^{1}H relaxation rate enhancement measurements in the presence of $Ln(DPA)_3$ [148], luminescence decay measurements [149], and an MD-simulation of $[Eu(DPA)_3]^{3-}$ suggested that water entered the first coordination sphere only for very short periods of time resulting in an average q-value of 0.17 [150].

Early ^{1}H NMR studies on the paramagnetic $Ln(DPA)_3$ complexes indicated that the contact contributions to the LIS-values of meta- and *para*-DPA protons were virtually absent [141]. These shifts could perfectly be correlated with Bleaney's C_j factors and variable temperature measurements showed the expected T^{-2} dependence (see Eq. (7)). The angles between the Ln-H vectors and the C_3-rotational axis (θ) as calculated from the LIS-values and the axial form of Eq. (7) (B_2^2 = 0), appeared to be consistent with the crystal structures and suggested that no change occurs along the Ln-series [141]. Desreux and Reilley have demonstrated that the ^{13}C LIS-values of both $Ln(DPA)_3$ and $Ln(4-Me-DPA_3)_3$ have contact contributions that cannot be neglected [33,140].

More recently, Ouali et al. revisited the analysis of the $Ln(DPA)_3$ and $Ln(4-Me-DPA)_3$ complexes [143]. The remeasured ^{1}H and ^{13}C NMR spectra of the Ln-series were in good agreement with the previously published data. No break is visible in a plot of their ^{1}H LIS-data according to Eq. (11) (Fig. 12A), suggesting that $B_0^2 G$ (the slope) does not vary much across the Ln-series, whereas a plot according to Eq. (10) suggests a dramatic decrease in F between

the light and the heavy lanthanides (Fig. 12B). By contrast, the ^{13}C data show clear breaks between Eu and Tb in both plot-types (see for example Fig. 12C). Plots according to the crystal field independent 2-nuclei method (Eq. (12)) and the 3-nuclei method (Eq. (13)) have similar breaks into two lines with different slopes and intercepts, which reflects a change of G and thus the geometry across the series. A detailed analysis of the data and a comparison with crystal structures and gas-phase structures obtained by DFT calculations led to the conclusion that a sudden change in F, G, and B_0^2 (for example, $G^{Ce-Eu}/G^{Tb-Yb} \approx 0.60$ and $B_0^{2Ce-Eu}/B_0^{2Tb-Yb} \approx 1.60$ as evaluated for H_{para}) for most ligand nuclei occurs between Eu and Tb [143].

Similar phenomena were observed for other derivatives of $Ln(DPA)_3$ [145]. Recently, a study was reported on $Ln(4-Et-DPA)_3$ in DMSO solution [17]. The LIS values appeared to be somewhat smaller, but the trends were very similar. Various linearization procedures in combination with crystal structure and EXAFS data were applied to analyze the LIS data. The results were similar, although in this case, the value of B_0^2 appeared to be almost invariant across the Ln-series. Again, a significant break in F-values was observed about halfway the series.

If it is assumed that the molecular structures of $Ln(DPA)_3$ in the solid-state are similar to those of $Ln(DPA)_3$ and $Ln(4-Et-DPA)_3$ in solution, it is possible to estimate the G-values for these complexes from the crystal structures. We have fitted the published non-manipulated experimental LIS data of $Ln(DPA)_3$ [143] and $Ln(4-Et-DPA)_3$ [17] with Eqs. (8) and (9) (G_{rh} = 0). A break in F and B_0^2 values was assumed to occur somewhere in the series. The data for the nuclei in each series (before and after the assumed break) were fitted simultaneously, using the values for F for the various ligand nuclei and values for B_0^2 (the same for all Lns and ligand nuclei) before and after the break as adjustable variables. The fittings were performed for various locations of a break. The best
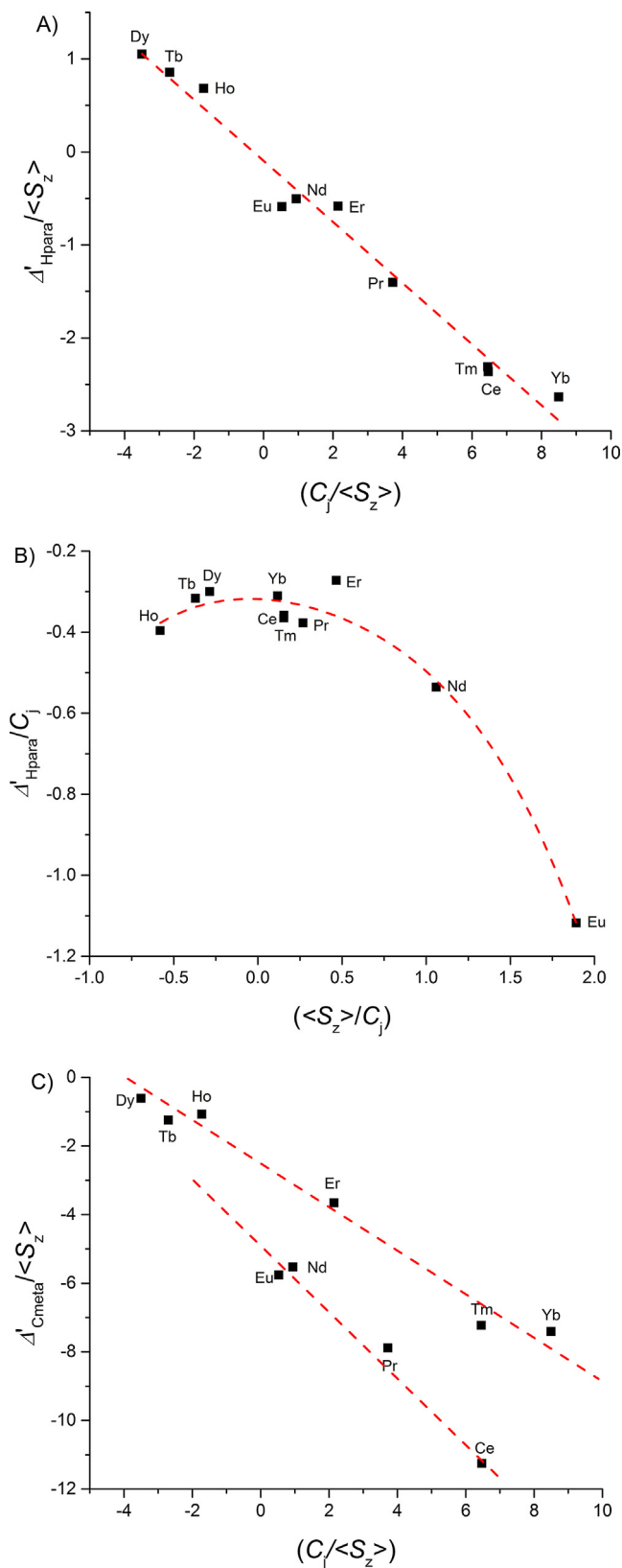
Fig. 12. Plots of LIS data for Ln(DPA)$_3$ from [143]: A) for H$_{para}$ according to Eq. (11); B) for H$_{para}$ according to Eq. (10); C) for H$_{meta}$ according to Eq. (11). The curves are guides to the eye.

fits were obtained by assuming a break between Ho and Er. The values for the best-fit parameters are compiled in Table 3. It is clear anyway that the geometry in solution is similar to that in the solid-

state. The changes in G are related to the decreased twist between the two O$_3$-planes and the decrease of the Ln-nuclei radii between La and Lu.

According to the point charge crystal field theory, the parameter B_0^2 for a TTP coordination polyhedron is proportional to $(2 \cos^2 \theta_O - 1/R^3)$, where R is the distance between the Ln-cation and the ligand donor atoms [24]. Hence, B_0^2 changes sign from positive to negative at $\theta_O = 45°$ and around this value, the value of B_0^2 is highly sensitive toward changes in θ_O. The O-atoms in the crystal structures are disposed at around $\theta_O = 47°$; an increase of θ_O from 46° to 47° would already lead to an increase of B_0^2 with a factor of about 2. Therefore, the increase in B_0^2 observed in solution may be explained by a decrease in R and possibly also a small increase in θ_O upon passing from La to Lu. The decrease in B_0^2 upon changing of solvent from water to DMSO can be attributed to an increase in θ_O. Recently, a similar solvent effect has been observed for Ln-complexes of 1,4,7-tris tris[(6-carboxypyridin-2-yl)methyl]-1, 4,7-triazacyclononane, which also adopt a TTP coordination geometry [152]. These solvent effects are attributed to hydrogen bonds involving the ligand carboxylate O-atoms and to the orientation of solvent dipoles that perturb the dipolar interactions between the Ln^{3+}-ions and the ligand donor atoms [153].

It should be noted that in the TTP geometry the carboxylate C-atoms have a θ near 54.7°, where the term $3 \cos^2 \theta - 1$ and thus G changes sign. Therefore, the LIS values for the carboxylate C-atoms are also sensitive toward tiny variations in the geometry of the complexes along the Ln-series as is reflected in relatively large differences in calculated and observed LIS values for this nucleus.

The breaks observed in G and B_0^2 are also explainable by a gradual change of G and B_0^2, which have an effect that is magnified by the large difference in the magnitudes of C_j and $< S_z >$. We obtained equally good fits with a model where B_0^2 was assumed to vary gradually and proportionally to R^{-3} across the Ln-series.

DFT calculations have demonstrated that the 4f electron density is very sensitive to the coordination sphere: the metal-ligand interaction polarizes the 4f density, leading to maxima located in trans position with respect to the metal-ligand bonds [154]. Nine such maxima were found for Lu(DPA)$_3$, whereas they were absent in La(DPA)$_3$. A similar difference in unpaired electron distribution may explain the increase in F-values going from Ce to Yb. A recent study based on the CASSCF(13,7) wave function of Yb(DPA)$_3$ showed that the magnetic anisotropy, and thus the pseudocontact shift, is very sensitive to the twist angle between the two O$_3$-planes [155].

4.3. Lanthanide tris(oxydiacetate) complexes

The structures of the lanthanide tris(oxydiacetate) complexes ([Ln(ODA)$_3$]$^{3-}$) resemble those of the Ln(DPA)$_3$ complexes (Fig. 13). X-ray crystal structure investigations have shown that the ODA ligand is bound to the Ln-cation in a tridentate fashion forming an Ln-coordination polyhedron that again can be described as a distorted TTP [156–162]. The capping positions are occupied by the three ether O-atoms, whereas six carboxylate O-atoms are located at the corners of the prism. The Ln-O$_{ether}$ distances are somewhat longer than the Ln-O$_{carboxylate}$ distances. The triangular faces are twisted with respect to each other to an extent that decreases along the Ln-series; the twist angle is 18.8° in Nd (ODA)$_3$ and 13.3° in Yb(ODA)$_3$ [157]. The C- and O-atoms of each ODA ligand are almost perfectly coplanar. The symmetry is again D_3 and consequently, there are two enantiomers, Δ and Λ.
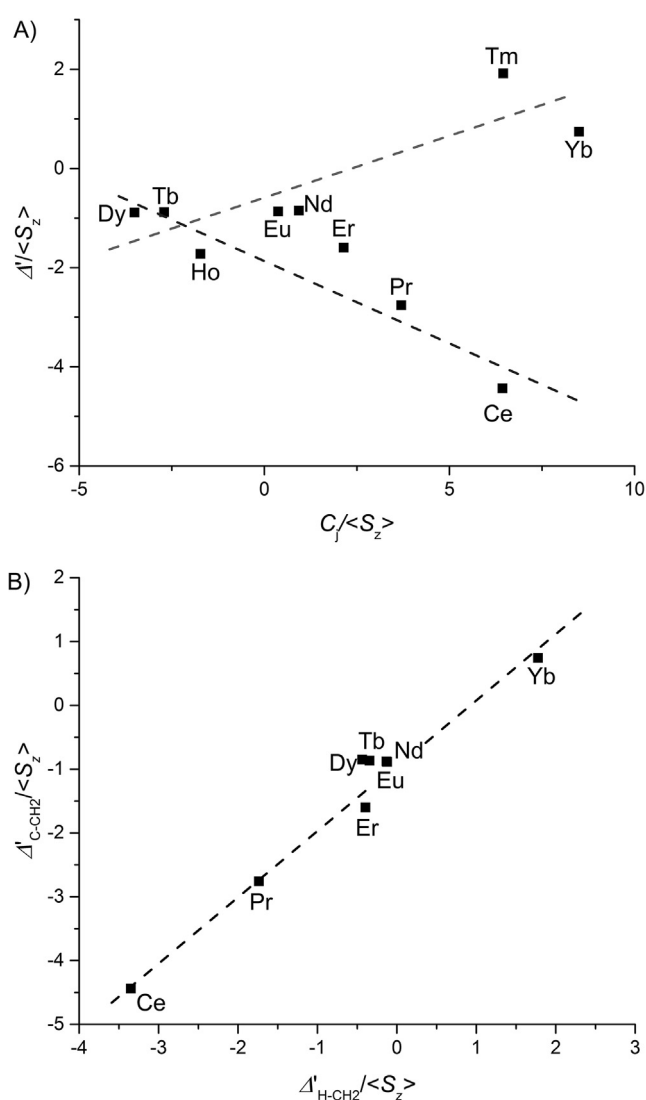
Potentiometric studies have shown that Ln(ODA)$_3$ complexes are also formed in aqueous solution (log β_3 = 10.25–13.36 at 293 K) but the stabilities are much lower than for Ln(DPA)$_3$ (log β_3 = 18.80–22.13 at 293 K) [163,164]. An aqueous solution of Dy (ODA)$_3$ shows negligible Dy^{3+}-induced shifts of the water ^{17}O

Table 3
Best-fit values obtained from fitting of LIS data of Ln(DPA)$_3$, Ln(4-Et-DPA)$_3$, and Ln(ODA)$_3$ using G-values derived from X-ray crystal structure data.

	Ln(DPA)$_3$ [a]		Ln(4-Et-DPA)$_3$ [b]			Ln(ODA)$_3$ [c]	
	Ce → Ho	Er → Yb	Ce → Ho	Er → Yb		Ce → Ho	Er → Yb
F H$_{meta}$	−0.01	0.29	−0.01	0.12	F C$_{COO}$	0.9	0.7
F H$_{para}$	0.00	0.25	−	−	F C$_{CH2}$	−9.1	−5.8
F C$_{COO}$	0.07	−2.74	−0.39	−2.31	F H$_{CH2}$	−5.8	−4.0
F C$_{ortho}$	0.41	1.21	0.07	−0.13			
F C$_{meta}$	−2.93	−1.84	−3.06	−2.44			
F C$_{para}$	1.30	1.44	1.37	1.36			
F C$_{CH2}$	−	−	−0.22	−0.13			
B_0^2	81.7	98.8	51.1	59.4	B_0^2	4.7	−31.3
AF	0.14		0.12		AF	0.26	

Agreement factor, defined as $(\Sigma(\Delta'_{calc}-\Delta'_{exp})^2/\Sigma\Delta'^2_{exp})^{1/2}$.
[a] LIS data measured at 298 K [143].
[b] LIS data measured at 298 K [17].
[c] LIS data measured at 346 K [151].
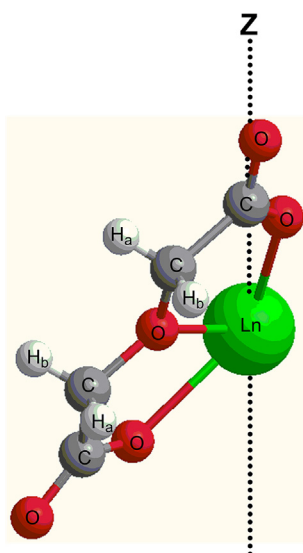
Fig. 13. Schematic representation of the coordination of Ln^{3+} by one of the ODA^{2-} ligands in the [Ln(ODA)$_3$]$^{3-}$ complex together with the 3-fold symmetry axis of this complex.

Fig. 14. Plots of LIS data for Ln(ODA)$_3$ from [151]: A) for C$_{CH2}$ according to Eq. (11); B) for H$_{CH2}$ and C$_{CH2}$ according to Eq. (12). The curves are guides to the eye.

nucleus, which indicates that this complex has no water molecules in the first coordination sphere of Dy^{3+} [90]. The La(ODA)$_3$ complex has a ^{139}La NMR ligand-induced shift of 180 ppm and since each La-bound carboxylate O-atom gives a shift increment of about 30 ppm, whereas bound ether O-atoms have a negligible contribution to the ^{139}La NMR shift, this suggests that 5–6 carboxylate oxygens are La^{3+}-bound [165]. The ratio of Gd^{3+}-induced relaxation rates in the Gd(ODA)$_3$ complex for COO$^-$/CH$_2$ has been measured to be 0.90. Using Eq. (19), the ratio of the distances of Gd and the carboxylate and methylene C-atoms was calculated to be 0.98, which indicates Gd-coordination of the ODA ligand in tridentate fashion [166]. Recently, Fusaro was able to observe the ^{17}O NMR resonances of the carboxylate O-atoms of Ln(ODA)$_3$ (Ln ≠ Ce, Sm, Gd) in aqueous solution [167]. At 9.4 T and 298 K, the spectra displayed two COO ^{17}O resonances in slow exchange on the NMR time scale; one signal with a negligible LIS assigned to O$_{unbound}$ and the other one with a large LIS assigned to O$_{bound}$. A plot according to Eq. (10) shows a perfectly straight line for O$_{bound}$ with a slope $F_{O-bound}$ = -78 ppm, from which with Eq. (3) the hyperfine coupling constant $A/\hbar$ was calculated to be −3.9 rad s^{-1} [167]. The $A/\hbar$-value of a paramagnetic Ln-bound O-atom has been demonstrated to be almost independent of the Ln-ion and the nature of the O-atom under study and to be in the range $(-3.9 \pm 0.6) \times 10^6$ rad s^{-1}

[88,90,91]. It can be concluded that the COO$^-$ groups in [Ln(ODA)$_3$]$^{3-}$ are all bound to the Ln^{3+}-cation in a monodentate fashion, which implies that the solution structures are similar to the crystal structures.
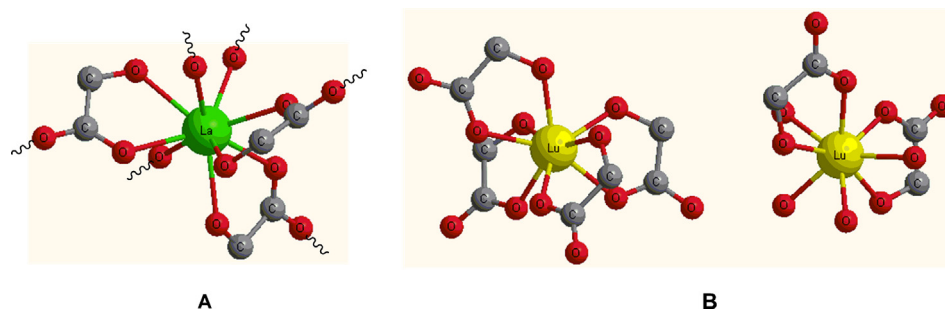
Fig. 15. The single crystal molecular structures of 1:3 Ln-glycolate complexes; H-atoms are not displayed. (A) La(HOCH$_2$COO)$_3$ as representative of the complexes for Ln = La-Gd [173]. Three La-O atoms belong to carboxylates of neighboring complexes and three carboxylate oxygens are bound to neighboring La-cations. (B) The [Lu(HOCH$_2$-COO)$_4$]$^-$[Lu((HOCH$_2$COO)$_2$(H$_2$O)$_4$]$^+$ as representative of the complexes for Ln = Tb-Lu [174].

Previously, ^{13}C and ^{1}H LIS data of this system were measured at 346 K and 4.9 T [151]. Under these conditions, a single resonance was observed for the diastereotopic methylene protons of the ODA ligand in each of the Ln-complexes. Plots of these LIS data according to Eq. (11) showed dramatic breaks between the light and the heavy lanthanides, whereas plots according to (10) were scattered. The slopes in the former plots had opposite signs, indicating a reversal of the sign of $B_0^2 G$ between Ho and Er (see for example Fig. 14A) [151]. However, plots according to the crystal field independent 2-nuclei method (Eq. (12)), gave a single straight line which indicates that the G-value of these complexes is almost invariant along the Ln-series (Fig. 14B) [16]. We have now fitted these data according to a procedure similar to that described above for Ln(DPA)$_3$, using crystal structures of Ln(ODA)$_3$ complexes [156–161] to estimate the G-values, which again gave an optimal fit for a break in B_0^2 between Ho and Er. Only a moderate fit was obtained. Apparently, the solution structures deviate from the solid-state structures more than in the case of Ln(DPA)$_3$. The best-fit parameters are included in Table 3. The best-fit value of B_0^2 for Ce-Ho is considerably lower than that for Ln(DPM)$_3$. Provided that B_0^2 is the dominating crystal field parameter, this suggests that in Ln(ODA)$_3$ the Ln-bound O-atoms for Ce-Ho are at a location for which the angle of the Ln—O vector and the z-axis ($\theta_{O\text{-COO}}$) is closer to 45°. Between Ho and Er, the sign of B_0^2 reverses, suggesting that θ becomes smaller than 45°. This is in contrast with the solid-state, where $\theta_{O\text{-COO}}$ only changes from 46.0° for Nd to 46.2° for Yb [157]. The decrease in $\theta_{O\text{-COO}}$ across the Ln-series in aqueous solution is most likely accompanied by several alterations in the complex geometry, which may explain the relatively poor fit of the LIS values with the use of the x-values estimated from the X-ray molecular structure.

It cannot be excluded that the decrease in B_0^2 along the Ln series takes place gradually. Changes of signs of B_0^2 have also been observed for the Ln-complexes of 1,4,7-tris tris[(6-carboxypyridin-2-yl)methyl]-1,4,7-triazacyclononane. A thorough study of these complexes has demonstrated that these effects are due to the high sensitivity of the electronic structures of the Ln^{3+}-ions to the position of the surrounding ligand donor atoms in the TTP coordination geometry [152].

Upon lowering the temperature, the exchange between the diastereotopic methylene ^{1}H resonances of the Ln(ODA)$_3$ complexes for Ln = Ho-Yb at 4.9 T becomes slow at the NMR time scale [151]. From the coalescence temperatures, the $\Delta G^{\neq}$ for this exchange process was estimated to be about 54 kJ mol^{-1}. For Ln = Ce-Dy, the exchange remained in the fast exchange region, likely because the chemical shift difference of the exchanging enantiotopic protons is smaller for the complexes of these lighter Ln-ions.

4.4. Lanthanide glycolate complexes

Ln^{3+}-ions can coordinate up to 4 glycolate ligands to form complexes with overall stability constants log β_4 = 5.1–6.8 [168]. Grenthe has determined the crystal and molecular structures of single crystals of various Ln-glycolate complexes prepared from microcrystalline Ln(HO-CH$_2$-COO)$_3$·2H$_2$O [169–173]. Glycolate in all complexes is coordinated in a bidentate fashion through a carboxylate O-atom and the hydroxyl O-atom forming an approximately flat chelate ring. The coordination number, as well as the geometry, differed between the first and the second half of the Ln-series. The complexes in the first half have a polymeric structure characterized by units with CN = 9 and a distorted TTP Ln-coordination geometry formed by four glycolate ligands and completed by three O-atoms of carboxylate groups of adjoining units (Fig. 15A) [170]. However, for the smaller Tb-Lu cations the CN decreases to 8 and the complexes are present as binuclear ion pairs, [Ln(HOCH$_2$COO)$_2$(H$_2$O)$_4$]$^+$[Ln(HOCH$_2$COO)$_4$]$^-$ (Fig. 15B). Here, both the cationic and the anionic complex unit have a distorted dodecahedron coordination geometry.

The hydroxyl groups in the above-mentioned complexes, which all were prepared under neutral or acidic conditions, are undissociated. Since coordination to the Ln-ion decreases the pK_a substantially [175], preparations under hydrothermal or basic conditions lead to other complexes with dissociated hydroxylic groups [170,176,177]. The induced pK_a decrease is the largest for Lu^{3+}, which has the smallest radius and hence the largest charge density.

A comparison of experimental relative Gd^{3+}-induced longitudinal ^{13}C NMR relaxation rates (COO 1.0; CH$_2$OH 0.88) of glycolate in aqueous solution with values calculated from the crystal structures using Eq. (19) (COO 1.0; CH$_2$OH 0.85) proves that glycolate in the Gd^{3+}-complex is bound in a bidentate fashion through both O-atoms [178]. This binding mode is confirmed for the Dy^{3+}-complex by the magnitudes of the Dy^{3+}-induced ^{17}O NMR shifts, which are mainly of contact origin [90].

LIS values for all Ln^{3+}-ions (except the radioactive Pm^{3+}) have been measured by the addition of small amounts of LnCl$_3$ to solutions of glycolate that was 5% ^{17}O-enriched at both hydroxylic and carboxylate O-nuclei in D$_2$O at pH 4.6–4.8 at 346 K [179]. The ratio Ln^{3+}/glycolate was ≤ 0.1. The exchange between the various species was fast at the NMR timescale. Perfect straight lines were obtained for plots of the LIS versus the amount of Ln^{3+}. After correction for the diamagnetic contributions, evaluated by interpolation between the corresponding shifts for La^{3+} and Lu^{3+}, followed by extrapolation of the LIS-values to a molar ratio Ln^{3+}/ligand = 1 (ligand = glycolate or D$_2$O) gives $n^*\Delta'_{D2O}$ and $m^*\Delta'_{glycolate}$, where n and m define the stoichiometry of the complex species under study (Ln(glycolate)$_m$(D$_2$O)$_n$). Plotting of the obtained Δ'-values according to Eqs. (10) and (11) afforded almost straight lines with

Table 4
Best-fit values obtained from fitting of LIS data of Ln-glycolate[a] to Eq. (8).

|		COO[b]	OH	D_2O	COO	CH_2	CH_2
Ce → Ho	$x*F$ [c]	−103.7	−159.0	−200.0	2.2	−1.9	−1.0
	$x*G$	−13.6	2.2	12.8	−5.9	−2.3	−1.1
Er → Yb	$x*F$	−77.7	−123.0	−142.7	6.3	1.0	−0.3
	$x*G$	−18.6	−3.4	10.4	−7.2	−2.4	−0.8

[a] Values at 246 K, extrapolated to ρ = 1.
[b] Fast exchange between the two O-resonances.
[c] $x = m,n$ defines the stoichiometry (Ln(glycolate)$_m$(D$_2$O)$_n$).

small breaks, which were originally assigned to gradual tiny structural changes resulting from the decrease of the ionic radii across the Ln-series [179]. However, plots according to the 2-nuclei and 3-nuclei approach (Eqns. 12–16) suggested that these breaks are due to more drastic structural changes [180]. Taking this into account, we have now fitted the LIS data for Ce-Ho and for Er-Yb separately to Eq. (8). The best-fit parameters are collected in Table 4. F-values for Ln-bound O-atom, generally are found in a small range of −70 ± 11 at 246 K, independent of the nature of the O-atom [35,90]. Only one carboxylate ^{17}O signal was observed because the exchange between the Ln-bound and the free O-resonance is fast on the NMR time scale. Assuming that the $m*F$-value of the latter O-atom is negligible, the value of the bound O-atom is 207.4 The $m*F$- and $n*F$-values (see Table 4) suggest that the most likely stoichiometry of the predominant complex for Ln = Ce → Ho is Ln(HOCH$_2$COO)$_3$(D$_2$O)$_3$, in agreement with the relaxation rate data for the Gd^{3+}-complex and the crystal structures for Ln = La-Gd mentioned above. Then, the most likely geometry is a TTP. The relatively low G-value for the OH O-atoms compared to the COO O-atoms points to a preference for an equatorial location (the capping locations), whereas the COO and D$_2$O O-atoms are probably predominantly at the two triangular faces. Fast exchange between the various possible structures within these limitations leads to averaged C_3-symmetry, which is a prerequisite for the above data treatment.

Treatment of the F- and G-values for Er → Yb in a similar way does not afford a reasonable stoichiometry for the concerning complexes. Perhaps these complexes have, like the crystal structures, 8-coordinated Ln-ions and a low symmetry, which makes it impossible to apply the above separation of contact and PCS in this case.
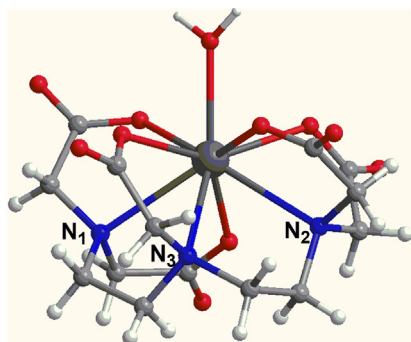
Fig. 16. Crystal structure of [Gd(DTPA)(H$_2$O)] (top) [187] and Newton projection of the ethylene bridges showing the interconversion between the $\lambda\lambda$ and $\delta\delta$ enantiomers.

4.5. Lanthanide complexes of diethylenetriamine-N,N,N',N'',N''-pentaacetate

X-ray crystal structures of various Ln^{3+}-complexes of diethylenetriamine-N,N,N',N'',N''-pentaacetate (DTPA) have been reported. The CN is always 9. The DTPA ligand is bound octadentately through the three N-atoms and an O-atom of each of the five carboxylate groups and the Ln-coordination sphere is completed with a water ligand (Fig. 16) [181–188]. The coordination can be best described as a distorted TTP with water and the two lateral N-atoms (N$_1$ and N$_2$) at the capping positions [182]. The two ethylene groups have either the $\lambda\lambda$- or the $\delta\delta$-conformation. Any symmetry is absent in these structures.

This structure is retained in solution, as has been demonstrated by ^{13}C NMR relaxation rate enhancements measured for the Nd-complex at 4.9 T and 246 K, which were in agreement with the solid-state Nd-C distances [189]. However, the presence of only 8 resonances in the ^{13}C NMR spectra indicates that there is fast exchange between the two enantiomeric forms ($\lambda\lambda$ and $\delta\delta$, see Fig. 16), which produces an effective plane of symmetry through the central glycine unit. The same conclusion was drawn from the presence of 11 signals in the ^1H NMR spectra of Ln-DTPA complexes in aqueous solution for Ln = Pr, Eu, and Yb at 7.0 T and 273–298 K, which coalesced to 9 signals upon increase of the temperature [190,191]. A plot of the ^{17}O NMR shifts for all Ln-ions (except Pm) according to Eq. (10) gave a perfectly straight line with a slope of −53, which indicates that q = 1 for the whole Ln-series [189]. The similarity between solid and liquid state structures was confirmed for [Eu(DTPA)(H$_2$O)]$^{2-}$ by analysis of EXAFS data [192,193].

The Ln-DTPA complexes are almost the same at first sight, but a closer inspection shows subtle differences in geometry that have important consequences for other chemical properties. For example, the Ln—O$_{water}$ bond length for Ln = Yb is almost the same as that of Nd, whereas a smaller length should be expected due to a decrease of the ionic radius (see Table 5). By contrast, the Ln—O$_{carboxylate}$ does show the expected decrease. The O-O distances and the O-Ln-O angles around the Ln-bound water molecule indicate that the cavity available for the water molecule narrows due to the lanthanide contraction, which results in a stretching of the Ln—O$_{water}$ bond to reduce the strain. Aqueous solutions of the related [Ln(DTPA-BMA)(H$_2$O)] complexes (DTPA-BMA = 1,7-bis [(N-methylcarbamoyl)methyl]-1,4,7-triazaheptane-1,4,7-triacetate) show a dramatic increase of the exchange rate of water between the complex and the bulk for Gd and Ho. A reversal of the sign of the activation volume for this reaction indicates a transition of water exchange mechanism from interchange activation for Ln = Nd to limiting dissociative for the other heavier Ln-ions (Fig. 17) [194]. A lengthening of the Ln—O$_{water}$ bond as a result of strain has also been shown for Ln-complexes of the monophosphonate analog of DOTA (DOTA = 1,4,7,10-tetraazacyclododecane-1,4,7,10-tetraacetate) [195]. In that case, increasing strain along the Ln-series ultimately leads to the expulsion of the Ln-bound water. Similar phenomena have recently been reported for Ln-DOTMA chelates (DOTMA = 1R,4R,7R,10R-α,α', α'', α'''- tetramethyl-1,4,7,10-tetraazacyclododecane-1,4,7,10-tetraacetate) [196].

Table 5
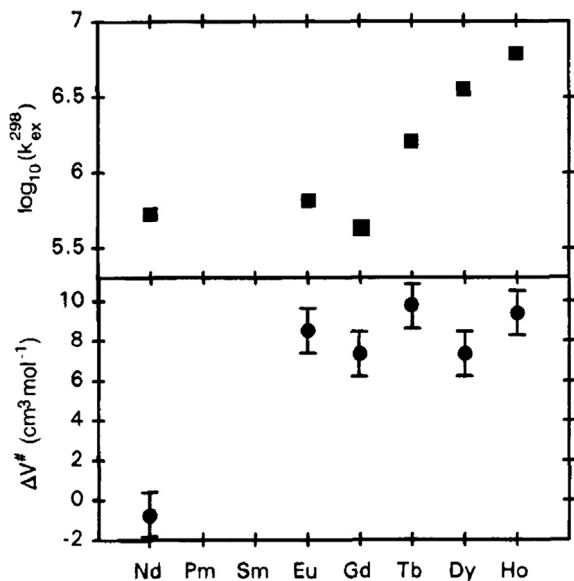Comparison of some solid state geometric data between [Nd(DTPA)(H$_2$O)]$^{2-}$ [184] and [Yb(DTPA)(H$_2$O)]$^{2-}$ [183].

|	[Nd(DTPA)(H$_2$O)]$^{2-}$	[Yb(DTPA)(H$_2$O)]$^{2-}$
Ln-O$_{water}$ (Å)	2.45	2.42
Ln-O$_{carboxylate}$ (Å)[a]	2.44	2.30
O$_{water}$-O$_{carboxylate}$ (Å)[a]	2.98	2.81
∠O$_{water}$-Ln-O$_{carboxylate}$ (°)[a]	75.1	72.9

[a] Averaged over the 4 nearest neighboring O-atoms.

Fig. 17. Water exchange rates k_{ex}^{298} and activation volumes $\Delta V^{\neq}$ of water exchange on the DTPA-BMA complexes of the Nd, Eu, Gd, Tb, Dy, and Ho cations. Reprinted with permission from Ref. [194], Copyright (1998) American Chemical Society.

4.6. Lanthanide complexes of ethylene glycol-bis(2-aminoethylether)-N,N,N′,N′-tetraacetate

In all crystal structures of Ln^{3+}-complexes of ethylene glycol-(2-aminoethylether)-N,N,N′,N′-tetraacetate (EGTA), the EGTA ligand is bound octadentately through the two ethylene glycol O-atoms, an O-atom of each of the four carboxylate groups and the two N-atoms. The EGTA ligand is sterically very demanding, which is reflected in the CN, which changes twice along the series as a result of the increase in steric strain due to the lanthanide contraction. The La^{3+} and Ce^{3+}-complexes have CN = 10, q = 1, and are bridged by coordination of a COO-group of an adjacent complex [197]. The Ln-EGTA complexes for Ln = Eu-Er have CN = 9 and q = 1 [187,193,197–204], whereas for the Yb^{3+} and Lu^{3+}-complexes, the CN is further decreased to 8 and q = 0 [198,203]. For the Nd-EGTA complex, both 9- and 10-coordinated solid-state structures have been reported [197,198].
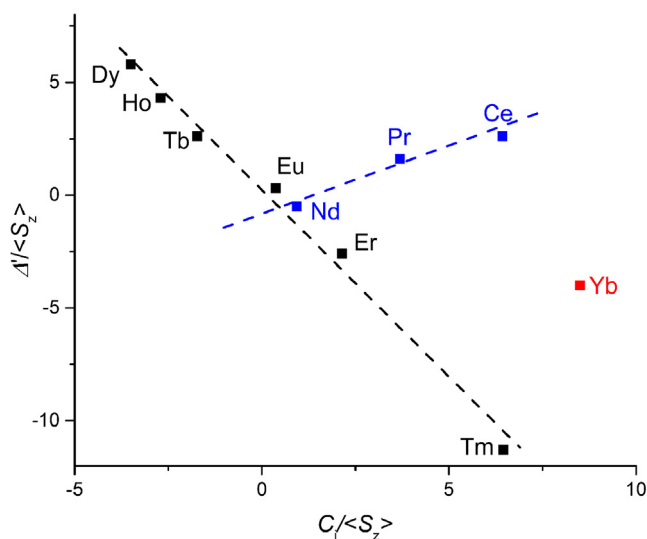

Fig. 18. Plot of the ^1H LIS values for one of the acetate protons of Ln-EGTA complexes at 298 K according to Eq. (11). Data from [205].

A plot of LIS values for the acetate protons according to Eq. (11) for aqueous solutions of Ln-EGTA complexes shows two breaks, one between Nd and Eu and another one between Tm and Yb (Fig. 18) [205]. This suggests that in solution similar changes in CN occur as in the solid-state. For Ln = La-Ce, the solution structure can be thought to be formed from the solid-state structure by substitution of the bridging carboxylate group by a water molecule to give a q = 2 complex. Most likely q = 1, for Ln = Eu-Tm and q = 0 for Ln = Yb and Lu. This is supported by variable temperature UV–vis measurements for the Ce-complex showing the presence of two species that were assigned to the 9- and 10-coordinated complexes. The value of q = 1 for Ln = Eu-Tm is in line with the hydration number for Eu-EGTA as determined by luminescence decay [206] and the presence of a single absorption for the $^5D_0 \leftarrow {}^7F_0$ transition in the UV–vis spectrum. For Gd-EGTA, the relaxivity of the Gd-complex [207], the value of the ^{17}O hyperfine coupling constant (-3.2×10^6 rad s^{-1}) [205], and the similarity of the UV-spectrum in the solid and liquid state indicated that q = 1 [187].

The proposed structural changes of Ln-EGTA-complexes in solution were supported by variable temperature ^1H and ^{13}C NMR spectra, which showed different dynamics for the three groups of lanthanides along the series. The fluxional processes for Ln = La-Tm lead to wagging between the two possible staggered conformations of each of the ethylene bridges (δ and λ) and to effective C_2-symmetry for the 10- and 9-coordinated complexes, whereas the NMR spectra for 8-coordinated Yb-complexes did not show any exchange broadening (Fig. 19) [187].

Information on the dynamics at a ps scale has been obtained by MD-simulations, which demonstrated for example that due to the large strain, the Gd-O$_{water}$-distance in [Gd(EGTA)(H$_2$O)]$^-$ is 3% longer than in [Gd(DTPA)(H$_2$O)]$^{2-}$ and [Gd(DOTA)]$^-$ [204,208]. This is consistent with its relatively large water exchange rate (k_{ex}^{298} = 3. 1×10^7 s) by means of a dissociative reaction mechanism. Moreover, these studies revealed that after dissociation of the water molecule, the 8-coordinate transition state of the exchange reaction has two locations where a new water molecule can enter, which may be an additional explanation for the relatively high water exchange rate.
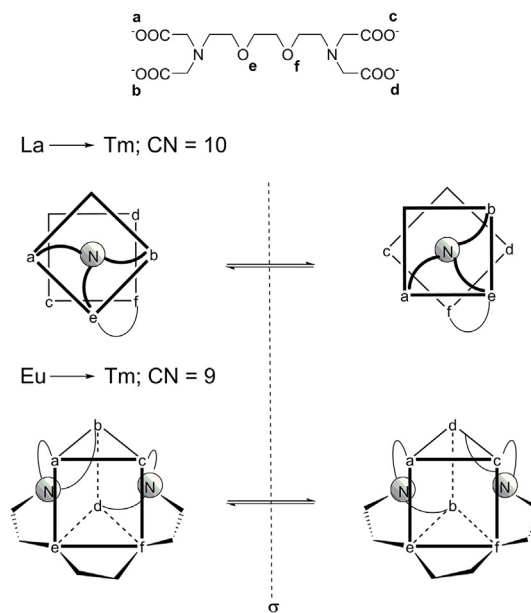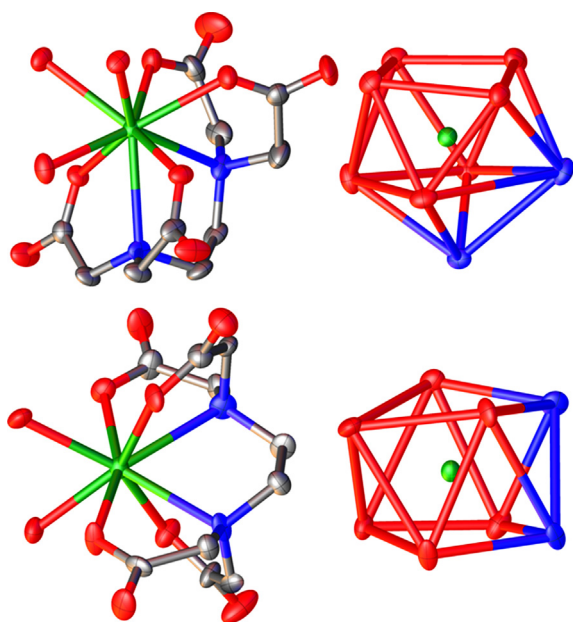

Fig. 19. Schematic representation of fluxional processes in Ln-EGTA complexes leading to effective C_2-symmetry. The complexes with CN = 8 (Yb, Lu) show no chemical exchange [205].

4.7. Lanthanide complexes of ethylenediamine-N,N,N′,N′-tetraacetate

A rather large number of X-ray structures of [Ln(EDTA)]⁻ complexes has been reported in the literature. All these structures evidence hexadentate coordination of the ligand to the Ln³⁺-ion, the remaining coordination positions being often occupied either by water molecules or other polydentate ligands [209–211]. In some cases the coordination environment is completed by the coordination of O-atoms of the carboxylate groups of neighboring [Ln(EDTA)]⁻ entities, resulting in the formation of coordination polymers in the solid-state [212], including an example of a 10-coordinate La³⁺-complex [213]. However, these polymeric structures are very unlikely to be present in solution.

The series of [Ln(EDTA)]⁻ salts that were more extensively characterized in the solid-state are the M[Ln(EDTA)(H₂O)ₑ]·xH₂O salts (M = Na, K or Cs). The Na⁺ salts are isomorphous throughout the series from La to Er and crystallize in the orthorhombic *Fdd2* space group [188,209,214–216]. These salts contain the 9-coordinate [Ln(EDTA)(H₂O)₃]⁻ complexes (Ln = La-Er), in which the coordination polyhedron can be best described as a capped square antiprism (Fig. 20). The O-atoms of two acetate groups and the O-atoms of two coordinated water molecules define one of the square faces of the polyhedron, while the second one is delineated by an amine N-atom, two O-atoms of acetate groups and the O-atom of a coordinated water molecule. The second amine N-atom is capping the latter square face. The Cs⁺ salts of the large lanthanide ions contain nine-coordinate metal ions (Ln = Pr, Nd, Sm), while the smaller lanthanides form eight-coordinate [Ln(EDTA)(H₂O)₂]⁻ complexes (Ln = Dy, Ho, Yb) [209,217]. Similar 8-coordinate species are observed in the guanidinium salts of the Yb³⁺ and Lu³⁺-complexes [187,218]. The metal ions in the 8-coordinated complexes present a distorted square antiprismatic coordination environment, where each of the square faces is described by two oxygen atoms of acetate groups, an amine nitrogen atom and a coordinated water molecule (Fig. 20).

The conformation of the ligand in the [Ln(EDTA)(H₂O)₃]⁻ complexes can be described as $\delta_E(\delta\lambda\delta\lambda)/\lambda_E(\lambda\delta\lambda\delta)$, where subscript E identifies the conformation of the five-membered chelate ring resulting from the coordination of the ethylenediamine moiety,
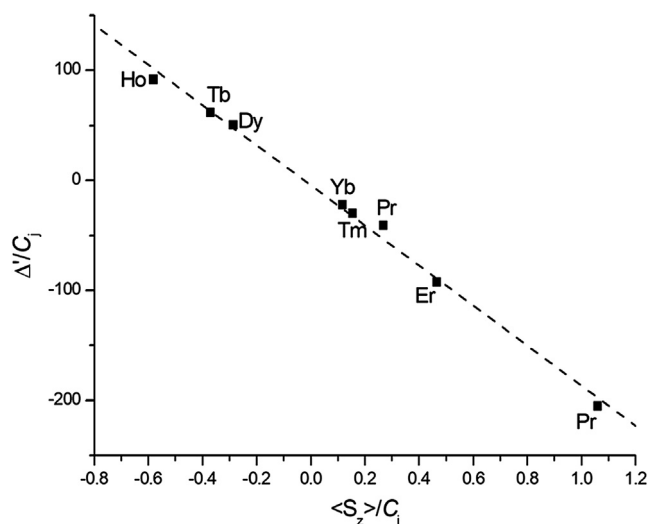
and $(\delta\lambda\delta\lambda)$ [or $(\lambda\delta\lambda\delta)$] describes the conformations of the four chelate rings generated upon coordination of the glycinate groups [219]. The Cs[Ln(EDTA)(H₂O)₂]·xH₂O salts crystallize as racemates, with the two $\delta_E(\lambda\lambda\lambda\lambda)/\lambda_E(\delta\delta\delta\delta)$ enantiomers being centrosymmetrically related in the crystal lattice. The same conformation is observed in the guanidinium salts of the Lu³⁺ and Yb³⁺-complexes. Thus, the X-ray structures of [Ln(EDTA)(H₂O)ₑ]⁻ complexes evidence that a structural change occurs across the lanthanide series, which involves not only variations in the number of coordinated water molecules but also a change in the conformation adopted by the ligand.

Early ¹⁷O NMR measurements in solutions of the [Ln(EDTA)(H₂O)ₑ]⁻ complexes evidenced a linear trend of the paramagnetic shifts according to Eq. (10), with the exception of Eu³⁺ [220]. In the latter case, the ¹⁷O NMR shift was obtained from a diluted solution, and it is likely endowed with a larger error. This result suggests that there is no abrupt change in the number of water molecules coordinated to the metal ion along the series from Pr to Yb. The slope of the straight line obtained with the ¹⁷O NMR shifts extrapolated to a molar ratio Ln³⁺/water ρ_w = 1 is qF 182 ± 5 (see Fig. 21). Each coordinated water molecule is expected to contribute with an F value of 80 assuming a hyperfine coupling constant $A/\hbar$ = −3.9 × 10⁶ rad s⁻¹ (A^{iso} = 0.62 MHz). Indeed, different ¹⁷O NMR studies and also DFT calculations (using either the small-core ECP or DKH approaches) indicated that $A/\hbar$ values of coordinated water molecules do not differ significantly in Gd³⁺-complexes with polyaminopolycarboxylate ligands [221]. Thus, the number of water molecules estimated from these ¹⁷O NMR data is 2.4, which suggests that an equilibrium exists in solution involving the q = 2 and q = 3 species. The equilibrium constant likely varies gradually across the lanthanide series, so that there is no abrupt change in the plot according to Eq. (10). Linear plots according to Eq. (10) were also obtained for EDTA-bisamide complexes, in spite of the presence of a hydration equilibrium evidenced by the analysis of the ⁵D₀ ← ⁷F₀ transition in the absorption spectra of the Eu³⁺ derivative [222].

Recent spectroscopic studies performed for the Gd³⁺ and Er³⁺-complexes of EDTA allowed determining the equilibrium constant involving the bis-hydrated 8-coordinate and tris-hydrated 9-coordinate species according to Eq. (37) [187,223].

$$[Ln(EDTA)(H_2O)_3]^- \leftrightarrow [Ln(EDTA)(H_2O)_2]^- + H_2O \qquad (37)$$

Fig. 20. Views of the structures of the [Dy(EDTA)(H₂O)₃]⁻ (top, Ref. [209]) and [Dy(EDTA)(H₂O)₂]⁻ (bottom, Ref. [188]) complexes and the corresponding coordination polyhedra. Color code: red: oxygen; blue: nitrogen; green: dysprosium.

Fig. 21. Plot of LIS data from [220] for [Ln(EDTA)(H₂O)ₑ]⁻ complexes according to Eq. (10).

Table 6
Thermodynamic parameters reported for Eq. (37).

Ln^{3+}	Eu^a	Gd^b	Er^c
K^{298}	0.59	1.6	19
% q = 2 at 298 K	37	62	95
ΔG^{298}/kJ mol^{-1}	+1.3	−1.6	−7.3
ΔH/kJ mol^{-1}	+17.7	+18.2	
ΔS/J mol^{-1} K^{-1}	+54.9	+66	
ΔV/cm^3 mol^{-1}	+13.2		

^a Rom Ref. [224].
^b From Ref. [187].
^c From Ref. [223].

a Rom Ref. [224].
b From Ref. [187].
c From Ref. [223].

The thermodynamic data for the hydration equilibrium are also available for the Eu^{3+}-complex from the analysis of the $^5D_0 \leftarrow {}^7F_0$ absorption band [224]. The results of these studies are summarized in Table 6. The equilibrium constants determined for the Eu^{3+} and Gd^{3+}-complexes evidence significant populations of both the bis- and tris-hydrated species in solution. The data reported for the Eu^{3+} complex assumed that the oscillator strengths of two bands of the $^5D_0 \leftarrow {}^7F_0$ transition are identical, and thus are probably endowed with larger errors. The equilibrium constant appears to vary progressively across the series, as for the Er^{3+}-complex there is still a significant population of q = 3 species at 298 K (5%). For the La^{3+}-complex, the abundance of the q = 3 species at 298 K was estimated to be ~10% by assuming that ΔG^{298} varies linearly with the number of $4f$-electrons with a slope of −1.1 kJ mol^{-1} [187]. The hydration equilibrium shown in Eq. (37) is characterized by a positive reaction entropy and a positive reaction volume, as would be expected.

4.8. Lanthanide complexes of DOTA and derivatives

X-ray crystal structural studies and ^1H NMR solution studies of the macrocyclic Ln(DOTA)$^-$ complexes (DOTA = 1,4,7,10-tetraazacyclododecane-N,N′,N″,N‴-tetraacetic acid, Fig. 22) have shown that they can occur in a variety of structures where the DOTA ligand is bound octadentately to the Ln^{3+}-ion through the four N-atoms and an O-atom of each of the four carboxylate groups. The binding of the Ln^{3+}-ion by the N-atoms fixes the four ethylene groups of the macrocycle in two enantiomeric conformations having all of these groups either in a δ- or a λ-gauche orientation ($\delta\delta\delta\delta$ and $\lambda\lambda\lambda\lambda$). The four acetate arms can be arranged with opposite helicities, Λ and Δ. The combination of all the metal-binding units in one ligand defines an Ln^{3+}-coordination polyhedron formed by two parallel faces defined by the four-ring nitrogen (N$_4$ plane) and four acetate arm oxygen (O$_4$ plane) donor atoms of the ligand with a twist angle (ω) and a distance (d) between those planes. The O-Ln-O angle between two transannular oxygen atoms in the O$_4$ plane is known as the opening angle (ψ) (see Fig. 24). The two outlined stereochemical elements combine to form two diastereoisomeric pairs of enantiomers, $\Lambda(\delta\delta\delta\delta)/\Delta(\lambda\lambda\lambda\lambda)$ and $\Delta(\delta\delta\delta\delta)/\Lambda(\lambda\lambda\lambda\lambda)$, with the ring and the
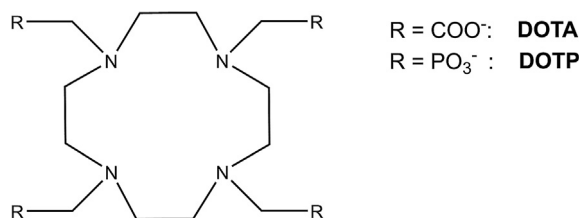

Fig. 22. Chemical structures of the tetraaza macrocyclic ligands cited in this section.

R = COO$^-$: **DOTA**
R = PO$_3^-$: **DOTP**

arms having opposite helicities, leading to a square antiprismatic (SA or M) coordination geometry (positive ω), and $\Delta(\delta\delta\delta\delta)/\Lambda(\lambda\lambda\lambda\lambda)$, with the same ring and acetate helicity, giving a twisted square antiprismatic (TSA or m) structure (negative ω) (Figs. 23 and 24). The coordination polyhedron may be extended to have a water O-atom capping the O$_4$-plane. Without such a water molecule, the respective complex geometries are called SA′ (or M′) and TSA′ (or m′).

Crystal structures of many Ln-DOTA-complexes have been reported. The structures of most of the complexes for Ln = Pr → Lu (Ln = Pr [226], Nd [226], Eu [226,227], Gd [225,228], Dy [226], Ho [226], Lu [229]), and of Y-DOTA [225,230] are very similar. They have a 9-coordinate structure with a water molecule in the first coordination sphere of the Ln^{3+}-ion and SA geometry ($\omega \sim 39°$). However, the structures obtained for the complexes with the larger Ln^{3+}-ions (La and Ce) are different. The La^{3+}-complex has a polymeric structure with a TSA geometry ($\omega = -22°$), with no La^{3+}-bound water but instead a bridging carboxylate O-atom of a neighboring complex molecule [231]. In solution, the La-DOTA-complex is, like all other Ln-DOTA-complexes, monomeric (see below). Possibly the formation of crystals of the polymeric structure is solubility driven. The Ce^{3+} complex has a TSA coordination ($\omega = -25°$) and a $\Lambda(\lambda\lambda\lambda\lambda)$ absolute configuration [226]. The Tm-complex (TSA′, $\omega \sim -24.5°$) is 8-coordinate and has no apically bound water molecule [226]. The Sc-complex is also 8-coordinate, with an SA′ configuration ($\omega \sim 41°$) for the isolated [Sc(DOTA)]$^-$ anion in the Na[Sc(DOTA)] crystal [226], but a TSA′ configuration ($\omega \sim -28°$) was found for crystals of K[Sc(DOTA)]$^-$[H$_6$DOTA]Cl$_2$·4H$_2$O, probably enforced by the solid-state packing [232]. In the lanthanide series, the sudden change of ω between Ce and Pr accompanying the transition from the TSA to the SA conformation can be ascribed to structural effects due to the Ln^{3+}-contraction. Several other geometric parameters show a regular and gradual decrease along the lanthanide series. The Ln—O$_{water}$ bond distance decreases from 2.59 Å (Ce) to 2.416 Å (Lu), and the Ln-N$_{av}$ and Ln—O$_{av}$ bond distances, respectively, from 2.80 Å and 2.50 Å for La to 2.53 Å and 2.27 Å for Tm [226,231]. The TSA/SA ratio depends on the extent to which the size of the Ln ion matches the size and shape of the cavity that can be formed by the DOTA ligand in either the TSA or SA conformation. The geometry and size of this cavity are primarily dictated by the orientation of the ligand pendant arms. The TSA configuration allows a larger distance d between the N$_4$ and O$_4$ planes than the SA configuration (Fig. 24). The early, larger, Ln^{3+}-ions, such as La^{3+} and Ce^{3+}, require a larger cavity, with an N$_4$-O$_4$ distance $d \geq 2.5$ Å and accordingly, prefer the formation of the TSA isomer in their complexes. The decrease of the Ln^{3+} ionic radius along the series reduces its distance to the N$_4$ plane and the consequent movement of the O$_4$ plane towards the N$_4$ plane, leading to a switch to the SA structure with an N$_4$-O$_4$ distance $d \approx 2.3$–2.4 Å. As mentioned above, this conformational transition takes place, in the solid state, between the Pr^{3+} and Ce^{3+}-complexes of DOTA [233].

The average opening angle ψ_{av} determines whether or not an apical water molecule is coordinated. When $\psi_{av} > 135°$, sufficient space is available to coordinate water. For example, TSA (e.g. [Ce(DOTA)(H$_2$O)]$^-$ in the TSA configuration has ψ = 144° and [Pr(DOTA)(H$_2$O)]$^-$ in the SA cifiguration ψ = 148°. But upon decrease of ψ_{av} near the heavy end of the Ln-series, the water molecule is expelled from the first coordination sphere, leading to the TSA′ [(Tm(DOTA)]$^-$, ψ = 124°) or SA′ ([Sc(DOTA)]$^-$, ψ = 124°) conformations [226,234].

Potentiometric studies have shown that the Ln(DOTA)$^-$ complexes in aqueous solution have very high thermodynamic stability constants (K_{LnL}), which change along the Ln series [235,236]. The reported values of log K_{LnL} vary due to differences in the employed experimental methods and ionic strength. According to the most recent publication, the stability constants increase along the Ln
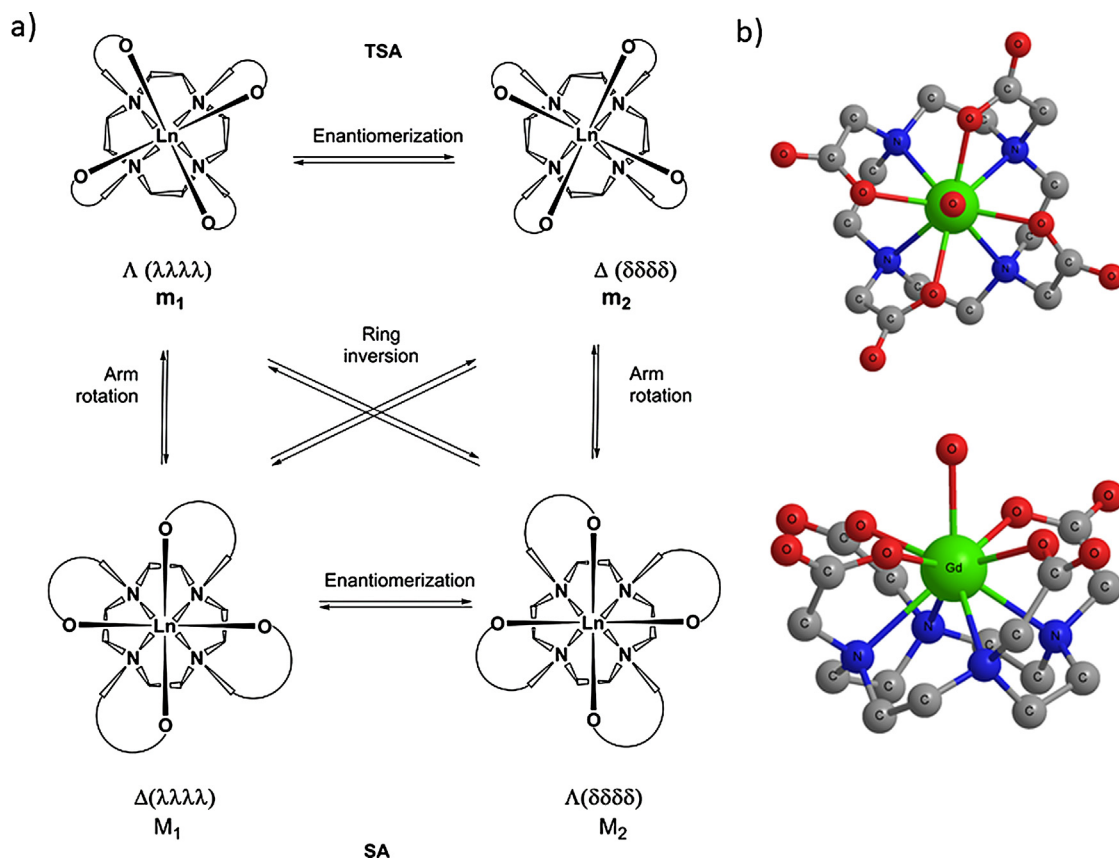
Fig. 23. (a) Schematic representation of the structures and dynamics of Ln(DOTA)$^-$ complexes. These structures have an apical water molecule, which is omitted for clarity. Similar structures without water ($q = 0$) are denoted as TSA′ and SA′. (b) Crystal structure of Gd(DOTA)(H$_2$O) viewed down the Gd-O$_{water}$ bond (top) and perpendicular to it (bottom). H-atoms are omitted for clarity [225].
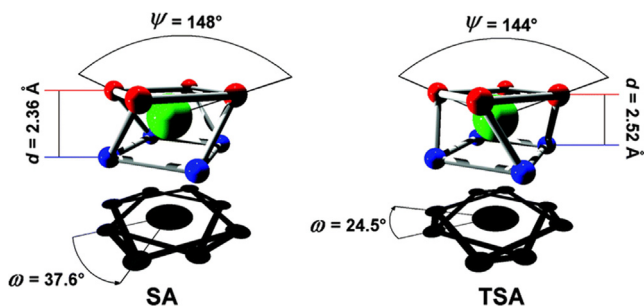
Fig. 24. Coordination polyhedra of the SA of [Pr(DOTA)(H$_2$O)]$^-$ and TSA of [Ce(DOTA)(H$_2$O)]$^-$. The coordinated water molecules are omitted. Oxygen atoms are represented red, nitrogens blue and lanthanides green. ω, d and ψ are defined in the text and represent average values for each structure [226,233]. Reproduced from Ref. [233] with permission from The Royal Society of Chemistry.

series as a result of the lanthanide contraction, but not steadily. They are approximately constant for Ce^{3+}-Sm^{3+} (log K_{LnL} = 23.39 for Ce^{3+}, 22.99 for Nd^{3+}), followed by a sharp increase at Eu^{3+}-Gd^{3+} (to log K_{LnL} = 23.45 for Eu^{3+}, 24.67 for Gd^{3+}), then they are again approximately constant at Gd^{3+}-Tm^{3+}, with a final increase at the end of the series (Yb^{3+}-Lu^{3+}) to log K_{LuL} = 25.41 [236].

NMR studies demonstrated that the macrocyclic Ln(DOTA)$^-$ complexes exist in solution as mixtures of two slowly interconverting structural isomers with different populations, which, at convenient temperatures, originate two sets of six and four peaks in their ^{1}H and ^{13}C NMR spectra, respectively, indicating that the structures of the two isomers have C_4-symmetry [237–240]. The presence of a Eu^{3+}-coordinated water molecule in each of the

two isomers of Eu(DOTA)$^-$ ($q = 1$) in aqueous solution has been confirmed by luminescence decay studies. [241,242]. A study of the Ln^{3+}-induced ^{17}O shifts of water in aqueous solutions of Ln (DOTA)$^-$ showed that they are dominated by their pseudocontact contribution and have only a small contact shift contribution [220]. A relatively large PCS of the ^{17}O resonance of the Ln^{3+}-bound water suggests a restricted position of a single ^{17}O nucleus of the coordinated water molecule on the C_4-axis of the complex, corresponding to the main symmetry axis of its magnetic susceptibility tensor (Eq. (4) for axial symmetry, $\Delta\chi_{rh} = 0$). Using Eqs (10) and (11), F-values of 0.131 and 0.0923 at 301 K were obtained for the light and heavy lanthanides, respectively. These data imply that the ^{17}O hyperfine coupling constant does not change much and that $q = 1$ along the Ln-series [220].

In early work, Desreux et al. studied the temperature dependence of the ^{1}H and ^{13}C NMR spectra for the complexes with the diamagnetic La^{3+} and Lu^{3+} and the paramagnetic Pr^{3+}, Eu^{3+} and Yb^{3+}. Only the "major" isomer of these complexes was identified and it was shown that the macrocyclic ring structure is very rigid [237]. The observed ^{1}H paramagnetic shift ratios were found to be dependent on the Ln^{3+}-ion under study, indicating the presence of contact contributions. As the complexes have a C_4-symmetry axis, the model for axial symmetry (Eq. (4), $\Delta\chi_{rh} = 0$), was used to define qualitative structural information on the complexes in aqueous solution, but it was not possible to define the conformation of their pendant arms, and the "minor" isomers were not recognized [227,237].

More recently, Aime *et al.* elucidated the solution structures and dynamics of the whole series of Ln(DOTA)$^-$ complexes (Ln ≠ Pm) using ^{1}H and ^{13}C NMR techniques at higher magnetic fields, includ-

ing 2D COSY and EXSY spectra [238]. The spectra of the two structural isomers observed for each paramagnetic complex showed great similarity, but one isomer induces larger paramagnetic shifts than the other, resulting from their different magnetic susceptibility anisotropies. The similarity of the vicinal ^{1}H coupling constants of the ethylene protons led to conclude that the conformation of the macrocycle is the same in the two isomers present for each complex and that they only differ in the layout of their acetate arms. The distances between the Ln^{3+}-ion and the ligand protons in the Tb^{3+}, Dy^{3+}, Ho^{3+}, and Yb^{3+}-complexes were calculated from the difference of the Curie contribution to their paramagnetic T_2 and T_1 relaxation (see Eqs. (20) and (21)) [238,243]. However, this approach did not take into consideration the contribution of the anisotropy of the magnetic susceptibility tensor to the Curie terms, as discussed before (Eqs. (25)–(28)) [52]. Still, it was observed that the proton paramagnetic shifts of the "major" isomer of the Yb (DOTA)$^-$ complex, which are dominated by the PCS contribution, agree very well with those calculated from the crystal structures of the Gd^{3+} and Eu^{3+}-complexes described above, which corresponds to the SA isomer. The structure of this isomer was changed by stepwise variation of the torsion angle Ln-N-C-COO until the fit between calculated and observed proton PCS for the "minor" isomer was optimal. For the optimum fit, the arrangement of the acetate arms corresponds to a TSA structure with an orientation of the acetate arms that is inverted with respect to the main isomer, thus with a negative and smaller angle of rotation (ω) between the N_4 and O_4-planes. In summary, the quantitative interpretation of the observed proton PCS of Yb(DOTA)$^-$ allowed to conclude that the two structural isomers present in solution are enantiomeric pairs of diastereoisomers with capped SA and TSA geometries, highlighting the similarity between the solid-state and the solution structure of the complexes [238].

The dynamics of the Ln(DOTA)$^-$ systems are summarized in Fig. 23. The two stereoisomeric pairs of enantiomers, $\Lambda(\delta\delta\delta\delta)/\Delta(\lambda\lambda\lambda\lambda)$ and $\Delta(\delta\delta\delta\delta)/\Lambda(\lambda\lambda\lambda\lambda)$, can interconvert in solution by changing the conformation of the macrocyclic unit ($\delta\delta\delta\delta$) ↔ ($\lambda\lambda\lambda\lambda$) or by rotating the four acetate arms (Δ ↔ Λ). Each process by itself exchanges the SA and TSA geometries, while the two concerted or successive processes results in the interconversion of enantiomeric pairs. Variable temperature ^{13}C spectra of the Nd^{3+}-complex and ^{1}H EXSY of the Eu^{3+} and Yb^{3+}-complexes indicated that the exchange processes among the isomers are not coupled with the rearrangement of the macrocycle [238]. By solving the rate constants from the exchange matrix obtained by variable temperature EXSY spectra of Yb(DOTA)$^-$, it became apparent that all four conformational isomers are exchanging with each other [240]. The activation parameters ($\Delta G^{\ddagger 298}$) obtained for the arm rotation and ring inversion processes were very similar, suggesting a concerted enantiomerization mechanism. The results from other qualitative ^{1}H EXSY [238,239] and variable temperature ^{13}C NMR studies [231,238] point to a faster arm rotation than ring inversion. All results confirm the much higher rigidity of the Ln (DOTA)$^-$ complexes of DOTA in comparison with the complexes of DTPA derivatives. It also explains why the geometry of the Ln-DOTA system is radically influenced compared to systems with more flexible ligands.

The equilibrium TSA ⇄ SA shifts to the right in aqueous solutions of the Ln(DOTA)$^-$ complexes with decreasing size of the Ln^{3+}-ion (see Fig. 25). Other factors such as the concentration of inorganic salts present in the solution, temperature, or even pressure, also influence the ratio SA/TSA [238,239,244]. The near-zero activation volumes, obtained for the isomerization process by high-pressure NMR, shows that, in all these cases, it is purely conformational (see Fig. 25) [244]. However, large positive activation volumes, obtained for the isomerizations of the complexes of the smallest cations (Tm^{3+}-Lu^{3+}) combined with the observation of

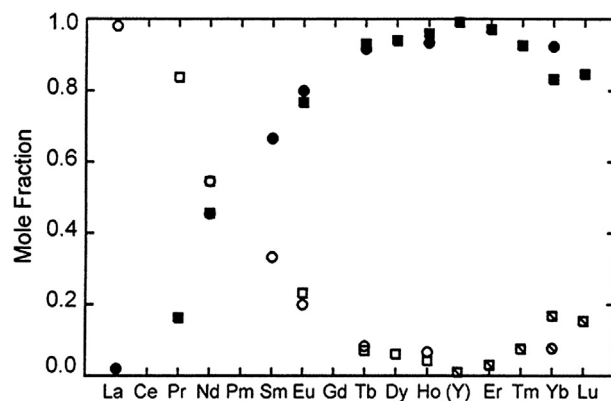**Fig. 25.** Molar fractions of the isomers TSA + TSA′ (open symbols) and SA (filled symbols) of $[Ln(DOTA)(H_2O)_x]^-$ ($x = 1,0$) as a function of the complexed metal ion from ^{1}H NMR spectroscopy (0.15 M Ln(DOTA)$^-$, pH 7.0, T = 298 K, ionic strength = 0.3 M). Squares: data from Ref. [244]; circles: data from Ref. [239]. Reprinted with permission from Ref. [244] Copyright (1997) American Chemical Society.

an accompanying decrease of the SA/TSA ratio (see Fig. 25) suggests that for these ions, in addition, a fast water dissociation process and conformational rearrangement is involved, leading to the SA′ geometry (with q = 0). The TSA isomer is stabilized relative to the SA isomer by the presence of high concentrations of non-coordinating salts, likely due to preferential (weak) interactions with ions and water-solvent stabilization effects. Thus, the solution NMR studies agree well with the X-ray data. The cavity sizes of the structures are in the order TSA > SA > TSA′ > SA′ and determine the relative isomeric solution populations of the complexes along the Ln series. The SA/SA′ structures are more compact than the TSA/TSA′, leading to larger paramagnetic shifts in solution [244,245]. In most cases, the crystal structure obtained corresponds to the most populated isomer in solution. The two exceptions are Pr(DOTA)$^-$ which crystallizes in the SA form although, in
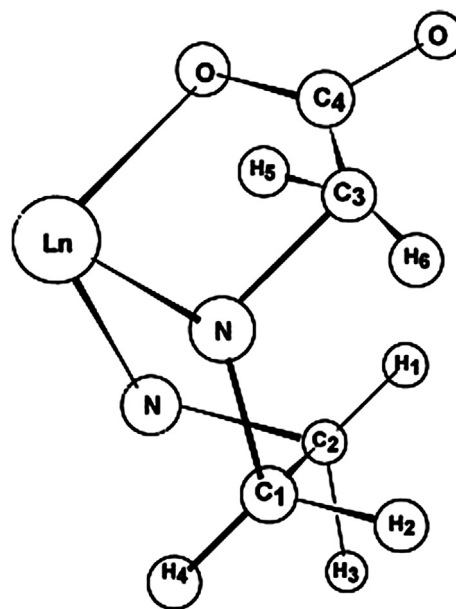

Fig. 26. Model of a fragment of the structure of the corresponding Ln^{3+} complexes in the $\Delta(\lambda\lambda\lambda\lambda)$ enantiomeric form of the SA isomer. Symmetry-related atoms are not shown for clarity. The numbering scheme for the hydrogen and carbon/phosphorous atoms is also shown. H_5 denotes the pro-R and H_6 the pro-S methylene protons of the pendant arm.

solution, the TSA is dominant (82%), and Tm(DOTA)$^-$ that crystalizes as TSA' and occurs in solution as 92% SA and 8% TSA'. An EXAFS study pointed to high similarities between the coordination environments of Gd^{3+} in aqueous solution and in [Gd(DOTA)(H$_2$O)]$^-$ and [Gd(DTPA)(H$_2$O)]$^{2-}$ crystals, with very similar calculated d(Ln-O$_w$), d(Ln-N$_{av}$) and d(Ln-O$_{av}$) values [246].

The ^{1}H and ^{13}C LIS data available (see atom numbering scheme in Fig. 26) for the SA and TSAP isomers of the paramagnetic Ln(DOTA)$^-$ complexes [238,245] were analyzed by plotting the data according to Eqs. (10) and (11) [247,248]. Sm, as usual, was excluded from these plots, and, due to low isomer populations, ^{1}H and ^{13}C LIS values of the SA isomer were only available for Ln = Nd-Eu in the first half of the lanthanide series, whereas ^{13}C LIS values for the TSA isomer in the second half of the series were only available for Yb (TSA'). Using the available data, breaks between light and heavy lanthanide ions were observed in most of these plots (see e.g. Fig. 27), reflecting variations in the values of both F_i and $B_0^2 G_i$. Data for Ln = Tm and Yb are systematically outliers in plots for the second half of the Ln-series.

The same sets of LIS data were also plotted according to Eq. (12), in which the crystal field parameter B_0^2 is factored out (Fig. 28a). These plots again show breaks between the light and the heavy lanthanide ions, which, however, are much less significant than

in the previous cases. The breaks observed in these plots indicate that the F_i and R_{ik} parameters change halfway through the series, together with changes of B_0^2. The breaks of the plots according to Eq. (12) are smaller than in those according to Eq. (11) because of the absence of B_0^2 in Eq. (12). Another reason might be that the geometric ratios, R_{ik}, may be much less affected by the smaller effects on G_i values due to structural changes resulting from the lanthanide contraction.

Plots of the LIS data according to Eq. (13), which eliminates the effect of variations of both B_0^2 and $< S_z >$ were made for combinations of three ^{13}C or ^{1}H nuclei of each isomer along the Ln(DOTA)$^-$ series. Fig. 28b,c shows some data of the SA and TSA isomers. In some cases, good linear correlations with R^2 = 0.999 are obtained (Fig. 28b,c) but with different combinations of nuclei, breaks originate at the middle of the series, which are more or less pronounced. This is in agreement with the changes of F_i and G_i parameters observed in the middle of the Ln series for these complexes, which illustrates that the linearity of some of the plots according to Eq. (13) may be accidental. From the above plots, it may be concluded that the parameters F_i, B_0^2, and G_i for the Ln-DOTA system are different in both the SA and the TSA conformational isomers. The value of B_0^2 for the SA conformer is larger than for the TSA conformer, which most likely can be ascribed to the more oblate shape of the Ln^{3+}-coordination polyhedron of the former conformer [24]. Fig. 28 suggests that the variations in G_i might be minor and therefore, possibly caused by amplification of tiny geometric changes along the series due to the data manipulation.

More insights in geometries, reaction mechanisms, and energy barriers for the Ln(DOTA)$^-$ system were obtained by *ab initio* calculations for Ln = La, Gd, Ho, Lu, both in the gas phase and in water. For the calculations in water, the polarizable continuum model (PCM) was employed [249]. The geometry optimizations carried out within the large-core approximation at the HF level provided two minima corresponding to 9-coordinated SA and TSA geometries (q = 1), except for Lu, where calculations in water indicated that the 8-coordinated TSA' (q = 0) is more favorable. These results agree with the experimental data discussed above. However, in order to obtain relative energies between the SA and TSA isomers in agreement with the experimental data, single-point energy calculations at the DFT level (B3LYP model) were needed. In this way, the computations confirmed the experiments that showed that the stability of the TSA conformers decreased in stability relative to the SA conformers with the decrease of the Ln^{3+} radius along the Ln-series. Furthermore, they also showed the dominance of 9-coordinated [Ln(DOTA)(H$_2$O)]$^-$ at the beginning of the series and of the 8-coordinated [Ln(DOTA)]$^-$ at the end. For the Lu^{3+} complex a stabilization of the TSA' isomer was observed for calculations in solution (but not in the gas phase). The interconversion between the SA and TSA isomers in [Lu(DOTA)]$^-$ was investigated by using large-core RECPs and both HF and DFT calculations (B3LYP model) [250]. These calculations showed that the cyclen moiety inverts stepwise from the $\delta\delta\delta\delta$ to the $\lambda\lambda\lambda\lambda$ configuration through four transition states in each of which one of the ethylene bridges is nearly eclipsed (Fig. 29). HF calculations indicated that a stepwise conversion is energetically preferred over a concerted one [251]. Conversely, the Δ to Λ inversion in [Lu(DOTA)]$^-$ takes place through a one-step mechanism with a concerted rotation of the four acetate arms. The activation energies provided by these computations agreed very well with the values obtained experimentally by NMR.

The structure and dynamic properties of the macrocyclic Ln^{3+}-DOTP complexes (DOTP = 1,4,7,10-tetra-azacyclododecane-N,N',N'',N''''-tetramethylenephosphonic acid, Fig. 22) have been investigated using X-ray diffraction, multinuclear NMR and computational techniques. The only X-ray crystal structure available for this series of complexes is that of Na$_5$[Gd(DOTP)], which shows two different configurations of Gd(DOTP)$^{5-}$ each on one side of a
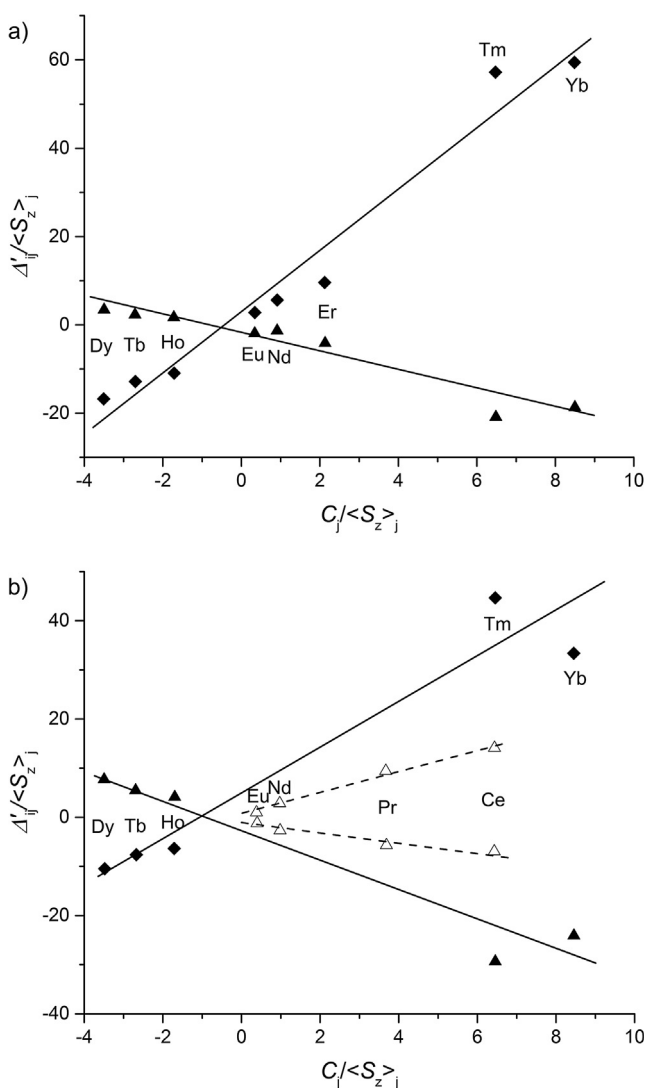
Fig. 27. Plots of the ^{1}H LIS values for (a) H$_4$ (◆) and H$_6$ (▲) of the SA isomer (Nd-Yb) and (b) H$_4$ (Ce-Eu ◇, Tb-Yb ◆) and H$_6$ (Ce-Eu △, Tb-Yb ▲) of the TSA/TSA' isomer of Ln(DOTA)$^-$ according to Eq. (11) (pH 7, 298 K). Redrawn from Ref. [248].
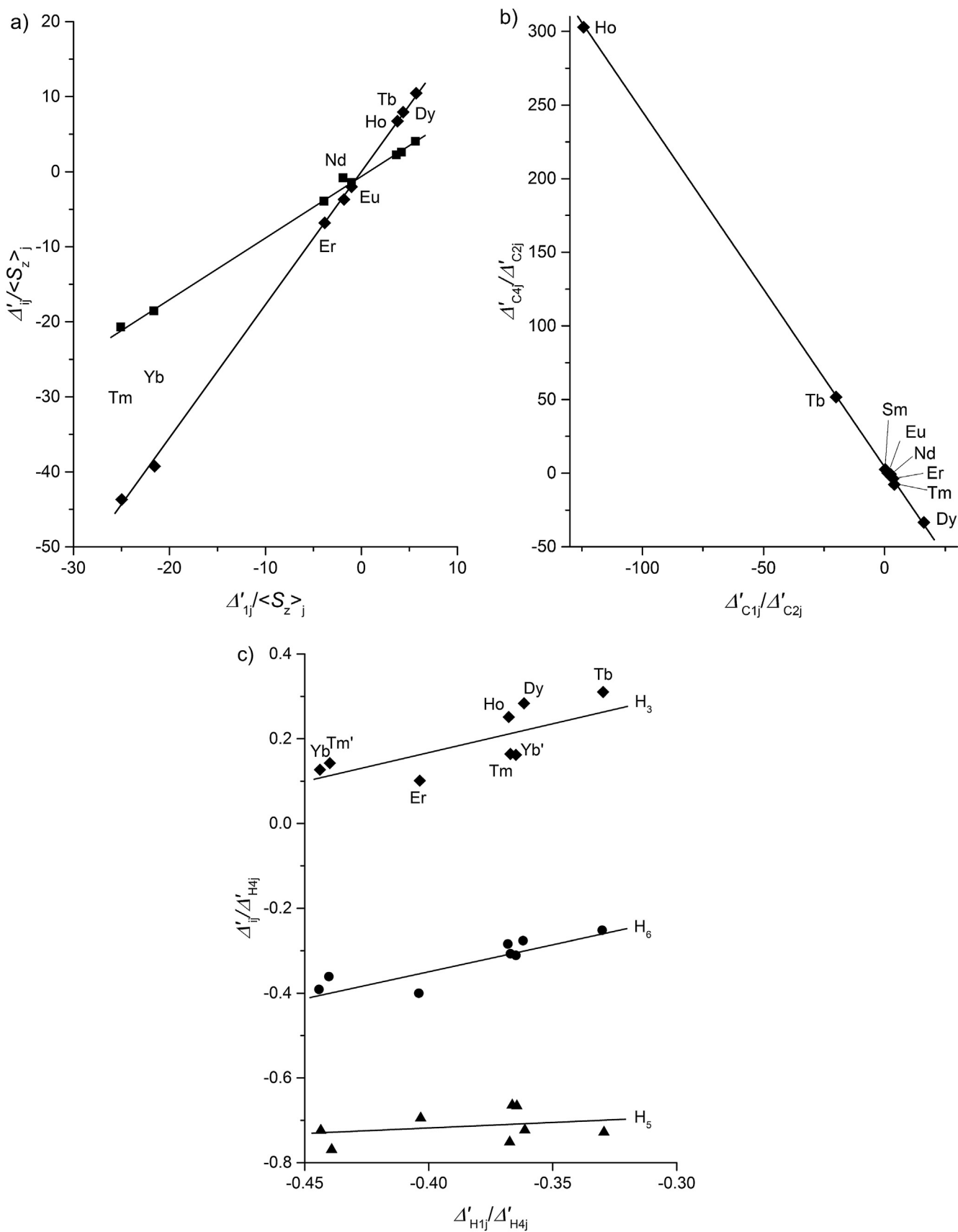
Fig. 28. (a) Plots of the ^{1}H LIS values of Ln(DOTA)$^-$ (Ln = Ce-Yb) according to Eq. (12) for the H$_5$-H$_1$ (◆) and H$_6$-H$_1$ (■) pairs; (b) plots according to Eq. (13) for the C$_4$,C$_1$,C$_2$ triad of the SA isomer (◆); (c) plots according to Eq. (13) for the H$_i$, H$_1$, H$_4$ triads (i = 3 (◆), 5 (▲), 6 (●)) of the TSA isomer [16,248].
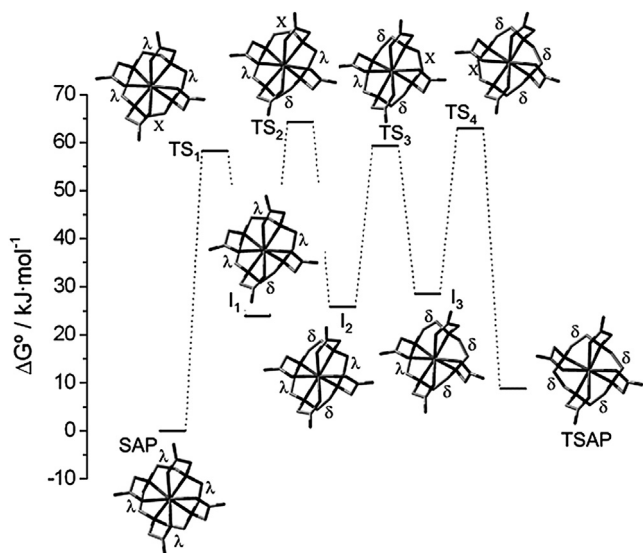
**Fig. 29.** *In vacuo* relative free energies of minima, intermediates (I), and transition states (TS) involved in the ring inversion process of [Lu(DOTA)]$^-$ obtained from DFT calculations (B3LYP) [250]. Reproduced from Ref. [36].

sheet of clustered hydrated Na$^+$ ions [252]. Gd^{3+} ions in both forms of the chelate have $q = 0$ and are bound in an 8-coordinated fashion through the four N-atoms and the four phosphonate O-atoms. The Gd^{3+}-complexes occur as a racemic mixture of $\Delta(\delta\delta\delta\delta)$ and $\Lambda(\lambda\lambda\lambda\lambda)$ TSA′ configurations and in C_4-symmetrical geometries with two slightly different twist angles ($\omega = -27.07°$ and $-23.67°$). One type of [Gd(DOTP)]$^{5-}$ anions is bound to four Na$^+$ ions in the cluster through O-atoms of adjacent ligand phosphonate groups that are not coordinating to Gd^{3+}, while the other type is linked to the cluster only through hydrogen bonds. The preference of [Gd(DOTP)]$^{5-}$ for a TSA′ geometry ($q = 0$) in the solid state, whereas [Gd(DOTA)(H$_2$O)]$^-$ adopts an SA geometry ($q = 0$), can be explained by the difference in steric demands and the negative charge density between carboxylate and phosphonate groups. The bulkiness of the phosphonate groups results in a smaller opening angle ψ, which together with the Coulomb repulsion prevents a water molecule to enter the first coordination sphere of the complexes [233].

The [Ln(DOTP)]$^{5-}$ complexes have been thoroughly studied in aqueous solution using several multinuclear NMR techniques [40,253–255]. Studies of their hydration state using luminescence lifetime measurements of [Eu(DOTP)]$^{5-}$ [256], ^{17}O NMR shift measurements on [Dy(DOTP)]$^{5-}$ [40] and ^{1}H NMRD profiles of [Gd(DOTP)]$^{5-}$ [257,258] lead to the conclusion that $q = 0$ and that two water molecules are located in the second coordination sphere, where they interact with the charged phosphonate oxygens. The ^{1}H and ^{13}C NMR spectra of the diamagnetic [Ln(DOTP)]$^{5-}$ complexes (Ln = La, Lu) showed that they are stereochemically quite rigid [254], with a higher activation energy for $\delta\delta\delta\delta \leftrightarrow \lambda\lambda\lambda\lambda$ inversion of the macrocycle than for the corresponding DOTA complexes [237]. The [Ln(DOTP)]$^{5-}$ chelates also have a remarkably high thermodynamic stability (log $K_{LnL} = 27.1 \pm 0.2$ for La^{3+}-Gd^{3+}) as well as an extremely high inertness [259]. Potentiometric and ^{31}P NMR studies revealed four protonation steps in the range pH 2 – 10. Under physiological conditions (pH (7.4)), the monoprotonated H[Ln(DOTP)]$^{4-}$ species predominates. The solution structures of 11 paramagnetic Ln^{3+}-DOTP-complexes were examined by ^{1}H, ^{13}C, ^{31}P, and ^{23}Na NMR spectroscopy and MM calculations [254]. All spectra revealed a single set of NMR signals in aqueous solutions. ^{23}Na NMR shift studies induced by [Tm(DOTP)]$^{5-}$ binding to the Na$^+$ counter-cations provided, together with MMX calculations, a binding model [40,259] that afforded a rationalization of

the very large observed ^{23}Na PCS induced by [Ln(DOTP)]$^{5-}$. [Ln(DOTP)]$^{5-}$ complexes are because of their high negative charge unable to pass cell membranes, which has led to their utilization as shift reagents for the discrimination of the degenerate intra- and extracellular ^{23}Na NMR resonances [260]. [Tm(DOTP)]$^{5-}$ complexes are extremely effective shift reagents in ^{23}Na NMR studies of perfused organs and of small animals *in vivo* [261].

As opposed to DOTA complexes, [Ln(DOTP)]$^{5-}$ complexes are present in solution exclusively as a racemic mixture of the $\Delta(\delta\delta\delta\delta)$ and $\Lambda(\lambda\lambda\lambda\lambda)$-TSA′ isomers. Plots of the ^{1}H, ^{13}C, and ^{31}P LIS values (at 298 K, pH 10) [40,247,254] according to Eq. (11), show large breaks halfway through the series, in addition to systematic outliers for Tm and Yb on the curves for the second half of the series (see Fig. 30a). This suggests that F_i and $B_0^2 G_i$ change halfway the series and maybe also at Tm and Yb. To discriminate between variations B_0^2 and G_i, the data were also plotted according to the crystal field parameter independent method (Eq. (12)). These plots also showed breaks (but less significant) at Tb (Fig. 30b), indicating that B_0^2, F_i, R_{ik} and possibly also G_i all change halfway through the series. Assuming that H$_4$ has no contact shift contribution, F_i and $R_{iH4} = G_i/G_{H4}$ values were obtained for i = C$_1$, C$_2$, C$_P$ and P nuclei,
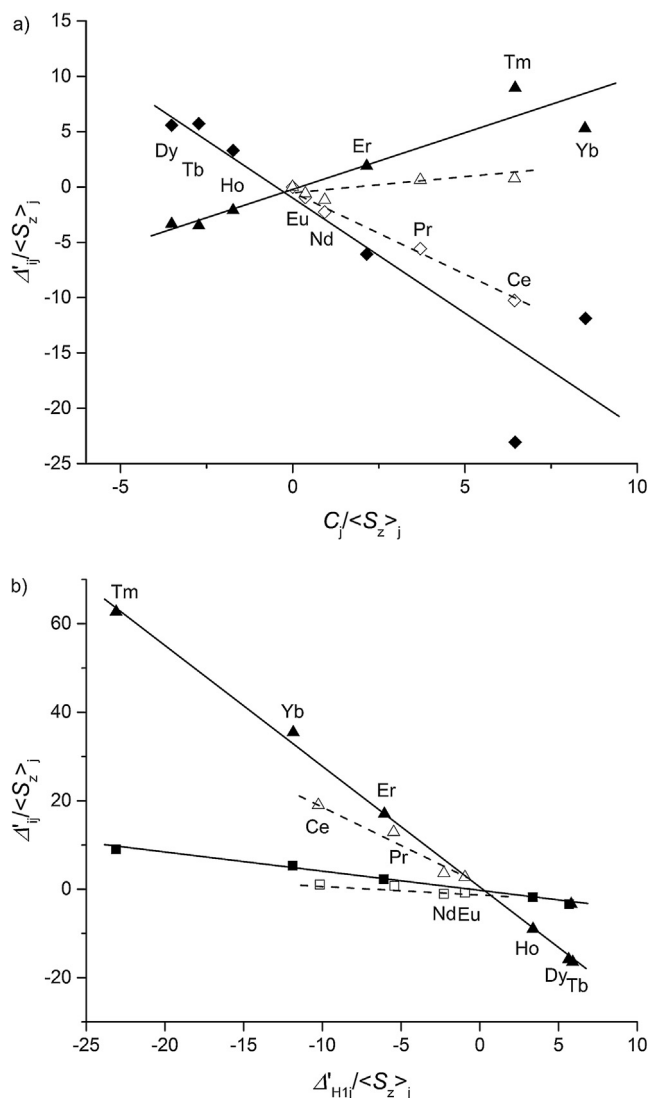
Fig. 30. Plots of the ^{1}H LIS values of Ln(DOTP)$^{5-}$, Ln = Ce-Yb: a) for H$_1$ (Ce-Eu ◇, Tb-Eu ◆) and H$_3$ (Ce-Eu △, Tb-Yb ▲) according to Eq. (11); (b) for the H$_3$-H$_2$ (Ce-Eu □, Tb-Yb ■) and H$_4$-H$_1$ (Ce-Eu △, Tb-Yb ▲) pairs according to Eq. (12) (pH 10, 298 K) [16,248].

as well as the B_0^2 values for the Tb-Yb complexes. These results have shown that B_0^2 changes significantly along the Tb-Yb half-series of complexes, the largest value being for Tm and the smallest for Yb [42].

Plots according to Eq. (13) using combinations of three ^1H, ^{13}C and ^{31}P shifts gave good linear relationships in some cases but more or less pronounced breaks for other combinations, which confirm the changes of F_i and G_i parameters detected with Eqs. ((11) and (12)) in the middle of the Ln series [245].

Computational studies based on classical molecular mechanics (CHARMM22 force field) or DFT calculations (B3LYP, large-core ECP for the lanthanides) supported a TSA′ structure of DOTP complexes in solution [250,262]. Molecular dynamics simulations have shown that a few water molecules are specifically bound to [Gd(DOTP)]$^{5-}$ through hydrogen bonds to the metal-unbound negative oxygens of the phosphonate groups, supporting the presence of a second hydration sphere in those complexes [263].

5. Conclusions

The gradual decrease of the ionic radius across the Ln-series is accompanied by an increasing steric strain in the complexes and charge density of the cations. These counteracting effects dominate the coordination chemistry of the lanthanides. General trends are gradual changes in the coordination polyhedra, the conformations of the bound ligands, complex stabilities (thermodynamic and kinetic), and dynamics, which are often accompanied by changes in coordination numbers.

By contrast to the chemical properties, the physical properties among the Ln-ions are very different. This propensity has appeared to be very useful for the structural elucidations of Ln-complexes. Recent progress in this field leads to the insight that particularly the geometry of the ligands around a Ln-cation may have a significant influence on the electronic properties. As a result, the relatively simple models to evaluate complex structures from spectroscopic data are not always adequate anymore. More complex models have been developed and computational methods are becoming increasingly important.

Since Mendeleev, the lanthanides have developed from an appendix to the periodic system into a multifaceted group of elements with many applications in science and technology, ranging from chemical catalysis to biomedical theranostics. The advance in the understanding of structure–property relationships of Ln-based connections and materials is invaluable for the design and alignment of new compounds.

Funding

Declaration of Competing Interest

The authors declare that they have no known competing financial interests or personal relationships that could have appeared to influence the work reported in this paper.

References

[1] D.I. Mendeleev, J. Russ. Chem. Soc. 3 (1869) 25.
[2] D.I. Mendeleev, Z. Chem. 12 (1869) 405–406.
[3] D.A. Johnson, A.F. Williams, Chimia 73 (2019) 144–151.
[4] R.D. Shannon, Acta Crystallogr. Sect. A 32 (1976) 751–767.
[5] P.L. Brown, R.N. Sylva, J. Ellis, J. Chem. Soc. Dalton Trans. (1985) 723–730.
[6] M. Seitz, A.G. Oliver, K.N. Raymond, J. Am. Chem. Soc. 129 (2007) 11153–11160.
[7] S.A. Cotton, P.R. Raithby, Coord. Chem. Rev. 340 (2017) 220–231.
[8] P. D'Angelo, A. Zitolo, V. Migliorati, G. Chillemi, M. Duvail, P. Vitorge, S. Abadie, R. Spezia, Inorg. Chem. 50 (2011) 4572–4579.
[9] P. D'Angelo, A. Zitolo, V. Migliorati, G. Mancini, I. Persson, G. Chillemi, Inorg. Chem. 48 (2009) 10239–10248.
[10] C. Cossy, A.C. Barnes, J.E. Enderby, A.E. Merbach, J. Chem. Phys. 90 (1989) 3254–3260.
[11] C. Cossy, L. Helm, D.H. Powell, A.E. Merbach, New J. Chem. 19 (1995) 27–35.
[12] D.M. Corsi, C. Platas-Iglesias, H. van Bekkum, J.A. Peters, Magn. Reson. Chem. 39 (2001) 723–726.
[13] J.A. Peters, M.S. Nieuwenhuizen, D.J. Raber, J. Magn. Reson. 65 (1985) 417–428.
[14] R.M. Golding, M.P. Halton, Aust. J. Chem. 25 (1972) 2577–2581.
[15] A.A. Pinkerton, M. Rossier, S. Spiliadis, J. Magn. Reson. 64 (1985) 420–425.
[16] C. Piguet, C.F.G.C. Geraldes, Paramagnetic NMR lanthanide induced shifts for extracting solution structures, K.A. Gschneidner, J.-C.G. Bünzli, V.K. Pecharsky (Eds.) Handbook on the Physics and Chemistry of Rare Earths, Elsevier Science B.V., Amsterdam, 2003, pp. 353-463.
[17] M. Autillo, L. Guerin, T. Dumas, M.S. Grigoriev, A.M. Fedoseev, S. Cammelli, P. L. Solari, D. Guillaumont, P. Guilbaud, P. Moisy, H. Bolvin, C. Berthon, Chem. Eur. J. 25 (2019) 4435–4451.
[18] B. Bleaney, C.M. Dobson, B.A. Levine, R.B. Martin, R.J.P. Williams, A.V. Xavier, J. Chem. Soc. Chem. Commun. (1972) 791–793.
[19] M. Allegrozzi, I. Bertini, M.B.L. Janik, Y.M. Lee, G.H. Lin, C. Luchinat, J. Am. Chem. Soc. 122 (2000) 4154–4161.
[20] B. Bleaney, J. Magn. Reson. 8 (1972) 91–100.
[21] I. Bertini, C. Luchinat, G. Parigi, Concepts Magn. Reson. 14 (2002) 259–286.
[22] I. Bertini, C. Luchinat, G. Parigi, Prog. Nucl. Magn. Reson. Spectrosc. 40 (2002) 249–273.
[23] M.D. Kemple, B.D. Ray, K.B. Lipkowitz, F.G. Prendergast, B.D.N. Rao, J. Am. Chem. Soc. 110 (1988) 8275–8287.
[24] C. Görller-Walrand, K. Binnemans, Rationalization of crystal-field parametrization, in: Handbook on the Physics and Chemistry of Rare Earths, Elsevier, 1996, pp. 121–283.
[25] T.A. Babushkina, V.F. Zolin, L.G. Koreneva, J. Magn. Reson. 52 (1983) 169–181.
[26] B.R. McGarvey, J. Magn. Reson. 33 (1979) 445–455.
[27] A.M. Funk, K.-L.N.A. Finney, P. Harvey, A.M. Kenwright, E.R. Neil, N.J. Rogers, P. Kanthi Senanayake, D. Parker, Chem. Sci. 6 (2015), 1655–1662 and references therein.
[28] V.S. Mironov, Y.G. Galyametdinov, A. Ceulemans, C. Görller-Walrand, K. Binnemans, J. Chem. Phys. 116 (2002) 4673–4685.
[29] J.D. Rinehart, J.R. Long, Chem. Sci. 2 (2011) 2078–2085.
[30] H.J. Hogben, M. Krzystyniak, G.T.P. Charnock, P.J. Hore, I. Kuprov, J. Magn. Reson. 208 (2011) 179–194.
[31] M.-E. Boulon, G. Cucinotta, J. Luzon, C. Degl'Innocenti, M. Perfetti, K. Bernot, G. Calvez, A. Caneschi, R. Sessoli, Angew. Chem. Int. Ed. 52 (2013) 350–354.
[32] A.E. Suturina, K. Mason, C.F.G.C. Geraldes, I. Kuprov, D. Parker, Angew. Chem. Int. Ed. Engl. 56 (2017) 12215–12218.
[33] C.N. Reilley, B.W. Good, J.F. Desreux, Anal. Chem. 47 (1975) 2110–2116.
[34] J. Reuben, J. Magn. Reson. 50 (1982) 233–236.
[35] J.A. Peters, J. Huskens, D.J. Raber, Progr. Nucl. Magn. Reson Spectrosc. 28 (1996) 283–350.
[36] J.A. Peters, K. Djanashvili, C.F.G.C. Geraldes, C. Platas-Iglesias, Structure, Dynamics and Computational Studies of Lanthanide-Based Contrast Agents, John Wiley & Sons Ltd., 2013, pp. 209–276.
[37] S. Di Pietro, S.L. Piano, L. Di Bari, Coord. Chem. Rev. 255 (2011) 2810–2820.
[38] C.N. Reilley, B.W. Good, R.D. Allendoerfer, Anal. Chem. 48 (1976) 1446–1458.
[39] J.A. Peters, J. Magn. Reson. 68 (1986) 240–251.
[40] J. Ren, A.D. Sherry, J. Magn. Reson. Ser. B 111 (1996) 178–182.
[41] C.F.G.C. Geraldes, S. Zhang, C. Platas, T. Rodriguez-Blas, A. De Blas, A.D. Sherry, J. Alloys Compd. 323–324 (2001) 824–827.
[42] D. Parker, E. Suturina, A. Harnden, A. Batsanov, M. Fox, K. Mason, M. Vonci, E. McInnes, N. Chilton, Angew. Chem. Int. Ed. Engl. 58 (2019) 10290–10294.
[43] I. Rodriguez-Rodriguez, D. Esteban-Gomez, A. de Blas, T. Rodriguez-Blas, M. Botta, R. Tripier, C. Platas-Iglesias, Inorg. Chem. 51 (2012) 13419–13429.
[44] I. Bertini, C. Luchinat, G. Parigi, E. Ravera, NMR of Paramagnetic Molecules; Applications to Metallobiomolecules and Models, second ed., Elsevier, Boston, 2015.
[45] I. Solomon, Phys. Rev. 99 (1955) 559–565.
[46] N. Bloembergen, L.O. Morgan, J. Chem. Phys. 34 (1961) 842–850.
[47] N. Bloembergen, J. Chem. Phys. 27 (1957) 572–573.
[48] M. Gueron, J. Magn. Reson. 19 (1975) 58–66.
[49] L. Helm, Progr. Nucl. Magn. Reson Spectrosc. 49 (2006) 45–64.
[50] N. Schaefle, R. Sharp, J. Magn. Reson. 176 (2005) 160–170.
[51] A.J. Vega, D. Fiat, Mol. Phys. 31 (1976) 347–355.
[52] E. Suturina, K. Mason, C.F.G.C. Geraldes, N.F. Chilton, D. Parker, I. Kuprov, Phys. Chem. Chem. Phys. 20 (2018) 17676–17686.
[53] H.R. Leverentz, H.W. Qi, D.G. Truhlar, J. Chem. Theory Comput. 9 (2013) 995–1006.
[54] K. Vanommeslaeghe, O. Guvench, A.D. MacKerell Jr., Curr. Pharm. Des. 20 (2014) 3281–3292.
[55] K. Vanommeslaeghe, M. Yang, A.D. MacKerell Jr., J. Comp. Chem. 36 (2015) 1083–1101.
[56] D. Bini, M. Gregori, U. Cosentino, G. Moro, A. Canales, A. Capitoli, J. Jimenez-Barbero, L. Cipolla, Carbohydr. Res. 354 (2012) 21–31.

[57] U. Cosentino, D. Pitea, G. Moro, G.A.A. Saracino, A. Villa, Phys. Chem. Chem. Phys. 11 (2009) 3943–3950.
[58] W. Thiel, Wiley Interdiscip. Rev. Comput. Mol. Sci. 4 (2014) 145–157.
[59] J.D.L. Dutra, M.A.M. Filho, G.B. Rocha, R.O. Freire, A.M. Simas, J.J.P. Stewart, J. Chem. Theory Comput. 9 (2013) 3333–3341.
[60] M.A.M. Filho, J.D.L. Dutra, G.B. Rocha, R.O. Freire, A.M. Simas, RSC Adv. 3 (2013) 16747–16755.
[61] M. Bursch, A. Hansen, S. Grimme, Inorg. Chem. 56 (2017) 12485–12491.
[62] M. Orio, D.A. Pantazis, F. Neese, Photosynth. Res. 102 (2009) 443–453.
[63] F. Neese, Coord. Chem. Rev. 253 (2009) 526–563.
[64] A. Roca-Sabio, M. Regueiro-Figueroa, D. Esteban-Gomez, A. de Blas, T. Rodriguez-Blas, C. Platas-Iglesias, Comput. Theor. Chem. (2012) 93–104.
[65] R. Car, M. Parrinello, Phys. Rev. Lett. 55 (1985) 2471–2474.
[66] R. Pollet, N.N. Nair, D. Marx, Inorg. Chem. 50 (2011) 4791–4797.
[67] A. Lasoroski, R. Vuilleumier, R. Pollet, J. Chem. Phys. 139 (2013) 104115.
[68] A. Lasoroski, R. Vuilleumier, R. Pollet, J. Chem. Phys. 141 (2014) 014201.
[69] H. Stoll, B. Metz, M. Dolg, J. Comp. Chem. 23 (2002) 767–778.
[70] M. Dolg, H. Stoll, A. Savin, H. Preuss, Theor. Chim. Acta 75 (1989) 173–194.
[71] M. Dolg, H. Stoll, H. Preuss, J. Chem. Phys. 90 (1989) 1730–1734.
[72] M. Regueiro-Figueroa, C. Platas-Iglesias, J. Phys. Chem. A 119 (2015) 6436–6445.
[73] M. Reiher, Theor. Chem. Acc. 116 (2006) 241–252.
[74] C. van Wüllen, J. Chem. Phys. 109 (1998) 392–399.
[75] A.S. Ivanov, V.S. Bryantsev, Eur. J. Inorg. Chem. 2016 (2016) 3474–3479.
[76] M. Dolg, J. Chem. Theory Comput. 7 (2011) 3131–3142.
[77] D.A. Pantazis, F. Neese, J. Chem. Theory Comput. 5 (2009) 2229–2238.
[78] D. Aravena, F. Neese, D.A. Pantazis, J. Chem. Theory Comput. 12 (2016) 1148–1156.
[79] J. Olsen, Int. J. Quantum Chem. 111 (2011) 3267–3272.
[80] J. Jung, M. Atanasov, F. Neese, Inorg. Chem. 56 (2017) 8802–8816.
[81] A.Y. Freidzon, I.A. Kurbatov, V.I. Vovna, Phys. Chem. Chem. Phys. 20 (2018) 14564–14577.
[82] S. Khan, R. Pollet, R. Vuilleumier, J. Kowalewski, M. Odelius, J. Chem. Phys. 147 (2017) 244306.
[83] C. Cossy, A.E. Merbach, Pure Appl. Chem. 60 (1988) 1785–1796.
[84] W.D. Horrocks, D.R. Sudnick, J. Am. Chem. Soc. 101 (1979) 334–340.
[85] A. Beeby, I.M. Clarkson, R.S. Dickins, S. Faulkner, D. Parker, L. Royle, A.S. de Sousa, J.A.G. Williams, M. Woods, J. Chem. Soc. Perkin Trans. 2 (1999) 493–504.
[86] R.M. Supkowski, W.D. Horrocks Jr., Inorg. Chim. Acta 340 (2002) 44–48.
[87] T. Kimura, Y. Kato, J. Alloys Compd. 225 (1995) 284–287.
[88] K. Djanashvili, J.A. Peters, Contrast Media Mol. Imaging 2 (2007) 67–71.
[89] A.P.G. Kieboom, J.M. van der Toorn, J.A. Peters, W.M.M.J. Bovée, A. Sinnema, C.A.M. Vijverberg, H. van Bekkum, Recl. Trav. Chim. Pays.-Bas. 97 (1978) 247–248.
[90] C.A.M. Vijverberg, J.A. Peters, A.P.G. Kieboom, H. van Bekkum, Recl. Trav. Chim. Pays-Bas 99 (1980) 403–409.
[91] M.C. Alpoim, A.M. Urbano, C.F.G.C. Geraldes, J.A. Peters, J. Chem. Soc. Dalton Trans. (1992) 463–467.
[92] K. Djanashvili, C. Platas-Iglesias, J.A. Peters, Dalton Trans. (2008) 602–607, and references therein.
[93] X. Zhao, M. Wong, C. Mao, T.X. Trieu, J. Zhang, P. Feng, X. Bu, J. Am. Chem. Soc. 136 (2014) 12572–12575.
[94] G. Anderegg, Critical Evaluation of Equilibrium Constants in Solution: Stability Constants of Metal Complexes IUPAC Chemical Data Series, Pergamon Press, Oxford, 1977, pp. 1–36.
[95] G. Anderegg, F. Arnaud-Neu, R. Delgado, J. Felcman, K. Popov, Pure Appl. Chem. 77 (2005) 1445–1495.
[96] A. Roca-Sabio, M. Mato-Iglesias, D. Esteban-Gómez, E. Tóth, A. de Blas, C. Platas-Iglesias, T. Rodríguez-Blas, J. Am. Chem. Soc. 131 (2009) 3331–3341.
[97] M.P. Jensen, R. Chiarizia, I.A. Shkrob, J.S. Ulicki, B.D. Spindler, D.J. Murphy, M. Hossain, A. Roca-Sabio, C. Platas-Iglesias, A. de Blas, T. Rodríguez-Blas, Inorg. Chem. 53 (2014) 6003–6012.
[98] N.A. Thiele, S.N. MacMillan, J.J. Wilson, J. Am. Chem. Soc. 140 (2018) 17071–17078.
[99] N.A. Thiele, V. Brown, J.M. Kelly, A. Amor-Coarasa, U. Jermilova, S.N. MacMillan, A. Nikolopoulou, S. Ponnala, C.F. Ramogida, A.K.H. Robertson, C. Rodríguez-Rodríguez, P. Schaffer, C. Williams Jr., J.W. Babich, V. Radchenko, J.J. Wilson, Angew. Chem. Int. Ed. 56 (2017) 14712–14717.
[100] N.A. Thiele, J.J. Woods, J.J. Wilson, Inorg. Chem. 58 (2019) 10483–10500.
[101] C.A. Chang, M.E. Rowland, Inorg. Chem. 22 (1983) 3866–3869.
[102] E. Brücher, B. Györi, J. Emri, P. Solymosi, L.B. Sztanyik, L. Varga, J. Chem. Soc. Chem. Commun. (1993) 574–575.
[103] C.A. Chang, V.O. Ochaya, Inorg. Chem. 25 (1986) 355–358.
[104] A. Roca-Sabio, M. Mato-Iglesias, D. Esteban-Gómez, A. de Blas, T. Rodríguez-Blas, C. Platas-Iglesias, Dalton Trans. 40 (2011) 384–392.
[105] L. Tei, Z. Baranyai, E. Brücher, C. Cassino, F. Demicheli, N. Masciocchi, G.B. Giovenzana, M. Botta, Inorg. Chem. 49 (2010) 616–625.
[106] J.L. Mackey, M.A. Hiller, J.E. Powell, J. Phys. Chem. 66 (1962) 311–314.
[107] M. Regueiro-Figueroa, D. Esteban-Gómez, A. de Blas, T. Rodríguez-Blas, C. Platas-Iglesias, Chem. Eur. J. 20 (2014) 3974–3981.
[108] R. Guillaumont, F. David, Radiochem. Radioanal. Lett. 17 (1974) 25–39.
[109] U. Cosentino, A. Villa, D. Pitea, G. Moro, V. Barone, J. Chem. Phys. B 104 (2000) 8001–8007.
[110] F.K. Kalman, A. Vegh, M. Regueiro-Figueroa, E. Tóth, C. Platas-Iglesias, G. Tircso, Inorg. Chem. 54 (2015) 2345–2356.

[111] F.H. Spedding, M.J. Pikal, B.O. Ayers, J. Phys. Chem. 70 (1966) 2440–2449.
[112] F.H. Spedding, K.C. Jones, J. Phys. Chem. 70 (1966) 2450–2455.
[113] F.H. Spedding, M.J. Pikal, J. Phys. Chem. 70 (1966) 2430–2440.
[114] A. Habenschuss, F.H. Spedding, J. Chem. Phys. 70 (1979) 3758–3763.
[115] A. Habenschuss, F.H. Spedding, J. Chem. Phys. 73 (1980) 442–450.
[116] T. Yamaguchi, M. Nomura, H. Wakita, H. Ohtaki, J. Chem. Phys. 89 (1988) 5153–5159.
[117] I. Persson, P. D'Angelo, S. De Panfilis, M. Sandström, L. Eriksson, Chem. Eur. J. 14 (2008) 3056–3066.
[118] P. D'Angelo, R. Spezia, Chem. Eur. J. 18 (2012) 11162–11178.
[119] R. Díaz-Torres, S. Alvarez, Dalton Trans. 40 (2011) 10742–10750.
[120] A.M. Van Loon, H. Van Bekkum, J.A. Peters, Inorg. Chem. 38 (1999) 3080–3084.
[121] J. Glaser, G. Johannesson, Acta Chem. Scand. A 35 (1988) 639–644.
[122] D. Parker, R.S. Dickins, H. Puschmann, C. Crossland, J.A.K. Howard, Chem. Rev. 102 (2002) 1977–2010.
[123] L. Helm, A.E. Merbach, Eur. J. Solid State Inorg. Chem. 28 (1991) 245–250.
[124] K. Binnemans, K.A. Gschneidner, J.C.G. Bünzli, V.K. Pecharsky, Handbook on the Physics and Chemistry of Rare Earths, 2005.
[125] L. Helm, A.E. Merbach, Chem. Rev. 105 (2005) 1923–1960.
[126] C. Cossy, L. Helm, A.E. Merbach, Inorg. Chem. 28 (1989) 2699–2703.
[127] S. Galera, J.M. Lluch, A. Oliva, J. Bertran, F. Foglia, L. Helm, A.E. Merbach, New. J. Chem. 17 (1993) 773–779.
[128] S.F. Lincoln, Helv. Chim. Acta 88 (2005) 523–545.
[129] D.H. Powell, A.E. Merbach, Magn. Reson. Chem. 32 (1994) 739–745.
[130] D.P. Fay, D. Litchinsky, N. Purdie, J. Phys. Chem. 73 (1969) 544–552.
[131] J. Zhang, N. Heinz, M. Dolg, Inorg. Chem. 53 (2014) 7700–7708.
[132] J. Zhang, M. Dolg, J. Phys. Chem. A 119 (2015) 774–780.
[133] A. Abbasi, P. Lindqvist-Reis, L. Eriksson, D. Sandström, S. Lidin, I. Persson, M. Sandström, Chem. Eur. J. 11 (2005) 4065–4077.
[134] J. Albertsson, Act. Chem. Scand. 26 (1972) 1023–1044.
[135] J. Albertsson, Acta Chem. Scand. 26 (1972) 1005–1017.
[136] J. Albertsson, Act. Chem. Scand. 26 (1972) 985–1004.
[137] J.M. Harrowfield, Y. Kim, B. Skelton, A. White, Aust. J. Chem. 48 (1995) 807–823.
[138] J.M. Harrowfield, I. Ling, B.W. Skelton, A.N. Sobolev, A.H. White, Aust. J. Chem. 70 (2017) 485–493.
[139] G. Pompidor, O. Maury, J. Vicat, R. Kahn, Acta Crystallogr. Sect. D: Biol. Crystallogr. 66 (2010) 762–769.
[140] J.F. Desreux, C.N. Reilley, J. Am. Chem. Soc. 98 (1976) 2105–2109.
[141] B.M. Alsaadi, F.J.C. Rossotti, R.J.P. Williams, J. Chem. Soc. Dalton Trans. (1980) 597–602.
[142] H. Donato, R.B. Martin, J. Am. Chem. Soc. 94 (1972) 4129–4131.
[143] N. Ouali, B. Bocquet, S. Rigault, P.-Y. Morgantini, J. Weber, C. Piguet, Inorg. Chem. 41 (2002) 1436–1445.
[144] F. Renaud, C. Piguet, G. Bernardinelli, J.-C.G. Bünzli, G. Hopfgartner, Chem. Eur. J. 3 (1997) 1646–1659.
[145] S. Rigault, C. Piguet, J.-C.G. Bünzli, J. Chem. Soc. Dalton Trans. (2000) 2045–2053.
[146] D.R. Foster, F.S. Richardson, Inorg. Chem. 22 (1983) 3996–4002.
[147] S.C.J. Meskers, H.P.J.M. Dekkers, J. Phys. Chem. A 105 (2001) 4589–4599.
[148] B.M. Alsaadi, F.J.C. Rossotti, R.J.P. Williams, J. Chem. Soc. Dalton Trans. (1980) 813–816.
[149] J.J. Lessmann, W.D. Horrocks Jr., Inorg. Chem. 39 (2000) 3114–3124.
[150] Y. An, M.T. Berry, F.C.J.M. van Veggel, J. Phys. Chem. A 104 (2000) 11243–11247.
[151] J.A. Peters, J. Chem. Soc. Dalton Trans. (1988) 961–965.
[152] M. Vonci, E.J.L. McInnes, N.F. Chilton, K. Mason, A.T. Frawley, D. Parker, E.A. Suturina, S.G. Worswick, I. Kuprov, J. Am. Chem. Soc. (2017).
[153] K. Mason, A.C. Harnden, C.W. Patrick, A.W.J. Poh, A.S. Batsanov, E.A. Suturina, M. Vonci, E.J.L. McInnes, N.F. Chilton, D. Parker, Chem. Commun. 54 (2018) 8486–8489.
[154] E. Furet, K. Costuas, P. Rabiller, O. Maury, J. Am. Chem. Soc. 130 (2008) 2180–2183.
[155] D. Esteban-Gómez, L.A. Büldt, P. Pérez-Lourido, L. Valencia, M. Seitz, C. Platas-Iglesias, Inorg. Chem. 58 (2019) 3732–3743.
[156] J. Albertsson, I. Elding, Acta Chem. Scand., Ser. A 31 (1977) 21–30.
[157] J. Albertsson, Acta Chem. Scand. 24 (1970) 3527–3541.
[158] J. Albertsson, Acta Chem. Scand. 22 (1968) 1563–1578.
[159] L.J. Farrugia, R.D. Peacock, B. Stewart, Acta Crystallogr. Sect. C: Cryst. Struct. Commun. 56 (2000) e435–e436.
[160] F.R. Fronczek, A.K. Banerjee, S.F. Watkins, R.W. Schwartz, Inorg. Chem. 20 (1981) 2745–2746.
[161] R. Marsh, Acta Crystallogr. Sect. B: Struct. Sci. 65 (2009) 782–783.
[162] C. Kremer, J. Torres, S. Dominguez, J. Mol. Struct. 879 (2008) 130–149.
[163] I. Grenthe, I. Tobiasson, Acta Chem. Scand. 17 (1963) 2101–2112.
[164] I. Grenthe, J. Am. Chem. Soc. 83 (1961) 360–364.
[165] C.A.M. Vijverberg, J.A. Peters, A.P.G. Kieboom, H. van Bekkum, Recl. Trav. Chim. Pays-Bas 99 (1980) 287–288.
[166] C.A.M. Vijverberg, in: Thesis, Delft University of Technology, Delft, The Netherlands, 1984.
[167] L. Fusaro, Magn. Reson. Chem. 56 (2018) 1168–1178.
[168] A. Sonesson, Acta Chem. Scand. 13 (1959) 998–1010.
[169] I. Grenthe, Acta Chem. Scand. 23 (1969) 1253–1265.
[170] I. Grenthe, Acta Chem. Scand. 23 (1969) 1752–1764.
[171] I. Grenthe, Acta Chem. Scand. 25 (1971) 3347–3359.

[172] I. Grenthe, Acta Chem. Scand. 25 (1971) 3721–3736.
[173] I. Grenthe, Acta Chem. Scand. 26 (1972) 1479–1489.
[174] I. Farkas, A. Fischer, M. Lindsjö, Z. Anorg, Allg. Chem. 628 (2002) 1885–1889.
[175] M. van Duin, J.A. Peters, A.P.G. Kieboom, H. van Bekkum, Recl. Trav. Chim. Pays-Bas 108 (1989) 57–60.
[176] T. Stumpf, T. Fanghaenel, I. Grenthe, J. Chem. Soc., Dalton Trans. (2002) 3799–3804.
[177] T. Toraishi, I. Farkas, Z. Szabo, I. Grenthe, J. Chem. Soc., Dalton Trans. (2002) 3805–3812.
[178] C.A.M. Vijverberg, J.A. Peters, A.P.G. Kieboom, H. van Bekkum, Tetrahedron 42 (1986) 167–174.
[179] J.A. Peters, M.S. Nieuwenhuizen, A.P.G. Kieboom, D.J. Raber, J. Chem. Soc., Dalton Trans. (1988) 717–723.
[180] C.F.G.C. Geraldes, S.R. Zhang, A.D. Sherry, Inorg. Chim. Acta 357 (2004) 381–395.
[181] H. Gries, H. Miklautz, Physiol. Chem. Phys. Med NMR 16 (1984) 105–112.
[182] J.J. Stezowski, J.L. Hoard, Isr. J. Chem. 24 (1984) 323–334.
[183] K.I. Hardcastle, M. Botta, M. Fasano, G. Digilio, Eur. J. Inorg. Chem. (2000) 971–977.
[184] A. Mondry, P. Starynowicz, Polyhedron 19 (2000) 771–777.
[185] J. Wang, Y. Wang, X.-D. Zhang, Z.-H. Zhang, Y. Zhang, L. Ping Kang, H. Li, J. Coord. Chem. 58 (2005) 921–930.
[186] B. Liu, Y.F. Wang, J. Wang, J. Gao, R. Xu, Y.M. Kong, L.Q. Zhang, X.D. Zhang, J. Struct. Chem. 50 (2009) 880–886.
[187] R. Janicki, A. Mondry, Dalton Trans. 48 (2019) 3380–3391.
[188] J. Wang, G. Gao, Z. Zhang, X. Zhang, Y. Wang, J. Coord. Chem. 60 (2007) 2221–2241.
[189] J.A. Peters, Inorg. Chem. 27 (1988) 4686–4691.
[190] B.G. Jenkins, R.B. Lauffer, Inorg. Chem. 27 (1988) 4730–4738.
[191] B.G. Jenkins, R.B. Lauffer, J. Magn. Reson. 80 (1988) 328–336.
[192] P. Thakur, J.L. Conca, C.J. Dodge, A.J. Francis, G.R. Choppin, Radiochim. Acta 101 (2013) 221–232.
[193] R. Xu, D. Li, J. Wang, Y.X. Kong, B.X. Wang, Y.M. Kong, T.T. Fan, B. Liu, Russ. J. Coord. Chem. 36 (2010) 810–819.
[194] D. Pubanz, G. Gonzalez, D.H. Powell, A.E. Merbach, Inorg. Chem. 34 (1995) 4447–4453.
[195] P. Vojtíšek, P. Cígler, J. Kotek, J. Rudovský, P. Hermann, I. Lukeš, Inorg. Chem. 44 (2005) 5591–5599.
[196] M. Woods, K.M. Payne, E.J. Valente, B.E. Kucera, V.G. Young Jr., Chem. Eur. J. 25 (2019) 9997–10005.
[197] C.K. Schauer, O.P. Anderson, J. Chem. Soc. Dalton Trans. (1989) 185–191.
[198] Y. Inomata, D. Okamura, K. Morita, Y. Yukawa, F.S. Howell, J. Mol. Struct. 659 (2003) 23–34.
[199] J. Wang, P. Hu, B. Liu, R. Xu, Y. Wang, J. Gao, L. Zhang, X. Zhang, J. Coord. Chem. 62 (2009) 3168–3178.
[200] X. Chen, D. Li, J. Wang, B. Liu, Y. Kong, D. Wang, X. Zhang, J. Coord. Chem. 63 (2010) 3897–3906.
[201] J.Q. Gao, T. Wu, J. Wang, X.D. Jin, D. Li, B.X. Wang, K. Li, Y. Li, Russ. J. Coord. Chem. 37 (2011) 817.
[202] Y. Bai, J.Q. Gao, J. Wang, X.D. Jin, Y. Li, B. Wang, T. Wu, X.D. Zhang, Russ. J. Coord. Chem. 39 (2013) 49–57.
[203] F.Y. Tian, G.H. Liu, B. Li, Y.T. Song, J. Wang, Russ. J. Coord. Chem. 43 (2017) 304–313.
[204] F. Yerly, K.I. Hardcastle, L. Helm, S. Aime, M. Botta, A.E. Merbach, Chem. Eur. J. 8 (2002) 1031–1039.
[205] S. Aime, A. Barge, A. Borel, M. Botta, S. Chemerisov, A.E. Merbach, U. Müller, D. Pubanz, Inorg. Chem. 36 (1997) 5104–5112.
[206] R.C. Holz, S.L. Klakamp, C.A. Chang, W.D. Horrocks Jr., Inorg. Chem. 29 (1990) 2651–2658.
[207] C.A. Chang, H.G. Brittain, J. Telser, M.F. Tweedle, Inorg. Chem. 29 (1990) 4468–4473.
[208] F. Yerly, A. Borel, L. Helm, A.E. Merbach, Chem. Eur. J. 9 (2003) 5468–5480.
[209] N. Sakagami, Y. Yamada, T. Konno, K. Okamoto, Inorg. Chim. Acta 288 (1999) 7–16.
[210] R. Ragul, B.N. Sivasankar, J. Chem. Crystallogr. 41 (2011) 1273–1279.
[211] M.-L. Chen, Z. Xu, Z.-H. Zhou, Polyhedron 153 (2018) 213–217.
[212] X. Zhuang, Q. Long, J. Wang, Acta Crystallogr. E 66 (2010) m1436.
[213] D.-B. Xiong, H.-H. Chen, X.-X. Yang, J.-T. Zhao, Inorg. Chim. Acta 360 (2007) 1616–1620.
[214] K. Nakamura, T. Kurisaki, H. Wakita, T. Yamaguchi, Acta Crystallogr Sect. C: Cryst. Struct. Commun. 51 (1995) 1559–1563.
[215] L.K. Templeton, D.H. Templeton, A. Zalkin, H.W. Ruben, Acta Crystallogr. Sect. B: Struct. Sci. Cryst. Eng. Mater. 38 (1982) 2155–2159.
[216] D.W. Engel, F. Takusagawa, T.F. Koetzle, Acta Crystallogr. Sect. C: Cryst. Struct. Commun. 40 (1984) 1687–1693.
[217] L.R. Nassimbeni, M.R.W. Wright, J.C. van Niekerk, P.A. McCallum, Acta Crystallogr. Sect. B: Struct. Sci. Cryst. Eng. Mater. 35 (1979) 1341–1345.

[218] R. Janicki, P. Starynowicz, A. Mondry, Eur. J. Inorg. Chem. 2008 (2008) 3075–3082.
[219] J. Maigut, R. Meier, A. Zahl, R. van Eldik, Inorg. Chem. 47 (2008) 5702–5719.
[220] C.C. Bryden, C.N. Reilley, J.F. Desreux, Anal. Chem. 53 (1981) 1418–1425.
[221] D. Esteban-Gómez, A. de Blas, T. Rodríguez-Blas, L. Helm, C. Platas-Iglesias, ChemPhysChem 13 (2012) 3640–3650.
[222] C. Platas-Iglesias, D.M. Corsi, L. Vander Elst, R.N. Muller, D. Imbert, J.-C.G. Bünzli, E. Tóth, T. Maschmeyer, J.A. Peters, Dalton Trans. (2003) 727–737.
[223] R. Janicki, A. Mondry, Phys. Chem. Chem. Phys. 16 (2014) 26823–26831.
[224] N. Graeppi, D.H. Powell, G. Laurenczy, L. Zekany, A.E. Merbach, Inorg. Chim. Acta 235 (1995) 311–326.
[225] C.A. Chang, L.C. Francesconi, M.F. Malley, K. Kumar, J.Z. Gougoutas, M.F. Tweedle, D.W. Lee, L.J. Wilson, Inorg. Chem. 32 (1993) 3501–3508.
[226] F. Benetollo, G. Bombieri, L. Calabi, S. Aime, M. Botta, Inorg. Chem. 42 (2003) 148–157.
[227] M.R. Spirlet, J. Rebizant, J.F. Desreux, M.F. Loncin, Inorg. Chem. 23 (1984) 359–363.
[228] J.P. Dubost, J.M. Leger, M.H. Langlois, D. Meyer, M. Schaefer, C.R. Acad. Sci. Ser. II: Mec., Phys., Chim., Sci. Terre Univers 312 (1991) 329–354.
[229] S. Aime, A. Barge, M. Botta, M. Fasano, J. Danilo Ayala, G. Bombieri, Inorg. Chim. Acta 246 (1996) 423–429.
[230] D. Parker, K. Pulukkody, F.C. Smith, A. Batsanov, J.A.K. Howard, J. Chem. Soc. Dalton Trans. (1994) 689–693.
[231] S. Aime, A. Barge, F. Benetollo, G. Bombieri, M. Botta, F. Uggeri, Inorg. Chem. 36 (1997) 4287–4289.
[232] M. Pniok, V. Kubíček, J. Havlíčková, J. Kotek, A. Sabatie-Gogová, J. Plutnar, S. Huclier-Markai, P. Hermann, Chem. Eur. J. 20 (2014) 7944–7955.
[233] P. Hermann, J. Kotek, V. Kubíček, I. Lukeš, Dalton Trans. (2008) 3027–3047.
[234] I. Lukeš, J. Kotek, P. Vojtíšek, P. Hermann, Coord. Chem. Rev. 216–217 (2001) 287–312.
[235] E.T. Clarke, A.E. Martell, Inorg. Chim. Acta 190 (1991) 27–36.
[236] W.P. Cacheris, S.K. Nickle, A.D. Sherry, Inorg. Chem. 26 (1987) 958–960.
[237] J.F. Desreux, Inorg. Chem. 19 (1980) 1319–1324.
[238] S. Aime, M. Botta, G. Ermondi, Inorg. Chem. 31 (1992) 4291–4299.
[239] S. Hoeft, K. Roth, Chem. Ber. 126 (1993) 869–873.
[240] V. Jacques, J.F. Desreux, Inorg. Chem. 33 (1994) 4048–4053.
[241] C.C. Bryden, C.N. Reilley, Anal. Chem. 54 (1982) 610–615.
[242] M. Albin, W.D. Horrocks, F.J. Liotta, Chem. Phys. Lett. 85 (1982) 61–64.
[243] S. Aime, L. Barbero, M. Botta, G. Ermondi, J. Chem. Soc. Dalton Trans. (1992) 225–228.
[244] S. Aime, M. Botta, M. Fasano, M.P.M. Marques, C.F.G.C. Geraldes, D. Pubanz, A.E. Merbach, Inorg. Chem. 36 (1997) 2059–2068.
[245] M.P.M. Marques, C.F.G.C. Geraldes, A.D. Sherry, A.E. Merbach, H. Powell, D. Pubanz, S. Aime, M. Botta, J. Alloys Compd. 225 (1995) 303–307.
[246] S. Bénazeth, J. Purans, M.-C. Chalbot, M.K. Nguyen-van-Duong, L. Nicolas, F. Keller, A. Gaudemer, Inorg. Chem. 37 (1998) 3667–3674.
[247] J. Ren, S. Zhang, A.D. Sherry, C.F.G.C. Geraldes, Inorg. Chim. Acta 339 (2002) 273–282.
[248] C.F.G.C. Geraldes, S. Zhang, A.D. Sherry, Bioinorg. Chem. Appl. 1 (2003) 1–23.
[249] U. Cosentino, A. Villa, D. Pitea, G. Moro, V. Barone, A. Maiocchi, J. Am. Chem. Soc. 124 (2002) 4901–4909.
[250] M. Purgel, Z. Baranyai, A. de Blas, T. Rodriguez-Blas, I. Bányai, C. Platas-Iglesias, I. Tóth, Inorg. Chem. 49 (2010) 4370–4382.
[251] M.D. Vaira, P. Stoppioni, New. J. Chem. 26 (2002) 136–144.
[252] F. Avecilla, J.A. Peters, C.F.G.C. Geraldes, Eur. J. Inorg. Chem. (2003) 4179–4186.
[253] A.D. Sherry, C.F.G.C. Geraldes, W.P. Cacheris, Inorg. Chim. Acta 139 (1987) 137–139.
[254] C.F.G.C. Geraldes, A.D. Sherry, G.E. Kiefer, J. Magn. Reson. 97 (1992) 290–304.
[255] J. Ren, A.D. Sherry, Inorg. Chim. Acta 246 (1996) 331–341.
[256] C.F.G.C. Geraldes, R.D. Brown III, W.P. Cacheris, S.H. Koenig, A.D. Sherry, M. Spiller, Magn. Reson. Med. 9 (1989) 94–104.
[257] S. Aime, M. Botta, E. Terreno, P.L. Anelli, F. Uggeri, Magn. Reson. Med. 30 (1993) 583–591.
[258] S. Aime, M. Botta, D. Parker, J.A.G. Williams, J. Chem. Soc. Dalton Trans. (1996) 17–23.
[259] A.D. Sherry, J. Ren, J. Huskens, E. Brücher, E. Toth, C.F.C.G. Geraldes, M.M.C.A. Castro, W.P. Cacheris, Inorg. Chem. 35 (1996) 4604–4612.
[260] A.D. Sherry, C.R. Malloy, F.M.H. Jeffrey, W.P. Cacheris, C.F.G.C. Geraldes, J. Magn. Reson. 76 (1988) 528–533.
[261] D.C. Buster, M.M.C.A. Castro, C.F.G.C. Geraldes, C.R. Malloy, A.D. Sherry, T.C. Siemers, Magn. Reson. Med. 15 (1990) 25–32.
[262] E.S. Henriques, C.F.G.C. Geraldes, M.J. Ramos, Mol. Phys. 101 (2003) 2319–2333.
[263] A. Borel, L. Helm, A.E. Merbach, Chem. Eur. J. 7 (2001) 600–610.